Chemical and Physical Modification of Optical Transitions in Perovskite Quantum Dots

Ilka Vinçon

München, 2023

Chemical and Physical Modification of Optical Transitions in Perovskite Quantum Dots

Dissertation

to obtain the doctoral degree of natural sciences (Dr. rer. nat.)

at the Faculty of Physics

of the Ludwig-Maximilians-Universität München

submitted by

Ilka Vinçon

from Schramberg

Munich, 30th October, 2023

First referee:	Prof. Dr. Jochen Feldmann
Second referee:	Dr. Andreas Tittl
Date of oral examination:	20th December, 2023

Chemische und Physikalische Modifikation Optischer Übergänge in Perovskitquantenpunkten

Dissertation

zur Erlangung des Doktorgrades der Naturwissenschaften (Dr. rer. nat.)

an der Fakultät für Physik
der Ludwig-Maximilians-Universität München

vorgelegt von

Ilka Vinçon

aus Schramberg

München, 30.10.2023

Erstgutachter:	Prof. Dr. Jochen Feldmann
Zweitgutachter:	Dr. Andreas Tittl
Tag der mündlichen Prüfung:	20.12.2023

Publications, Conferences, and Awards

Scientific Publications of Results Presented in This Work

- I. Vinçon, F. J. Wendisch, D. De Gregorio, S. D. Pritzl, Q. A. Akkerman, H. Ren, L. de S. Menezes, S. A. Maier, J. Feldmann
  Strong Polarization Dependent Nonlinear Excitation of a Perovskite Nanocrystal Monolayer on a Chiral Dielectric Nanoantenna Array
  ACS Photonics 9 , 3506-3514 (2022)

- I. Vinçon, A. Barfüßer, J. Feldmann, Q. A. Akkerman
  Quantum Dot Metal Salt Interactions Unraveled by the Sphere of Action Model
  J. Am. Chem. Soc. 145, 14395-14403 (2023)

Additional Publications

- A. Dey, ..., I. Vincon, ..., L. Polavarapu
  State of the Art and Prospects for Halide Perovskite Nanocrystals
  ACS Nano 15, 10775-10981 (2021)

Conferences and Workshops

- *Econversion Conference 2021 (Poster)*
  Munich, Germany, September 2021

- *Econversion-PhD-Retreat 2021 (Poster)*
  Ettal, Germany, November 2021

- *OPTIMA 2022: Workshop on Optical Spectroscopy of New Materials 2022 (Talk)*
  Fall-Lenggries, Germany, July 2022

- *DPC 2022: 21st International Conference on Dynamical Processes in Excited States of Solids (Poster)*
  Wroclaw, Poland, September 2022

- *EOSAM 2022: European Optical Society Annual Meeting (Talk)*
  Porto, Portugal, September 2022

- *MATSUS23: Materials for Sustainable Development Conference (Talk)*
  Valencia, Spain, March 2023

- *Joint CeNS/SFB 1032 Workshop Venice (Poster)*
  Venice, Italy, September 2023

- *SolTech Conference 2023 (Talk)*
  Würzburg, Germany, October 2023

Awards

- **Best Poster Award**
  by Materials at the *DPC 2022*
  Wroclaw, Poland, September 2022
- **Front Cover in ACS Photonics**
  Volume 9, Issue 11, published in 2022
- **CeNS Travel Award**
  for the *MATSUS23: Materials for Sustainable Development Conference*
  Valencia, Spain, March 2023
- **Front Cover in JACS**
  Volume 145, Issue 26, published in 2023

Zusammenfassung

Quantenpunkte (QP) sind faszinierende Halbleitermaterialien und scheinen für neuartige Displays, Sensoren oder Quantencomputer wie gemacht zu sein. Als Material hat dabei besonders Bleihalidperowskit (BHP) im letzten Jahrzehnt mit herausragenden Eigenschaften für Furore gesorgt. BHP QP weisen etwa eine intrinsische Defekttoleranz, hohe Photolumineszenz-Quantenausbeute und spektrale Durchstimmbarkeit auf. Maßgeschneiderte Anwendungen erfordern jedoch – bedingt durch die geringe Größe von QP – das Wissen um und die Kontrolle von Wechselwirkungen mit der Umgebung. Eine wichtige Rolle spielen dabei chemische und physikalische Umgebungsmodifikationen, welche im Rahmen dieser Arbeit anhand der indikativen Photolumineszenz (PL) von BHP-QP analysiert wurden.
Zum einen wurde ein mikroskopisches Modell der Interaktion zwischen Metallsalzen und QP entwickelt. Solche Interaktionen werden etwa postsynthetisch zur Defektpassivierung oder Modulation der Zusammensetzung angewandt. Die Kombination von in-situ-spektroskopischen sowie zeitaufgelösten Methoden ermöglichte es, die Bildung kontrollierter, reversibler Oberflächendefekte bei Zugabe von $BiBr_3$ zu Kolloiden von sphärischen $CsPbBr_3$ QP nachzuweisen. Dies trägt zur Präzisierung der bislang unklaren Wirkung der Bismutheinlagerung in BHP-QP bei. Anhand des ungewöhnlichen Auslöschungsverhaltens wurde ein statistischer Wechselwirkungsprozess identifiziert und mit einem Aktionssphären-Modell beschrieben. Dabei offenbarte sich die Tragweite der gebildeten Defekte, von denen bereits ein einziger zur vollständigen PL-Löschung ausreicht. Durch Einführung eines Affinitätsfaktors ergab sich schließlich ein detailliertes mikroskopisches Bild des Adsorptionsprozesses. Relevante Prozessparameter, wie etwa Orte erhöhter Reaktivität oder der Einfluss einer Ligandenmonolage, konnten als Basis für künftige gezielte Oberflächenmodifikationen ermittelt werden.
Weiterhin wurde das Nahfeld von Metaoberflächen (MO) als mögliche physikalische Umgebungsmodifikation hinsichtlich BHP-basierter polarisierter Photodetektoren untersucht. Lösungsbasiert wurde eine Monolage kubischer $CsPbBr_3$ QP auf einer z-förmigen dielektrischen MO abgelagert. So wurde eine hybride, chirale BHP-MO gebildet, welche bislang nur mit BHP-Dünnschichten untersucht wurde. Durch PL-Mikroskopie wurde zirkularer Dichroismus unter nichtlinearer Anregung in den abgelagerten intrinsisch achiralen BHP-QP erzeugt. Das z-förmige MO-Design ermöglichte dabei starke polarisationsabhängige Resonanzen mit ausgeprägter Unterscheidung von links- und rechtszirkularem Licht im roten Spektralbereich. Dies eignete sich besonders für einen nichtlinearen Anregungsprozess im hybriden System. Die beobachtete Steigerung der PL-Intensität sowohl bei direkter als auch nichtlinearer Anregung konnte durch verstärkte Absorption in Folge von Streuung des Anregungslichts an der MO erklärt werden. Insbesondere wurde so eine Abhängigkeit von der Anregungswellenlänge sowie -polarisation mit einer chiralen Auflösung von bis zu 25 % erzielt.

Abstract

Quantum dots (QDs) are an attractive class of semiconductor material for a plethora of applications, ranging from novel display concepts via sensing to quantum computing. As a material, specifically lead halide perovskite (LHP) has shaken up the research community during the last decade. QDs made of LHP possess outstanding characteristics including intrinsic defect tolerance, near unity photoluminescence quantum yields and almost effortless spectral tunability. In view of their nanoscopic size, understanding and controlling interactions of LHP QDs with the surrounding is mandatory to enable in particular tailored applications. Especially chemical and physical modifications play an important role, which have thus been studied within this thesis by exploiting the strong photoluminescence (PL) of LHP QDs as a sensitive measure to elucidate important interaction mechanisms.

On the one hand, a microscopic model of the metal salt-QD interaction was developed – a post-synthetic treatment frequently employed for defect passivation or compositional change. In-situ spectroscopy was combined with time-resolved analysis to study the addition of $BiBr_3$ to colloidally dispersed spherical $CsPbBr_3$ QDs. A controlled and reversible formation of surface traps was found, allowing for further clarification of bismuth incorporation thus far under debate. The unusual quenching dynamics proved the statistical nature of the process and could be well described within a modified sphere of action model. This unraveled the trap's severity with adsorption of only one $BiBr_3$ sufficient to completely quench the PL of a $CsPbBr_3$ QD. By introducing a surface affinity factor, a detailed microscopic insight on the adsorption process was obtained: key parameters such as surface areas with exposed reactivity and the impact of a ligand monolayer were identified, providing a basis for future tailored surface alterations.

On the other hand, physical modifications provided by the near field of metasurfaces were explored as a potential pathway to enable LHP based polarized photodetectors. A monolayer of cubic $CsPbBr_3$ QDs was deposited on a z-shaped dielectric metasurface via a solution based process. This formed a hybrid chiral perovskite-metasurface, thus far limited to bulk perovskite films. Based on PL microscopy, the induction of nonlinear excited circular dichroism in intrinsically achiral LHP QDs was demonstrated in this hybrid system. The z-metasurface design enabled strong polarization dependent resonances in the red spectral range specifically discriminating left and right circularly polarized light. As such, it proved compatible with below band gap operation when combined with LHP QDs. Strongly enhanced PL intensities of LHP QDs for both, above and below band gap excitation were achieved. This could be assigned to an enhanced absorption in consequence of scattering of excitation light at the metasurface. Importantly, a dependence of the PL intensity on both, the excitation wavelength and polarization was achieved, yielding a chiral discrimination in PL of up to 25 %.

Table of Contents

1

Introduction

Most of what is considered a prerequisite for our modern life standard depends on semiconductor technologies: Every chip in smartphones or computers is based on semiconductors. Beyond that, they are employed for light harvesting in solar cells,[1,2] illumination technologies such as light emitting diodes (LEDs),[3,4] or serve as lasing material nowadays even utilized in medical diagnostics.[5,6] One of the most intriguing phenomena of semiconductors is their interaction with light. Charge carriers can be created on demand by absorption in the visible to near infrared spectral range. Novel materials that excel in this respect are thus of utmost importance to match growing demands in the aforementioned markets.

Lead halide perovskite (LHP) are such a material class. Equipped with a strong absorption ability and excellent charge transport properties, they are considered ideal for light harvesting applications.[7] Today, some of the best performing commercially viable photovoltaic devices utilize LHP films.[8] Early on, the enormous potential of this material class for light emitting applications has been noticed, too. Lasing with LHPs has been realized in 2014,[9,10] while the first LEDs had already been demonstrated in the 1990s.[11] Especially the LHP's apparent insensitivity to intrinsic defects combined with an ease for compositional and thus band gap modulation are favorable for light emission.[12]

Interest in LHP has gained increasing impetus with the availability of LHP colloidal nanocrystals.[13] Such size reduction to nanoscopic dimensions is an additional potent measure to vary semiconductor properties.[14] In quantum dots (QDs), where size confinement is present in all three dimensions, completely new physical behavior dominated by quantum effects occurs. Increased exciton binding energies together with narrow line widths and a size-dependent band gap are just a few of them.[15] Precise particle size control achieved during the last decades

thus led to tremendous advances in the field of nanotechnology, finally rewarded with the nobel prize in chemistry this year. Especially the facile low-cost colloidal synthesis strategy introduced by the group of Bawendi[16] paved the way for a broader application of QDs. Notably, they already found their way into diverse fields ranging from bio-imaging[17] to display technology and other light applications.[18] While one part of the success of QDs is their peculiar size-dependent physical properties, the strongly increased surface-to-volume ratio with diminished size is the second. Other than in bulk materials, interactions with the surrounding may severely impact the overall behavior and thus require a thorough understanding. This includes both, chemical and physical modifications.

For once, the large surface of a QD is prone to undergo chemical modifications, both wanted and unwanted. Numerous examples have demonstrated how ligand chemistry in colloidal systems can be exploited to introduce new functionalities,[19] e.g. utilized in biosensing[20,21] or solar cell applications.[22,23] Similarly, interactions with inorganic metal salts have also proven to impact luminescent properties of conventional QDs.[24,25] Such treatments with metal salts are particularly common for LHP nanocrystals. Post-synthetic addition of metal salts are not only applied to boost luminescence by surface defect passivation.[26] They may also induce strong modifications in the optical transitions including band gap shifts by anion exchange or energy transfer by incorporation of dopants due to partial cation exchange.[27] Yet, a precise mechanistic understanding and microscopic picture of this interaction, mandatory for an exclusive control of the process, is still due.

Secondly, QDs are often subject to an intimate contact with a substrate when incorporated in devices such as photodetectors, LEDs, or alike. Exposed to the surface's near field due to their small size, the substrate's impact is a viable method to achieve novel functionalities not inherent to LHP QDs itself. One of them is a distinct interaction with polarized light as needed e.g. for advanced optical components.[28] In this regard, a combination with metasurfaces is a promising approach. These artificial surfaces composed of subwavelength scatteres are characterized by a defined near field and controllable light-matter interactions, influencing optical transitions in emitters placed in their vicinity.[29] Thus far, bulk LHP films have proven to be successfully manipulated by suitable metasurfaces, enabling a discrimination for emitted light dependent on its polarization.[30–32] However, utilization of LHP QDs would allow to increase the flexibility in device fabrication compared to bulk layers.[13] Additionally, the efficient induction of polarization effects in the absorption of LHP by such a combination was yet to be shown.

Based on well defined model systems that exploit the characteristic, strong luminescence of LHP QDs as a sensor, I thus investigated the aforementioned chemical and physical modifications in the surrounding of QDs within this thesis. The basic concepts of QDs as light emitters, the material class of LHP, and physical and chemical surrounding manipulations are presented in Chapter 2. The purpose of Chapter 3 is to convey all necessary details utilized in

the subsequent analysis including both, the QD synthesis and all analytical tools. By a defined modification induced in the optical transitions of an as-synthesized LHP QD model system, a microscopic picture of a metal salt-QD interaction shall then be conceived in Chapter 4. Next, the challenge to equip LHP QDs with a polarization dependent absorption has been tackled by the demonstration of a hybrid perovskite-metasurface with two-photon induced circular dichroism in Chapter 5. The thesis concludes with Chapter 6, placing these results in context and providing prospects for future investigations.

2

Fundamentals

This chapter provides an overview of fundamental aspects governing the luminescence of lead halide perovskite (LHP) nanocrystals (NCs), explains possibilities for targeted modifications and discusses challenges provided by the influence of the NCs' surrounding. In Section 2.1, the material class of LHP NCs, its basic physical properties and their interaction with light is introduced. Impacts on a NC's chemical surrounding, possibilites for its modification and strategies to analyze resulting changes in luminescence are discussed in Section 2.2. Finally, Section 2.3 focuses on the physical aspects of light-matter interaction, introducing metasurfaces as a tool for local manipulations and the basic concepts of polarized light.

2.1 Lead Halide Perovskite Nanocrystals

2.1.1 From Bulk to Nano

As a crystalline material, a semiconductor is characterized by a periodic arrangement of its atoms in three dimensions. This periodicity imposes a fundamental constrain to physical properties, including an electron's probability density as pointed out by F. Bloch,[33] nowadays known as the Bloch theorem. An electron subject to a periodic potential $V(\boldsymbol{r})$, as provided by the atoms of the lattice, will inherit this periodicity within its wave function $\psi(\boldsymbol{r}) = e^{i\boldsymbol{k}\boldsymbol{r}}u(\boldsymbol{r})$. It is expressed as a plane wave modulated by a function $u(\boldsymbol{r})$ that carries the lattice periodicity, while the wave vector $\boldsymbol{k}$ is unique when chosen within the first Brillouin zone.[34] In conjunction with other simplifications for the many particle problem of an electron residing inside a lattice,[35–37] this forms the basis for solving Schrödinger's equation and defining the eigenvalues $E(\boldsymbol{k})$ of such an electron with the help of perturbation theory.
Bands, quasi-continuous regions of possible energy values (equivalent to twice the number of orbitals involved in their formation) separated by forbidden energy gaps, are formed. This is a result of the perturbation imposed on an atomic potential when orbitals overlap given the atoms' proximity in the periodic lattice (tight binding approximation).[34,38] These allowed energy states are depicted in a simplified sketch in Figure 2.1a. Intrinsic semiconductors possess a filled valence band. In such systems, mobile charge carriers only exist once an electron is given enough energy to be lifted to the conduction band, creating a hole in the valence band at the same time.[38] Given the band gap energy $E_g < 3\,\mathrm{eV}$ of semiconductors, a

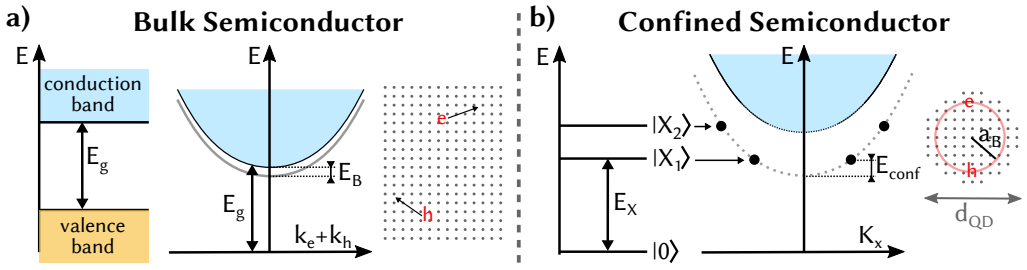

Figure 2.1: Size-Dependent Properties of Semiconductors. Characteristics of charge carriers residing in the lattice for a 3D-bulk and a 0D-nanocrystalline confined intrinsic semiconductor material, respectively. **a** Left: Electrons (holes) reside in quasi-continuous conduction (valence) bands separated by a band gap E_g. Middle: Two particle picture of the band structure with a continuum level (blue). Excitons, characterized by their center-of-mass motion dispersion (grey), readily dissociate given their weak binding energy E_B. Right: Electrons (holes) move separately through the lattice, carrying a quasi-momentum $\boldsymbol{k}_e$ ($\boldsymbol{k}_h$). **b** Left: Weakly confined systems ($a_B > {}^{d_{QD}}/_2$) act as a quantum box of diameter d_{QD} for an exciton with Bohr radius a_B with discrete energetic states of energy E_X. Middle: Two particle picture with the center-of-mass motion, carrying a quasi-momentum $\boldsymbol{K}_X$, discretisized with the confinement energy E_{conf}. Right: Quantum confinement increases the free carriers' energy, stabilizing the formation of excitons in QDs .

limited amount of charge carriers is present dependent on the temperature,[34,39] and more carriers may be generated electrically or optically (see Subsection 2.1.3).
Electrons (holes) are equipped with a quasi-momentum $\boldsymbol{k}_\mathrm{e}$ ($\boldsymbol{k}_\mathrm{h}$) that is limited to a set of non-equivalent values defined by the first Brillouin zone. In a direct gap semiconductor, the minimum and maximum of conduction and valence band, respectively, coincide regarding this quasi-momentum. Then, the complex band structure with its dispersion relation $E(\boldsymbol{k})$ can be simplified around the band gap in a two-particle picture[40] as depicted in Figure 2.1a, using the sum of the momenta and energies for a pair of electron and hole. A parabolic dispersion

$$E_\mathrm{e}(\boldsymbol{k}_\mathrm{e}) = \frac{\hbar^2 \boldsymbol{k}_\mathrm{e}^2}{2m_\mathrm{e}^*} \tag{2.1}$$

characterizes the quasi-free motion as exemplary shown for the electron. $\hbar$ denotes the reduced Planck constant, while the perturbation imposed by the periodic potential is considered in form of an effective mass m_e^* instead of the electron's inherent mass m_e.[41]
In addition to the continuum obtained with this effective mass approximation, a parabolic dispersion is depicted in Figure 2.1a. This is a result of the non-negligible Coulomb attraction between charged particles. It provides a perturbation for the quasi-free electrons and holes thus far considered to move independently. The as-formed quasiparticle composed of an electron and hole bound to each other by Coulomb interaction is termed an exciton. Weak perturbations result in "hydrogen-like" Wannier-Mott excitons,[39,42] whose characteristic energetic levels are separated from the continuum by the exciton's binding energy

$$E_\mathrm{B} = -\frac{e^4 \mu}{2(4\pi\epsilon_0\epsilon)^2\hbar^2}\frac{1}{n_\mathrm{r}^2} = -\frac{1}{2}\frac{e^2}{4\pi\epsilon_0\epsilon \cdot a_B}\frac{1}{n_\mathrm{r}^2} = -\frac{Ry^*}{n_\mathrm{r}^2}. \tag{2.2}$$

This relative motion of electron and hole around each other is defined by a Bohr radius a_B, the quantum number n_r and the effective Rydberg energy Ry^*. The latter is associated with the relative coordinate $\boldsymbol{r}$, the system's reduced mass μ and the material's dielectric constant ϵ, while other constants have the usual meaning. The exciton behaves as one particle, whose center of mass motion with a coordinate $\boldsymbol{R}$ gives rise to a dispersion similar to Equation 2.1 with the exciton momentum $\boldsymbol{K}$ and overall mass $M = m_\mathrm{e}^* + m_\mathrm{e}^*$.[39] In 3D inorganic semiconductors, the exciton Bohr radius a_B spans several unit cells. This is caused by the material's dielectric constant ϵ significantly exceeding the vacuum value, i.e. the charges are effectively screened from each other.[39] As a result, the binding energy E_B is usually small within the order of tens of meV and the exciton is prone to thermal dissociation. Overall, the energetic landscape of bulk semiconductors can thus be well described by bands with a quasi-continuum of states for electrons and holes that move mostly separately through the lattice (Figure 2.1a). However, this picture changes significantly when the crystal's dimension is reduced.

When at least one dimension is reduced to the nanoscale, so called NCs are formed. They may be present supported on substrates based on physical procedures such as epitaxial growth, or as colloids in solution.[14] The latter are stabilized electrostatically or sterically by adsorption of charged or long chain organic molecular species, respectively.[19] NCs are characterized by their number of dimensions that remain unrestricted in size: quantum wells, or in a colloidal form nanoplatelets, are examples of 2D systems, while quantum wires/nanorods represent a 1D system. Finally, the 0D-representatives are quantum dots, whose size is restricted in all three dimensions.

The term "quantum" is introduced once the restricted dimension gets small enough for phenomena related to the quantum character of the carriers to occur. This is the case when the size gets close to the exciton Bohr diameter or the de-Broglie wavelength of electrons or holes.[39] Then, they cannot move freely anymore but experience quantum confinement, i.e. the NC presents a quantum box for the particle. When the crystal's dimension a is still larger than the exciton's Bohr diameter, the energy landscape is well described in the weak confinement limit. This assumes confinement to act as a perturbation for the Wannier-Mott type excitons,[39] yielding excitonic energies E_X of

$$E_X = E_\mathrm{g} - \frac{Ry^*}{n_\mathrm{r}^2} + \frac{\hbar^2\pi^2 n_\mathrm{R}^2}{2Ma^2} \tag{2.3}$$

With respect to the band gap energy E_g in a 3D system, stabilization is achieved dependent on the exciton's relative motion as described by its binding energy E_B (Equation 2.2). However, the center of mass motion is not simply described by Equation 2.1 anymore, but confined due to the quantum dot's size. Thus, it is discretized in form of a confinement energy E_conf.[39] In consequence, the parabolic dispersions, shown in Figure 2.1a for the lowest relative motion level ($n_\mathrm{r} = 1$), "break up" into quantized excitonic states (Figure 2.1b). They are distinguished by their center of mass motion quantum number n_R as $|X_1\rangle$, $|X_2\rangle$, which depend on the quantum dot's dimension a as stated in Equation 2.3.

Apart from a discretization of the exciton's motion, confinement of any free electron and hole causes their energy to be increased with respect to the band gap, too.[39] This explains the upward shift of the "continuum" compared to a 3D bulk system (Figure 2.1b). As a result, the effective binding energy of the exciton is increased,[39] although the energy gained through Coulomb interaction remains unperturbed. Notably, the "quantum effect" gets even more dominant when the system's size is reduced below the exciton Bohr radius. Due to a reduced shielding of the charge carriers, the Coulomb interaction between electrons and holes is additionally enhanced. In the limit of such strong confinement, the "continuum" break apart intro discrete states.[39] Overall, confinement effects cause a stabilization of excitons. Thus, they are dominant in quantum sized structures (Figure 2.1b), unlike in bulk materials where they can often be neglected.

2.1.2 The Unique Class of Perovskite Semiconductors

Semiconductor research has long been focused on so called conventional semiconductors, which include the commercially most utilized semiconductor silicon, but also GaAs or CdTe as examples of III-V and II-VI semiconductors.[7,40] Only within the last 20 years, lead halide perovskites (LHPs) received significant attention as a prospective novel semiconductor material with outstanding optoelectronic properties.[12,13] Their name perovskite refers to a specific type of crystal structure adopted by compounds with a composition ABX_3, as depicted in Figure 2.2. In these compounds, A and B are cations while X is an anion.[46] They possess a cubic or orthorhombic crystal structure composed of corner sharing $[BX_6]$-octahedra, incorporating A-cations in the formed cuboctahedral voids. Deciphered by Barth in 1926,[47] the structure's stability can be described in terms of a tolerance factor t. This has been introduced by Goldschmidt based on the spatial need of A,B, and X with their specific radii R

$$t = \frac{R_B + R_X}{\sqrt{2}(R_A + R_X)}, \tag{2.4}$$

with $0.76 < t < 1.13$.[27,46] This structure is by far not unknown – perovksite-type oxides can be formed by approximately 90% of metals in the periodic table. As such, they have already been investigated in the 70s for their catalytic properties.[48] The "grandfather" of these compounds is the naturally occurring $CaTiO_3$, which has been first described by Gustav Rose for a sample found in the ural mountains and named in honor of the mineralogist Lev Perovski.[49] Lead halide perovskite refers to a subcategory of perovskite compounds that are based on lead cations Pb^{2+} and halide anions X^-. Their A-site cation may be cesium in fully inorganic structures or an organic cation in hybrid organic-inorganic structures.[27]

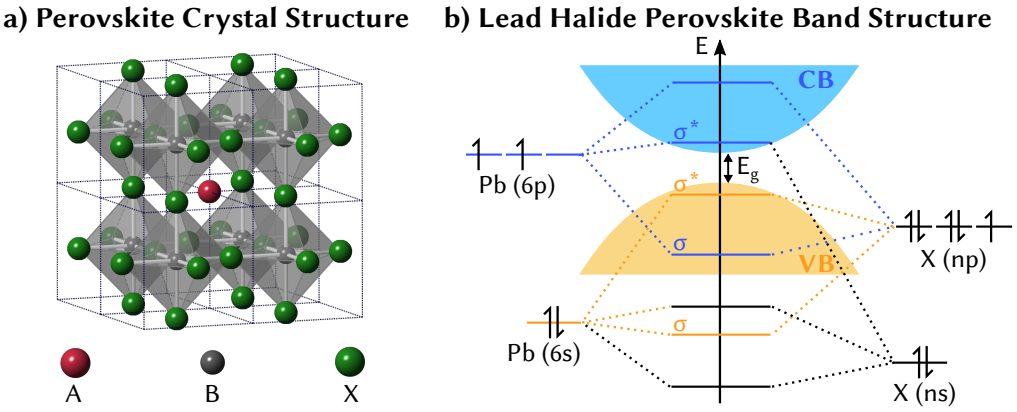

Figure 2.2: Properties of Perovksite Semiconductors. a Crystal structure of a general perovskite ABX_3, where for LHP A = Cs, B = Pb and X = I, Br, Cl (adapted from [43]). **b** Formation of the LHP band structure by hybridization of halide and lead orbitals (adapted from [44],[45]). Contributions to the conduction/valence band (CB/VB) are shown in blue and orange, respectively. E_g refers to the band gap energy while σ (σ^*) denote the bonding (antibonding) contributions.

Although LHPs have been known for more than 100 years, their rise to a globally noted semiconductor only set off when their capacity for solar cells had been demonstrated and rapidly expanded to applications for light generation.[13,27] Its impressive optoelectronic properties are closely linked to their band structure, as depicted in Figure 2.2.
LHPs are direct gap semiconductors with their band edge states formed by a hybridization of lead and halide orbitals within the $[PbX_6]^{4-}$-octahedra, while the A site cations are not directly involved.[44,50] Both, the valence band minimum and the conduction band maximum can be attributed to antibonding ($\sigma^\star$) states. The conduction band arises form an interaction of halide s and p orbitals with lead $6p$ orbitals and carries the dominant p character of the latter. The associated bonding orbitals (σ) are buried in the valence band. Their dominant halide character implies a charge transfer form lead to halide, forming the σ-bond between them.[45] The valence band maximum is formed from the antibonding $\sigma^\star$-interaction of lead $6s$ and halide p orbitals.[44,50]
Overall, the valence band is considered s-type while the conduction band is p-type, an inverse arrangement compared to conventional semiconductors.[13] This significantly simplifies the spin structure of the band-edge states, making them promising candidates for spin applications, as discussed in detail e.g. by S. Strohmair and others.[51–53] Likewise, the LHPs extraordinary long carrier diffusion lengths,[54,55] which highlights their potential for light harvesting applications, has been linked to the band structure: With the given orbital contribution of the bandedge states, a reduced wave function overlap of electrons and holes has been proposed.[7] Finally, the halide's contribution to the valence band[44] in conjunction with the lattices ionicity[27] enables an easy adjustment of the bandgap energy within the visible region. When altering the halide composition from iodide up to chloride, the conduction band's energy is slightly increased as a result of the lattice contraction in this process. The valence band, however, is lowered towards chloride due to its increased electronegativity that outcompetes the energy increase due to lattice contraction.[44,56] Overall, the bandgap thus increases from iodide up to chloride. Together with their defect tolerance (see Subsection 2.2.1), LHPs are therefore well suited for applications requiring an interaction with light.

2.1.3 Perovksite NCs: Light Emitters for the Future

Especially once reduced to nanoscale dimensions, LHPs excel as a material with respect to interaction with light. Within the broader group of such systems investigated for light applications, the focus shall be placed on colloidal LHP NCs. To-date, they have been realized e.g. as nanoplatelets,[57–59] nanowires,[60] and also QDs.[61,62] Several characteristics arise from downsizing to the nanoscale, which contribute to the success of LHP NCs. Prior to discuss these characteristics and advantages compared to bulk materials, I summarize the basic concepts of a NC interaction with light.

Excitation and Relaxation Processes in QDs

LHPs are governed by comparably small exciton Bohr diameters between 5 nm in chloride based up to 12 nm in iodide based systems.[61] The size of LHP NC treated within this thesis (approx. 5-12 nm) is therefore not significantly smaller than the Bohr diameter, though still in the confinement range. Such NCs can be well described as QDs in the weak confinement limit.[63] Thus, the overview of important interaction processes with light is limited to a purely excitonic system of weakly confined QDs. Such processes, divided into excitation and recombination, are shown in Figure 2.3.
When photons hit a QD, they may be annihilated on the expense of increasing an electron's energy. This can initiate an excitation, i.e. a transition between the electronic ground state $|g\rangle$ and excited state $|f\rangle$:[64,65]

$$|g\rangle + m \cdot \text{Photon} \rightarrow |f\rangle \tag{2.5}$$

Such a process is called absorption of m photons. In order to occur, energy and momentum conservation need to be fulfilled.[39] Usually, the very small photon's momentum is neglected and a "vertical" transition in the band diagram is assumed. With the photon's energy E_ν related to its frequency ν by $E_\nu = h\nu$, energy conservation implies that $m \cdot h\nu = E_{|f\rangle} - E_{|g\rangle}$. If one photon ($m = 1$) is sufficient to create the excited state, it is called a linear absorption or above band gap excitation. $m > 1$ refers to a below band gap excitation/multi-photon absorption event of order m, exemplary depicted in Figure 2.3 for a two-photon absorption. In such a nonlinear process, several (m) photons interact simultaneously with the NC to create one excited state.[66] Overall, the transition $|g\rangle \rightarrow |f\rangle$ happens with a certain probability, which can be described in terms of a rate equation for the formation of the excited state:[64,65]

$$\left(\frac{\mathrm{d}n_f}{\mathrm{d}t}\right)_{\mathrm{ex}} = \Gamma_{\mathrm{fg}} n_g = k \cdot n_\nu^m \cdot n_g. \tag{2.6}$$

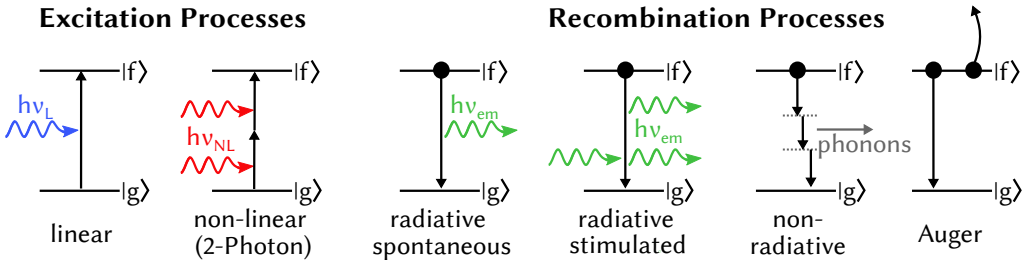

Figure 2.3: Optical Processes in Quantum Dots. A QD with a ground state $|g\rangle$ and excited state $|f\rangle$ can be subject to different excitation and subsequent recombination processes. In a linear or nonlinear optical excitation, one or multiple photons are absorbed, respectively. Recombination may occur radiatively, i.e. emitting a photon in a spontaneous or stimulated emission process, or non-radiatively, dissipating the energy in form of phonons mediated by trap states or transferring it to another exciton, termed Auger-recombination.

Here, n_i with $i \in \{g, f\}$ are the densities of the ground state and excited state, respectively. The transition rate Γ_{fg} can be rigorously derived from a quantum mechanical treatment in the realm of perturbation theory (see Fermi's Golden rule in Section 2.3).[64] At this point however, a more simple relation to the excitation light's intensity I_{ex} is established. The transition rate is proportional to the density of photons $n_\nu = \mathrm{d}N_\nu/\mathrm{d}V$ with frequency ν that are annihilated in the process, given a proportionality constant k.[65] As evident from Equation 2.6, the transition rate scales with the process order, since m photons are required to interact simultaneously with the QD. The photon density is directly linked to the light's intensity I_{ex}, defined as the energy E transferred per unit area A and time t:[67]

$$I_{\mathrm{ex}} = \frac{\mathrm{d}^2 E}{\mathrm{d}t\,\mathrm{d}A} = E_\nu \frac{\mathrm{d}N_\nu}{\mathrm{d}V}\frac{\mathrm{d}x}{\mathrm{d}t} = E_\nu \cdot c \cdot n_\nu, \tag{2.7}$$

given the photon's energy E_ν and considering their velocity $c = \frac{\mathrm{d}x}{\mathrm{d}t}$. Thus, a direct relation between the excitation rate and the excitation light's intensity I_{ex} can be established:

$$\left(\frac{\mathrm{d}n_f}{\mathrm{d}t}\right)_{\mathrm{ex}} \underset{\text{Equation 2.6, 2.7}}{=} \frac{k}{(c \cdot E_\nu)^m} I_{\mathrm{ex}}^m \cdot n_g. \tag{2.8}$$

Evidently, the excitation rate is proportional to the impinging light's intensity scaled by the order m of the process. This explains why nonlinear processes only occur at high excitation intensities, while linear processes dominate at low excitation intensities.[65] The efficiency of a system to undergo an excitation process of order m is usually compared in terms of its cross-section $\sigma_{(m)} = m \cdot k/c^m$, defined by the constants in Equation 2.8.[68] Alternatively, the loss in light intensity due to the excitation process can be defined by relating the rate of excited state formation with the change in photon density:

$$\left(\frac{\mathrm{d}I_{\mathrm{ex}}}{\mathrm{d}x}\right) \underset{\text{Equation 2.7}}{=} \left(\frac{\mathrm{d}n_\nu}{\mathrm{d}t}\right) E_\nu \underset{\text{Equation 2.6}}{=} -m\left(\frac{\mathrm{d}n_f}{\mathrm{d}t}\right)_{\mathrm{ex}} E_\nu \underset{\text{Equation 2.8}}{=} -\frac{m \cdot k}{c^m \cdot E_\nu^{m-1}} \cdot n_g I_{\mathrm{ex}}^m =: -\alpha_{(m)} I_{\mathrm{ex}}^m \tag{2.9}$$

Herein, an overall absorption coefficient $\alpha_{(m)}$ has been defined. This relation will be useful in the experimental determination of a sample's absorption behavior (see Section 3.4). For now, it is merely pointed out that LHP NCs have been found to exhibit large absorption coefficients,[69,70] which has initiated their application as sensitizer[71] and light harvesting material.[72] In addition, LHP NCs may also be promising for non-linear optics. With large two-photon absorption cross sections exceeding those of conventional quantum dots being reported,[73,74] they are prone for applications based on a non-linear excitation processes. So far, this has been utilized to demonstrate two-photon pumped lasing[75] and suggested to improve light harvesting by combining multi-photon absorption with multi-exciton generation.[76]

Subsequent to an excitation, the system returns to the initial ground state by disposing its excess energy through one of the recombination processes depicted in Figure 2.3. Generally, recombination occurs from the lowest excited state $|f\rangle$, to which a system relaxes quite fast after an excitation process. Again, energy and momentum conservation are fulfilled. The system may recombine radiatively, i.e. re-radiate a photon, which is called photoluminescence (PL). This happens spontaneously after an average lifetime τ of the excited state. However, the recombination may also be stimulated by a photon of equivalent energy, which is essentially a reversal of the excitation process and in a simple two-level system governed by the same rate.[67] Alternatively, the system can dissipate its energy non-radiatively to phonons or to another exciton in an excited state. The former often involves defect states (see Subsection 2.2.1), while the latter is termed Auger-recombination.[77]
Similar to the excitation process, the recombination may be described in terms of a rate equation:

$$\left(\frac{\mathrm{d}n_f}{\mathrm{d}t}\right)_{\mathrm{rel}} = -k_{\mathrm{r}}n_f - k_{\mathrm{nr}}n_f - k_{\mathrm{Auger}}n_f^2 \tag{2.10}$$

The first term describes the spontaneous radiative recombination and the second term those non-radiative recombinations that only involve one excited state. Both are proportional to the density of the excited states.[67,78] The last term in Equation 2.10 considers Auger-recombination, which depends on the squared excited state density given the bimolecular nature of the process.[79–81] As Auger recombination is only relevant at higher excited state densities,[77] it is often neglected. Then, the relaxation rate is directly proportional to the rate of emitted photons. Therefore, when excitation and recombination rates are balanced in a steady-state experiment, i.e. $\left(\frac{\mathrm{d}n_f}{\mathrm{d}t}\right)_{\mathrm{ex}} = -\left(\frac{\mathrm{d}n_f}{\mathrm{d}t}\right)_{\mathrm{rel}}$, the simple relation $I_{\mathrm{em}} \propto I_{\mathrm{ex}}^m$ can be established between emission and excitation intensity. This relation proves to be very insightful for the identification of multi-photon absorption processes.
Finally, a purely excitonic system without contribution of Auger recombination is simply goverened by a monomolecular recombination dynamics as a function of time t

$$I_{\mathrm{em}}(t) = I_{\mathrm{em},0}\mathrm{e}^{-t(k_{\mathrm{r}}+k_{\mathrm{nr}})} = I_{\mathrm{em},0}\mathrm{e}^{-t/\tau} \tag{2.11}$$

with an overall lifetime τ of the excited state and an initial emission intensity of $I_{\mathrm{em},0}$. Both, radiative and non-radiative decay processes contribute to this relaxation process. However, non-radiative recombination is usually an unwanted side-effect in luminescent samples. Thus, the photoluminescence quantum yield (PLQY), i.e. the ratio between radiative and total recombination rate PLQY $= k_{\mathrm{r}} \cdot \tau$, has been established as a measure for a system's efficiency to radiatively recombine.[78]

Especially with respect to this PLQY, lead halide perovskite (LHP) QDs and in general its NCs are outstanding light emitters reaching values surpassing 90 %.[61,82] This benefit is combined with an extremely narrow linewidth of approximately 110 meV, which puts LHP NCs right from the start on par with commercialized sophisticated conventional QD emitter systems.[83] Synthetic protocols that enable to easily tune the emission wavelength throughout the complete visible spectral range[61,84] complement these excellent luminescent properties. The described characteristics are partially linked to the minor impact of non-radiative decay channels dictated by the LHP intrinsic band structure, as discussed in Subsection 2.2.1. On the other hand, they are a consequence of the transition to nanoscale dimensions.
Firstly, confinement as introduced in Subsection 2.1.1 provides an additional degree of freedom to tune the band gap. The bulk band gap merely provides a lower limit, while increasingly larger band gaps are feasible when shrinking the system's size. This allows to enter regimes otherwise not accessible, an advantage for many applications e.g. light harvesting, sensing or display technologies.[14] On top of that, the reduced screening and thus stronger carrier-carrier interaction once advancing the dimensions of the system's exciton Bohr diameter increases an exciton's binding energy.[57,58,85] Such a strong increase in exciton binding energy to several 100 meV[58] has been observed in two dimensional systems and linked with a faster decay rate.[57] As such, the formation of excitons is vital for high PLQYs by favoring radiative recombination, a crucial prerequisite for light emitting applications such as LEDs.[13,57] A discretization in form of the excitonic levels is furthermore favorable for the NC's interaction with light by enabling the narrow linewidths of its emission signals.[14] Thus, the high color purity of LHP NCs meeting international standards for a potential application in displays[12,13] is also linked to their nanoscale dimension.
Apart from these favorable properties, there are, however, still a few obstacles for LHP NCs to be solved for them to become the next generation light emitters. Unfortunately, the ionic structure that enables easy tunability is also a major drawback causing an instability to temperature, light, oxygen and also humidity.[13,83] In this context, it is essential to understand the defect chemistry and impacts of the surrounding on such a nanoscale object.

2.2 Chemical Modification of a NC Surrounding

Reduction to the nanoscale goes hand-in-hand with an increase in the surface to volume ratio. The severity is evident when estimating the number of unit cells that are in contact with the surface in a LHP QD: while the fraction is less than 1 % in a QD with 200 nm diameter, more than 30 % are affected in a 6 nm QD. As such, next to the physical properties described in the previous section, the surface is a unique feature that sets nanometer-sized materials apart from their bulk counterparts. Modifications in the chemical surrounding at this surface, e.g. the type of termination or proximity to other species, thus significantly impact a NC's optical

or charge transfer properties.[19,86] This is good and bad at the same time.
On the one hand, the surface may give rise to unwanted side effects. Especially for luminescent applications, it is important to identify and eliminate side processes that may cause alternative decay channels next to the desirable radiative recombination. Dependent on the surface termination, undercoordinated atoms are present[86] and such defects may serve as centers for non-radiative decays.[87] Thus, the impact of defects on the optical performance of perovskite NCs is discussed in Subsection 2.2.1.
On the other hand, the surface chemistry can be exploited to pointedly manipulate the NCs' functionality. This is specifically easy in colloidal NC systems. Surface interactions with ligands already stir the synthesis with respect to dimension[58] or shape (see Chapter 3), detrimental to achieve the huge variety of colloidal systems.[14] Also post-synthetically, the impact of ligands on the electronic structure through formation of joint surface states[86] can be directly utilized. This has been demonstrated in energy transfer[88] or charge separation[23] for light harvesting or sensing and even in combination with biological systems.[21] Targeted post-synthetic modifications allow an additional manipulation. Such treatments are extensively used for LHP NCs as discussed in detail in Subsection 2.2.2. Finally, development and improvement of a specific surrounding requires to closely monitor any employed changes. The NC's bright luminescence is a sensitive indicator for such modulations. Thus, fluorescence quenching methods established to gather information about reactions of fluorophores are introduced in Subsection 2.2.3.

2.2.1 Lead Halide Perovskites and Defect Tolerance

Other than in conventional systems,[89] LHP NCs are able to achieve high PLQY values without requiring an extensive passivation of surface-based non-radiative decay channels.[27,83] This is commonly explained by their so called "defect tolerance". The impact of defects on luminescent properties and the special case of defects in LHP NCs shall thus be elucidated in this section.

Defects Formation in Semiconductors

Defects are a disruption of the perfect periodic three dimensional arrangement of the crystal structure.[38,40] One of the most evident examples of such an imperfection is the surface of a NC itself.[90] However, defects also occur in the interior of every crystal, formed i.e. during synthesis due to faults in the atomic arrangement with all possible dimensional manifestations. Here, merely the zero-dimensional so called point defects, which involve a single lattice site only, are discussed in detail given their detrimental character for a semiconductor's performance.[90] Generally, an atom of the lattice can be replaced, displaced or missing,[38,40] as depicted in Figure 2.4a.

When atoms not native to the material occupy a lattice site, an impurity is formed. Often, such impurities are introduced on intent as dopants, possessing more or less valence electrons than the atom they replace. A well-known example is the incorporation of phosphor atoms, possessing five valence electrons, in four-valent silicon. The result is a drastic change in the electronic and also optical properties by charge injection of the excess carrier in the conduction band, a process vital for the success of semiconductor applications.[91] Apart from such deliberate extrinsic defects, point defects already form intrinsically, i.e. involving only lattice native atoms. This is a natural consequence of the increase in the system's entropy by the induced disorder.[34] Replacements by lattice intrinsic atoms are called antisite. Additionally, Frenkel defects form. This involves an ion relocating to an empty void forming an interstitial, while leaving an empty lattice site, a vacancy, behind. Vacancies can also be caused by removal of ions migrating to the surface. Charge neutrality dictates that this occurs as pairs of positive and negative vacancies, so called Schottky defects.[34,38]

A defect's impact on the electronic structure of a semiconductor is linked to the type of perturbation that it imposes[90] within the periodic potential. Generally, charge carriers are described by the Bloch function as a result of the periodicity demanded by the lattice. Shallow defects inflict mild perturbations to this order, e.g. in form of a dopant atom as a positively (negatively) charged core with an excess electron (hole). They can be treated within the realm of the effective mass approximation and are thus "hydrogen-like".[34,90] The carrier gets loosely bound to the defect by Coulomb interaction, weakened as a result of the material's screening effect. The impact of the periodic crystal potential is considered in form of an effective mass for the carrier. As such, they are similar to excitons discussed in Subsection 2.1.1 with the carrier delocalized across various unit cells (Figure 2.4b), however, with the important

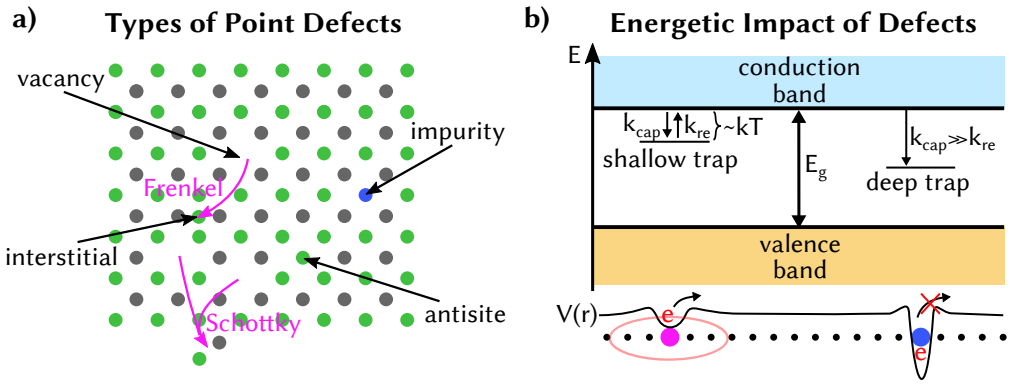

Figure 2.4: Defects and their Impact on the Energetic Landscape. a Schematic of point defects formed in a crystal lattice due to removal (vacancy), replacement (impurity/antisite) or relocation (interstitial) of its composing atoms. **b** Modification imposed by defects on the charge carrier properties of a semiconductor. Top: Action of a defect as a trap based on its energetic position relative to a band, with rate constants for the capture (k_{cap}) and release (k_{re}) process. Bottom: Deformation that positive defects impose on the potential, demonstrating the excitonic character of a shallow trap compared to the localizing impact of a deep trap.

difference that one part of this "exciton" is the defect that possesses an infinite mass.[90] In the band structure, such defects form energetic levels close to the respective band edge.[34] Deep defects, on the other hand, refer to states well separated from conduction and valence band. They are formed by strong perturbations for which the effective mass model breaks down.[90] As a consequence, a carrier that gets close to such a defect gets localized and a detachment does not occur at a significant rate. Thus, defects are also referred to as traps.

The Impact of Defects on Radiative Recombination

The interaction of carriers with defects has a profound impact on the optical properties of a material by providing additional recombination pathways. Such trap mediated recombination for defects has been described by Shockley, Read[92] and Hall[93] for doped semiconductors. This is depicted in Figure 2.4b exemplary for a defect level close to the conduction band. An electron is captured (k_{cap}) or released (k_{re}) from this defect at certain rate with their ratio dependent on the electron's energy E relative to the defect level's energy E_{t}:[92]

$$\frac{k_{\mathrm{re}}}{k_{\mathrm{cap}}} = \mathrm{e}^{-(E-E_{\mathrm{t}})/k_{\mathrm{B}}T} \tag{2.12}$$

When the energy barrier between defect level and conduction band is small, i.e. within the range of the thermal energy ($k_{\mathrm{B}}T \approx 26\,\mathrm{meV}$ at room temperature), the electron is readily released again. This is the case of shallow defects, characterized by energy differences within tens of meV.[91] However, for deep defects located approximately mid-gap, the electron gets localized at the defect and detachment does not occur at a significant rate. Such a trapped electron can then undergo recombination with a hole, which is prone to happen non-radiatively.[94] The overall trap-mediated recombination for such deep traps is described by:[77,94]

$$\left(\frac{\mathrm{d}n}{\mathrm{d}t}\right)_{\mathrm{trap}} = -k_{\mathrm{trap}} \cdot m \cdot n \tag{2.13}$$

It is proportional to the carrier's density n and the number of trap states m in the system, assuming that only a negligible amount of traps are filled, e.g. due to a fast subsequent non-radiative relaxation of trapped carriers.[77] The trapping rate k_{trap} accounts for the effectiveness of the trap-mediated recombination process. Thus, introducing traps to a system modifies its luminescence intensity I_m by opening an additional non-radiative decay channel, whose decay rate $k_{\mathrm{nr}} = k_{\mathrm{trap}}m$ heavily depends on the precise number of traps present. Thus I_m is obtained by integration and rearrangement of Equation 2.11 as

$$I_m = \frac{I_0}{1 + k_{\mathrm{trap}}\tau_0 m}, \tag{2.14}$$

with I_0 and τ_0 as the pristine system's intensity and recombination rate.

Defects in Lead Halide Perovksite NCs

The question, whether shallow or deep traps are formed by intrinsic defects is closely related to the material's band structure. The formation of a vacancy implies the removal of an atom, thus leaving the remaining atoms with dangling bonds. These are the atomic orbitals that normally hybridize but now form the defect level. Similarly, an interstitial possesses unbound atomic orbitals. In order to determine the impact of a defect, it is thus necessary to take a look at the contribution of atomic orbitals to valence and conduction bands.
For LHPs, the orbital structure of the band edge states has been discussed in detail in Subsection 2.1.2. A simplified sketch of the antibonding band structure is depicted in Figure 2.5a. Atomic levels of halide, which remain when lead vacancies are formed or halides are incorporated as interstitials, are located within the valence band. Similarly, halide vacancies expose dangling lead bonds which - considering the only minor contribution of halide to the conduction band - are close to or within the conduction band.[45] As a consequence, defects in LHPs are usually shallow in nature with energy differences to the band edge states of approximately 20 meV.[95] This is in stark contrast to conventional semiconductors (Figure 2.5b), where valence and conduction band are composed of bonding and antibonding state, respectively, causing deep traps to be formed by vacancies.[13]
Thus, LHPs are considered as "defect tolerant". This does not imply that they are free of defects. On the contrary, defects are formed in perovskite as in any other material such that they possess an overall defect density of approximately 10^{15} cm^{-3}.[94] In bulk LHPs for instance, Schottky defects have been found to form as pairs of A-site and halide vacancies.[13] Theoretical investigations for LHP NCs on the other hand predicted a preferential defect formation at the surface including an easy generation of interstitials.[96] Overall, such intrinsic defects are usually shallow in nature and thus do not perturb the charge transport or optical properties significantly. This is great in terms of applications and also facilitates their fabrication, sparing the need for an extensive surface treatment.[83]
Still, deep defects do occur in LHP NCs, too. For instance, dangling bonds of excess halide

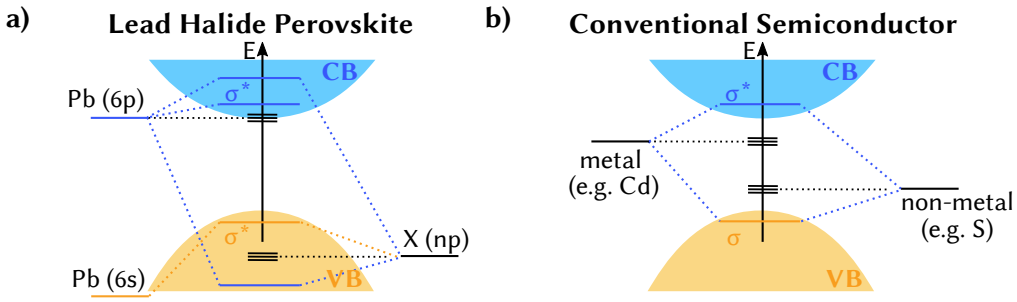

Figure 2.5: Impact of Defects in Different Semiconductors. **a** Scheme of the LHP band structure and shallow defects formed by dangling bonds. **b** Similar sketch for the band structure of conventional semiconductors, demonstrating the formation of deep traps.

at the NC surface, e.g. formed through extensive washing steps, were predicted to cause non-radiative decay.[87,96] This is in line with experimental studies showing poor luminescence for systems with large surface contributions.[26,97] Also, external doping may still cause the formation of deep traps. In this context, especially doping with bismuth has been tested[98] and reported to cause a decrease in PLQY due to formation of traps, although their nature is still under debate.[99–101]

2.2.2 Post-Synthetic Treatment of NCs

Post-synthetic treatment is a powerful tool to alter NCs once they are already formed. During such a treatment, an additive is provided to the NC dispersion and given time to interact with the surface of the NCs. One strategy is based on the partial exchange of the NCs' capping ligand for other organic molecules. This has been successfully employed to enhance the optical performance of LHP NCs,[102] induce chirality,[103] or replace insulating long-chain ligands by shorter ones to allow for an efficient charge transfer in solar cell applications.[104,105] Apart form these organic ligand modulations, treatment with metal salts, which can be seen as a ligand exchange reaction involving a metal complex,[86] take a prominent role. Thus far, this has been extensively used to enhance the optical performance and stability[26,106,107] but also induce compositional variations.[84,108]

Two important applications are depicted in Figure 2.6. Firstly, such treatments are aimed to passivate surface defects that have been identified as a reason for limitations in the PLQY of LHP NCs. Typically, the surface of inorganic LHP NCs is reported to be terminated by PbX_2 together with ammonium ligands,[109,110] as depicted in Figure 2.6a. Surface defects such as missing halide or lead atoms can then successfully be healed by supplying metal salts that are able to fill these gaps, such as $PbBr_2$,[26] $CdCl_2$,[106] or $ZnBr_2/ZnCl_2$.[107] These experimental studies are supported by theoretical investigations,[96] that predict the incorporation of metal

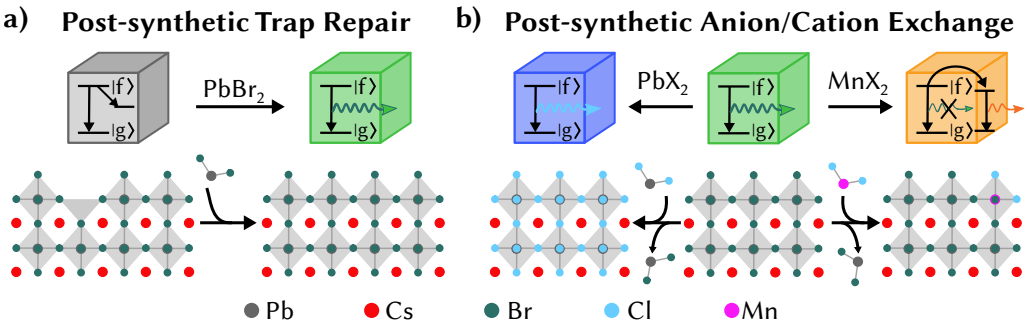

Figure 2.6: Post-Synthetic Treatments of LHP NCs with Metal Salts. **a** Surface traps provoking non-radiative recombination are effectively passivated by the post-synthetic addition of $PbBr_2$ metal salt. **b** A post-synthetic modulation of the emissive properties is feasible either by halide exchange (left), causing a shift of the band gap, or by embedding cations such as manganese (right), capable of energy transfer.

salts when present in the surrounding. Overall, the PLQY is significantly enhanced by such a treatment, e.g. from 7 % up to 42 % for LHP nanoplatelets.[26]
In addition to passivation, post-synthetic treatments have also been applied to modify the composition of NCs, exploiting the high mobility of ions within the rather soft and ionic lattice.[27] Such an exchange is depicted in Figure 2.6b. On the one hand, the halide anion can be exchanged by providing an excess of the respective PbX_2 salt.[84,108] A complete replacement based on the ease in halide diffusion[111] takes place within seconds without the need to supply energy in form of heat. Importantly, the size and shape are left unaltered upon careful treatment, enabling a direct comparison of the halide impact.[62,108] Taking its contribution to the band edge states into account, this is thus an easy method to fast and reversible adjust the band gap energy of LHP NCs. Analogously, providing a compatible metal ion is expected to result in an exchange of the cation. While this is readily feasible for the A-site cation,[112] a replacement of the divalent lead ion requires significantly more effort. Thus far, this has been mainly employed to alloy the system with Mn^{2+}. Long reaction times[113] and assistance by a concomitant halide exchange[114] allow a partial exchange. Mn^{2+} acts as a center for energy transfer with a long-lived luminescence while the NC's intrinsic luminescence is reduced.[98] Compared to in-situ doping techniques where dopants are added during material formation, such post-synthetic doping strategies are advantageous with respect to fine-tuning the luminescence and band gap energy by an easy and precise adjustment.[98]

2.2.3 Fluorescence Quenching and the Sphere of Action Model

Evidently, a NC's luminescence can be increased or decreased dependent on its interaction with the metal salt added post-synthetically. When a decrease in luminescence is induced by mechanisms that require a contact between a fluorophore and a second substance, the quencher, this is called quenching.[78] It may involve the fluorophore's ground state when it forms a non-emissive complex with the quencher. Alternatively, quenchers can act on the excited state causing a non-radiative decay, e.g. during a collisional encounter within the fluorophore's lifetime. The former is known as static and the latter as dynamic quenching.[78]
In both cases, the impact of a single quencher on a fluorophore can strongly differ. Although to-date time-resolved spectroscopy (see Section 3.4) can help to decipher interactions that cause a loss in fluorescence, the steady-state study of quenching dynamics is a simple yet powerful tool to provide such insights.
The idea of a quenching study is simple: Well defined small amounts (aliquots) of the substance suspected to cause a drop in luminescence are stepwise added to a solution containing the fluorophore (F) (Figure 2.7). Subsequent to each addition, the solution's steady-state PL intensity is determined. The as-acquired functional dependence of the PL intensity on the concentration of quencher (Q) comprises valuable information on the mechanism of

quenching. Applying this methodology, Stern and Volmer for instance identified a collision-induced deactivation of iodide luminescence in a pioneering work at the beginning of the 20th century.[115] In their honor, such concentration dependent plots are named Stern-Volmer plots. Today, this technique is e.g. exploited to characterize biological systems.[116,117] As quenching requires a physical contact, its efficiency is indicative for the relative location of Q to F and can thus be used e.g. to reveal the permeability of a membrane.[78] In addition, presence of parallel quenching processes, inhomogeneities in an ensemble of fluorophores, or information on mechanism-intrinsic properties such as diffusion or complexation constants can be acquired.[78] To enable such a quantitative analysis, a thorough description of the interaction and resultant characteristic functional dependence in the Stern-Volmer plot is needed.

Static and Dynamic Quenching: The Stern-Volmer Equation

In its simplest form, a system is subject to only one type of interaction which is similar for all fluorophores F. In such a case, the PL intensity ratio between the pristine (I_0) and quenched solution (I) is a linear function of the concentration c_Q of quencher (Q):[78]

$$\frac{I_0}{I} = 1 + K_\mathrm{SV} c_\mathrm{Q} \tag{2.15}$$

This is known as the Stern-Volmer equation whose constant K_SV is representative for the fluorophore's sensitivity to be quenched by Q.[78] The Stern-Volmer equation is universal for both, static and dynamic interactions. However, K_SV is characteristic for the type of process as detailed hereafter.

Static quenching acts on the ground state and can be described by the formation of a non-emissive complex

$$\mathrm{F} + \mathrm{Q} \xrightarrow{K_\mathrm{Q}} [\mathrm{F{-}Q}] \tag{2.16}$$

between F and Q, dictated by its association constant K_Q. This is depicted in Figure 2.7. With absorption being an instantaneous process driven by the presence or absence of a complex in the instance it occurs, only non-complexed fluorophores contribute to the emission.[78] Thus, for a solution containing a total concentration $c_{\mathrm{F},0}$ of fluorophores, the PL intensity is proportional to the fraction of non-complexed F:

$$I = I_0 \frac{c_\mathrm{F}}{c_{\mathrm{F},0}} = I_0 \frac{c_{\mathrm{F},0} - c_{[\mathrm{F{-}Q}]}}{c_{\mathrm{F},0}} \tag{2.17}$$

Here, $c_{[\mathrm{F{-}Q}]}$ refers to the amount of complexed species, which can be easily obtained from Equation 2.16 by applying the law of mass action. Together with a rearrangement, this yields a Stern-Volmer equation with $K_\mathrm{SV} = K_\mathrm{Q}$. As such, the dependence of the PL intensity is indicative for the complex formation in case of static quenching.

For dynamic quenching, the Stern-Volmer constant is instead linked to the diffusion of F and Q (see Figure 2.7). This is due to the quencher's action on the excited state, which can take place at any point during the fluorophore's lifetime. In other words, encounters are caused even for those F not connected to a Q at the moment of excitation dependent on the distance Q can diffuse during the lifetime of F. Deactivation from the excited state can thus be described by a non-radiative decay channel for the F-Q interaction that depends on this diffusion:[78]

$$\left(\frac{\mathrm{d}n_f}{\mathrm{d}t}\right)_{\mathrm{rel,Q}} \overset{\uparrow}{=} -\tau_0^{-1} n_f - K_\mathrm{q} c_\mathrm{Q} n_f \qquad (2.18)$$

Equation 2.10

Here, the lifetime τ_0 is representative for deactivation in absence of Q, and the second term describes the deactivation due to F-Q collisions. It considers that the probability for an encounter scales with the concentration of Q, while the quenching rate $K_\mathrm{q} = f_\mathrm{Q} k_0$ depends on a diffusion-driven encounter rate k_0 and the efficiency f_Q to result in deactivation. The former has been described e.g. by Smoluchowski,[118] establishing a link to the diffusion constant. The emission intensity for a process described by Equation 2.18 can then be determined by the

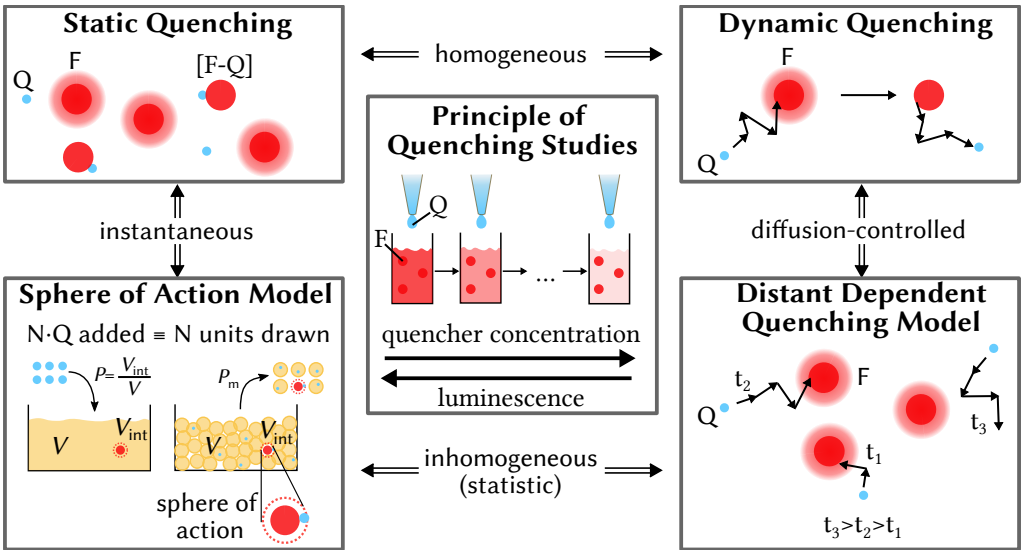

Figure 2.7: Luminescence Quenching Models. A quenching experiment (center), monitors the loss in luminescence of a solution with fluorophores (Fs) upon stepwise addition of aliquots of quencher (Q). Static quenching (top left) refers to complex formation with F in the ground state. This instantaneous homogeneous process occurs with the same probability for all F. Dynamic quenching (top right) is a homogeneous, diffusion-controlled quenching of the excited state of F. Inhomogeneous interactions result from the statistic distribution and motion of Q with respect to F. The former (bottom left) causes an apparent static quenching described by the "Sphere of Action model" by immediate deactivation once one Q is present in a defined sphere of action of F. The latter (bottom right) results in a distribution of points in time (t_1, t_2, t_3) at which F is deactivated by interaction with Q, described by the distant dependent quenching (DDQ) model.

ratio of the radiative to overall decay rate, similarly to the determination of the PLQY:

$$\frac{I}{I_0} = \frac{\tau_0}{\tau_0 + f_Q k_0 c_Q} \tag{2.19}$$

Rearrangement again yields the Stern-Volmer equation, now with a constant $K_{SV} = f_Q k_0 \tau_0^{-1}$ driven by the recombination and diffusion of F and Q in solution.[78]
The preceding analysis has successfully established an interpretation of the Stern-Volmer constant K_{SV} to unravel parameters detrimental for either the static or dynamic quenching mechanism. Naturally, this requires to know which mechanism is present. In view of their similar functional dependence in the Stern-Volmer plot (Equation 2.15), additional evidence is needed, as e.g. provided by a perturbation in the absorbance for static quenching or a temperature dependent analysis.[78] Alternatively, concomitant lifetime measurements are a handy tool to tell static and dynamic processes apart. A change in lifetime is absent for static quenching given its ground state interaction. In contrast, for dynamic quenching the lifetime decreases to the same extent as the PL intensity due to action on the excited state.[78]

The Sphere of Action and Distant Dependent Quenching Models

Static and dynamic quenching with the characteristic Stern-Volmer equation described thus far merely form the basis of analyzing more complex quenching mechanisms. For instance, the two basic interactions are not mutually exclusive but may occur at the same time. The reduction in intensity by both, complexation and collision, provokes a quadratic contribution in the Stern-Volmer plot and thus superlinear behavior.[78] On the other hand, situations such as the presence of fluorophores outside and inside of a non-permeable membrane may result in a sublinear behavior based on fluorophores subject to different extents of quenching.[78] Even when equally well accessible, an identical interaction of all fluorophores with the quenchers Q is only an idealized model. In reality, non-identical interactions occur as a consequence of the statistic nature of the process. This gets important when quenching is strong, i.e. for specific quencher-fluorophore combinations, and always when a large amount of Q is added.[78]

For a start, quenchers are statistically distributed in the solution, which is described by the so called “Sphere of Action” model proposed by F. Perrin.[119] When present in the vicinity of a fluorophore at the moment of excitation, the probability for a direct collision that causes an immediate deactivation is high.[78,120] In consequence an apparent static quenching occurs, as mainly those fluorophores F without any quenchers Q in their surrounding contribute. Thus, it is necessary to determine the probability of Q to be present within the vicinity of F. The addition of N quenchers Q that statistically distribute in the solution is equivalent to an urn model, as sketched in Figure 2.7. The probability to find a certain number m of Q within

a small volume fraction V_{int} of the total solution volume V is given by

$$P_{\mathrm{m}} = \binom{N}{m}(P)^m (1-P)^{N-m} \approx \frac{(N \cdot P)^m}{m!}\mathrm{e}^{-N \cdot P} \tag{2.20}$$

where $P = V_{\mathrm{int}}/V$ accounts for the probability of Q to end up in the volume V_{int}. The first term is the binomial distribution, which is defined by the possibility that m quenchers Q end up in the volume fraction, while $N - m$ do not. As the quenchers are not distinguishable, only their number that ends up in the volume V_{int} is relevant and the binomial coefficient $\binom{N}{m}$ thus sums all possible permutations. The approximation of the binomial by a Poisson distribution (second term) is valid provided that the total added amount of quenchers $N \gg 1$, and the probability to end up in the volume fraction V_{int} is sufficiently small, i.e. $P \ll 1$.
The relevant volume fraction V_{int} defining the vicinity of F is the so-called "sphere of action" (see Figure 2.7), giving the model its name.[78,120] Usually, the radius of the sphere of action is equal or only slightly larger than the sum of the radii of F and Q,[78] such that the condition $P \ll 1$ is well fulfilled. In the limiting case of 100 % quenching efficiency for a quencher present in the sphere of action, the PL intensity is strictly reduced to the fraction of F without any Q.[119,120] Then, the Stern-Volmer plot is characterized by an exponential instead of a linear behavior:

$$I = I_0 P_0 \underset{\text{Equation 2.20}}{=} I_0 \mathrm{e}^{-N \cdot V_{\mathrm{int}}/V} = I_0 \mathrm{e}^{-c_{\mathrm{Q}} \mathrm{N_A} V_{\mathrm{int}}} \tag{2.21}$$

with $\mathrm{N_A}$ as Avogadro's number. Usually, dynamic quenching due to diffusion adds on top, unless the mobility of Q is strongly limited. In rigid polymer solutions, for instance, diffusion is so slow that dynamic encounters within the fluorescence lifetime play no role and only the quencher's statistic distribution is relevant such that a pure dependence as shown in Equation 2.21 is observed.[121]

While the Sphere of Action model takes care of an inhomogeneous distribution of Q with respect to F at the moment of excitation, the diffusion process characterizing the dynamic quenching is subject to statistical variation, too (see Figure 2.7). This arises from the random Brownian motion of Q during the lifetime of F. In deriving the Stern-Volmer equation, a constant encounter rate k_0 independent of the starting positions of F and Q and elapsed time has been assumed. However, this is only true in the limit of a strongly diluted solution. In reality, those fluorophores F with a larger distance to the next quencher Q at the moment of excitation will remain in the excited state longer. Likewise, with elapsing time also F with Q nearby are less likely to be stricken, since there is a chance that Q diffuses away.[78,122] The effect of the random motion of Q has been taken into account for the first time in a theoretical description based on a time-dependent quenching rate $K_{\mathrm{q}}(t)$ by Smoluchowski[118] and applied to quenching of fluorescence by Sveshnikoff.[123] With elapsing time, the encounter rate converges to the diffusion-limited value assumed in the limit of low concentration.[124]

Later, the description has been refined to include an additional distance dependence of the encounter rate. This so-called DDQ model accounts for the fact that an orbital overlap is already sufficient for quenching to occur, while Smoluchowski assumed that F and Q need to collide.[78]
The overall complex description is able to account for two effects that characterize such type of diffusion controlled quenching: firstly, the Stern-Volmer plot shows a superlinear behavior with a dependence on the diffusion constant. Secondly, the time dependent PL intensity decay is not a simple exponential anymore, but characterized by a relation dependent on the quencher's concentration c_Q and time-dependent quenching rate $K_\mathrm{q}(t)$ as[78,122]

$$I(t) = I_0 \mathrm{e}^{-\frac{t}{\tau_0}} \exp\left(-c_\mathrm{Q} \int_0^t \mathrm{d}t K_\mathrm{q}(t)\right) \tag{2.22}$$

with other constants having the same meaning as in Equation 2.19. Usually, there are no analytical solutions for these equations anymore but numerical methods are necessary to fit the time dependent PL intensity.[78] A significant change in lifetime with quencher concentration is however already a characteristic feature that can help to tell inhomogeneous quenching based on the quencher's distribution (Sphere of Action model) and diffusion (DDQ model) apart.

Overall, quenching has been presented as a simple but potent method to obtain mechanistic insight when carefully applied and analyzed. Specifically, the dependence of quenching on diffusion or complex formation can be exploited to identify factors that govern a fluorophore's environment. It shall be noted, that the preceding theoretical description has been developed for molecular fluorophores deactivated by collisions. In a solid-state picture applicable to QDs, such models need to be slightly refined, as I will show in Chapter 4.

2.3 Physical Modification of a NC Surrounding

Thus far, modulation of optical transitions in QDs by chemical means has been introduced. This has shown to open up additional decay channels, modifying the emission rate. Here, an alternative pathway shall be discussed that can serve to equip LHP QDs with new functionalities: directly changing the transition probability Γ_fg as introduced in Equation 2.6 allows to modulate both, the emission but also the absorption process. Such an impact can be induced by a physical modification, e.g. a well defined modulation of the electromagnetic radiation field. A more explicit description of the transition probability Γ_fg in terms of such light-matter interactions thus needed to be established in Subsection 2.3.1 prior to presenting metamaterials as an artificial material class capable of performing such a change in Subsection 2.3.2. Specifically, modulation of polarization is then discussed in Subsection 2.3.3.

2.3.1 Fermi's Golden Rule

In a quantum mechanical sense, absorption or emission of radiation is a perturbation of a system due to its coupling with the electromagnetic radiation field. Derived from the time-dependent Schrödinger equation in the limit of a weak perturbation, the transition probability Γ_{fg} can be expressed by Fermi's Golden Rule:[125]

$$\Gamma_{\mathrm{fg}} = \frac{2\pi}{\hbar}|\langle f|H'|g\rangle|^2 \rho(\omega) \cdot \delta(E_{\mathrm{f}} - E_{\mathrm{g}} - \hbar\omega) \tag{2.23}$$

Herein, H' denotes the Hamiltonian of the perturbation. The matrix element $\langle f|H'|g\rangle$ thus defines the coupling of a transition between a ground state $|g\rangle$ and excited state $|f\rangle$ or vice versa by the radiation field. The latter is characterized by a multitude of possible photon modes. All modes matching the energy difference between excited state and ground state, i.e. $E_{\mathrm{f}} - E_{\mathrm{g}} = \hbar\omega_{\mathrm{fg}}$, may cause a coupling. Matching modes are selected by considering the respective density of photon states $\rho(\omega)$ present in excitation or emission at a certain frequency ω in combination with the delta-function. It shall be noted, that the above equation accounts for the transition only between two separate states. Thus, for bulk semiconductors, Fermi's Golden Rule has to be expanded by the joint density of states $\rho_{\mathrm{fg}}(\omega)$ that respects the coupling of the multitude of states of the quasi-continuum to the radiation field. However, as discussed previously, weakly confined QDs as investigated within this thesis are characterized by an energy landscape composed of a set of separate excitonic states and are thus well described by Equation 2.23.
In order to make use of Fermi's Golden Rule, the matrix element $\langle f|H'|g\rangle$ needs to be defined. Often, the interaction Hamiltonian can be treated in terms of the electric dipole approximation as $H' = -\boldsymbol{\mu}|\boldsymbol{E}|\hat{e}$ (see Appendix for more details).[90] It depends on the amplitude of the light's electric field vector $\boldsymbol{E}$ and the orientation of its unit vector $\hat{e}$ towards the dipole moment operator $\boldsymbol{\mu}$ characterizing the transition. With this, the probability to excite a QD to an excitonic state $|X_{\mathrm{i}}\rangle$ with energy $E_{X_{\mathrm{i}}} = \hbar\omega_{X_{\mathrm{i}}}$ upon interaction with a radiation field is given by:

$$\Gamma_{X_{\mathrm{i}}} \propto |\boldsymbol{E}(\omega_{X_{\mathrm{i}}})|^2 |\langle\psi_{\mathrm{c}}|\hat{e}\boldsymbol{\mu}|\psi_{\mathrm{v}}\rangle|^2 \rho(\omega_{X_{\mathrm{i}}}) \tag{2.24}$$

Evidently, three factors of the radiation field can impact an absorption or emission process: the amplitude of the electric field vector $\boldsymbol{E}$, the orientation with respect to the dipole moment operator (the matrix element is also referred to as electric transition dipole moment), and finally the spectral density of photon states.

All three factors can change dependent on the surrounding provided for the QD, e.g. by placing it in a cavity.[126] Specific substrates where the QD is placed upon can serve this purpose. For instance, the local density of photon states $\rho(\omega_{\mathrm{em}})$ at the emission frequency

ω_{em} can be significantly altered when the emitter is located at a surface or in a cavity.[127] This effect has been first noticed by Purcell, who related the observation of an accelerated decay of an excited nuclear magnetic transition in paraffin within a cavity to the resonant coupling with only a single mode provided by an electrical circuit.[128] The change in transition probability Γ_{cavity} and thus decay rate τ_{cavity} versus the free-space values has been quantified by what is now called Purcell factor:[125]

$$F_{\mathrm{P}} = \frac{\Gamma_{\mathrm{cavity}}}{\Gamma_{\mathrm{free}}} = \frac{\tau_{\mathrm{free}}}{\tau_{\mathrm{cavity}}} \tag{2.25}$$

Such effects are already present in comparable simple setups. Demonstrated by Drexhage in the 1960s,[129] an emitter's lifetime gets a function of its distance to a mirror surface as a result of altering the number of possible photon modes emission can occur to. Likewise, the absorption process can be manipulated. Changes in the electric field energy density u_ω of the excitation light at the location of the emitter, i.e. a modulated near field at a substrate, will impact the transition probability, given that $u_\omega \propto |\boldsymbol{E}(\omega)|^2$.[125] In other words, also a material's absorption coefficient $\alpha \propto \Gamma_{\mathrm{X_i}}$ can be directly modulated by the surrounding.
Finally, as a note, the as obtained dependencies account for linear processes only. For non-linear excitations, second order perturbation theory has to be taken into account.[130] The simple matrix element in Fermi's Golden Rule $|\langle f|H'|g\rangle|^2$ is then replaced by a more complex term. For a two-photon absorption process mediated by an intermediate state $|m\rangle$ with energy E_{m}, the transition probability is given by:[130]

$$\Gamma_{\mathrm{fg}} \propto |\boldsymbol{E}(\omega)|^4 \left| \sum_m \frac{\langle f|\hat{\boldsymbol{e}}\boldsymbol{\mu}|m\rangle\langle m|\hat{\boldsymbol{e}}\boldsymbol{\mu}|g\rangle}{E_{\mathrm{m}} - E_{\mathrm{g}} - \hbar\omega} \right|^2 \tag{2.26}$$

The sum considers all possible states within the quantum mechanical system. Transitions to these states, characterized by an energy expense of $E_{\mathrm{m}} - E_{\mathrm{g}}$, are weighted with respect to their energy missmatch to the excitation light ($\hbar\omega$). Evidently, a dependence on the electric field amplitude to the power of four and thus a quadratic dependence on the light's intensity, as already mentioned in Section 2.1, is obtained. As such, these processes offer an increased sensitivity when a modulation is applied by the surrounding.

2.3.2 Metasurfaces for Tunable Light-Matter Interactions

Modulations of the aforementioned properties – the electric field energy density or the local density of photon states – can be best achieved with materials characterized by precisely defined light-matter interactions. Specific interactions do not only result from the material's composition, but can instead be deliberately generated by patterning matter.[131,132] Nature holds manifold examples of such patterns. Microstructures are e.g. the reason for the colors in

butterfly wings or responsible for the enriched visual capability of aquatic animals.[133] Today, this concept can also be exploited to create artificially structured matter.
One class of artifical materials are metamaterials as shown in Figure 2.8. Metamaterials – a coined word for "beyond" conventional materials – are composed of building blocks on the nanoscale, i.e. smaller than the wavelength of light the material is interacting with.[134] Generally, the building blocks, named metaatoms, can have an arbitrary shape and material, ranging from metals such as gold or silver[135] to dielectrics such as titanium dioxide, silicon or even LHPs.[136,137] A metamaterial is then formed by an arrangement of these metaatoms in one, two or three dimensions. Especially two-dimensional metamaterials, named metasurfaces, have emerged at the spotlight due to their unique optical properties, while being easier to fabricate than their three-dimensional counterparts.[137] Light that strikes such a surface interacts with the individual subwavelength building blocks and gets further influenced by their arrangement. Although not mandatory, these arrangements are often periodic and characterized by the metaatom's distance p, the so called pitch.[131] The defined light-matter interactions that result for such metasurfaces are now detailed.

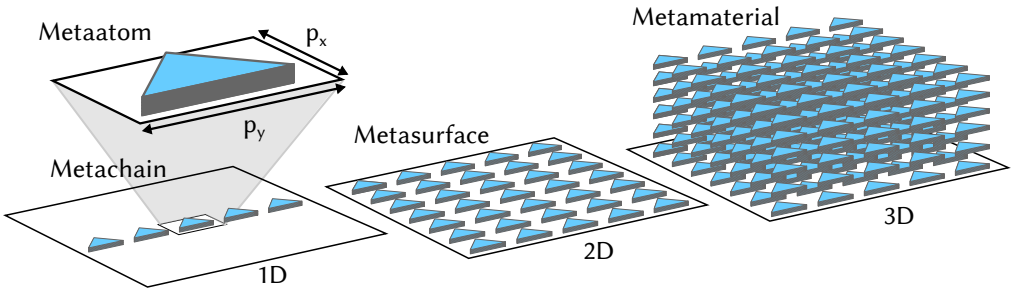

Figure 2.8: Formation of Metamaterials from Metaatoms. A metaatom constitutes a building block, from which metachains, metasurfaces and metamaterials are formed by arrangement in one-, two- and three dimensions, respectively, with the lattice's periodicity defined by the pitch p_x/p_y. Adapted from [131]

A classical treatment of light by its electromagnetic nature in terms of Maxwell's equations forms the basis for a description. In the absence of external charges or currents, Maxwell's equations are defined by:[138]

$$\nabla \cdot \boldsymbol{B} = 0 \qquad \text{(Gauss´s Law of Magnetism)} \tag{2.27a}$$

$$\nabla \cdot \boldsymbol{D} = 0 \qquad \text{(Gauss´s Law)} \tag{2.27b}$$

$$\nabla \times \boldsymbol{E} = -\frac{\partial \boldsymbol{B}}{\partial t} \qquad \text{(Faraday´s Law)} \tag{2.27c}$$

$$\nabla \times \boldsymbol{H} = \frac{\partial \boldsymbol{D}}{\partial t} \qquad \text{(Ampere´s Law)} \tag{2.27d}$$

Here, $\boldsymbol{B} = \mu_0 \mu \boldsymbol{H}$ is the magnetic flux density, which is linked to the magnetic field $\boldsymbol{H}$ by the vacuum permeability μ_0 and the characteristic relative permeability μ of the material. Likewise,

the dielectric displacement $\boldsymbol{D} = \epsilon_0 \epsilon \boldsymbol{E}$ is linked to the electric field $\boldsymbol{E}$ and the material's relative permittivity ϵ by a similar constitutive equation. A wave equation for light can be obtained by combination of Maxwell's equations, whose plane-wave solution is given by:[138]

$$\boldsymbol{E} = \boldsymbol{E}_0 \mathrm{e}^{i(\boldsymbol{kr} - \omega t + \varphi)} \tag{2.28}$$

It describes the propagation of an electromagnetic wave with amplitude $|\boldsymbol{E}_0|$, wavevector $\boldsymbol{k}$, frequency ω, and phase φ. Additionally, the polarization of the light, a property discussed in more detail in Subsection 2.3.3, is related to the vector nature of $\boldsymbol{E}_0$. The frequency $\omega = k_0/c_0$ is defined according to the light's dispersion by the vacuum values of the wavevectors's amplitude k_0 and the speed of light c_0. In media, both, the speed of light $c = c_0/n$ and the wavevector's amplitude $k = k_0/n$ are reduced by the real part of the refractive index $n = \sqrt{\epsilon\mu}$, which is linked to the material's relative permittivity and permeability. For non-magnetic media, $\mu \approx 1$. Generally, ϵ is a complex number. In non-absorbing media, ϵ and and thus $n \approx \sqrt{\epsilon}$ however reduce to only real numbers and shall be considered as such hereafter.[138]

When a plane wave as described in Equation 2.28 approaches a boundary between two media structured by a metasurface, it is exposed to an abrupt change in phase, amplitude or polarization at this interface.[134] The consequence of a phase change modulated across the interface is evident in Figure 2.9a. Waves emerge from each point at the surface according to Huygens's principle.[139] The shown metasurface consists of microscopic scatteres that each induce a variable phase shift $\Delta\varphi(x)$ to the emerging wave dependent on the position x along

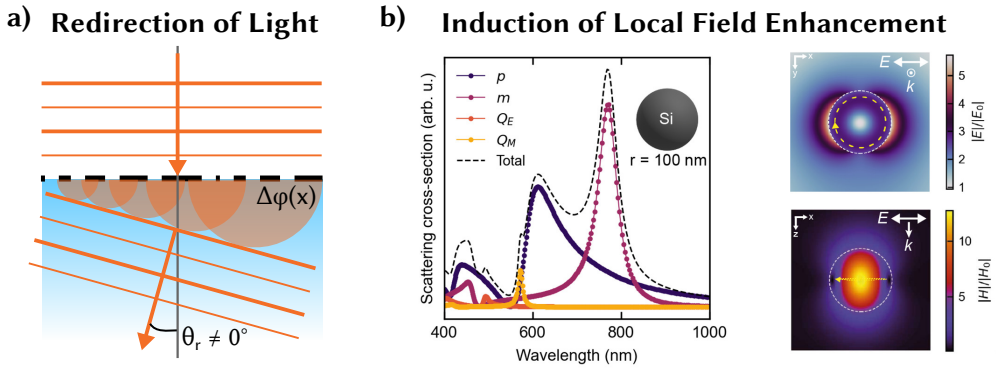

Figure 2.9: Light-Matter Interactions at Metasurfaces. a A metasurface (black) at an air-glass interface induces a variable phase shift $\Delta\varphi(x)$ by arranging different scatterers, which causes a light beam (orange) to be redirected at an angle $\theta_r \neq 0$ even for normal incidence, constituting an anormal refraction and reflection behavior. **b** For subwavelength metaatoms such as a silicon sphere with 100 nm diameter, light is scattered with its crosssection spectrally modulated by the resonant excitation of electric and magnetic dipole (*p*,*m*) and quadrupole (Q_E, Q_M) resonances, respectively (left). In consequence, enhanced electric and magnetic fields are present in the near field, depicted exemplary for the electric and magnetic dipole modes (left). Reproduced from [131]

the surface. Thus, the resultant wavefront does not follow the simple refraction law of Snellius anymore (i.e. $\theta_r \neq 0$ at normal incidence).[140,141] Instead, the light beam can be redirected at will, dependent on the configuration of scatterers present at the interface. Based on Fermat's principle of path minimization for light crossing an interface, Snellius's law can be expanded to obtain a rigorous prediction of the anomalous reflection and refraction behavior.[134,142] This ability to shape and redirect beams is at the heart of metasurface applications such as metalenses[143] or separation of beams dependent on polarization.[144]

Apart from redirection of light, metasurfaces also possess well defined electric fields in their surrounding, as every metaatom acts as an antenna for the impinging light.[29] Charge carriers within the metaatoms respond to the oscillating electric and magnetic field and are induced to collective oscillations themselves. In a first approximation, this interaction can be treated as an induction of electric and magnetic dipole moments within the metaatom, $\boldsymbol{\mu}$ and $\boldsymbol{m}$, related to the electromagnetic field by a polarizability tensor $\overleftrightarrow{\alpha}$:[29]

$$\begin{pmatrix} \boldsymbol{\mu} \\ \boldsymbol{m} \end{pmatrix} = \overleftrightarrow{\alpha} \begin{pmatrix} \boldsymbol{E} \\ \boldsymbol{H} \end{pmatrix} = \begin{pmatrix} \alpha_{\mathrm{E}} & \alpha_{\mathrm{EH}} \\ \alpha_{\mathrm{HE}} & \alpha_{\mathrm{H}} \end{pmatrix} \begin{pmatrix} \boldsymbol{E} \\ \boldsymbol{H} \end{pmatrix} \tag{2.29}$$

The response to an electric field, α_{E}, is sensitive to the metaatom's size, shape, and material composition which can thus be tailored accordingly. The cross coupling terms, α_{EH} and α_{HE}, couple the electric and magnetic response with a defined phase relation.[29] This is a prerequisite to achieve chirality, a structural property closely linked to polarization dependence as detailed in Subsection 2.3.3.

The dipole moment oscillates in time and for objects much smaller than the wavelength, this acts as a point dipole source that radiates light in terms of a dipole field. In effect, the impinging light is thus scattered on the subwavelength sized metaatoms dependent on their polarizability.[138] At certain frequencies, the polarizability and as such the dipole field in the vicinity of the metaatom is maximized. These resonances are specific for each metaatom and are visible in its optical spectrum, as demonstrated in Figure 2.9b for a silicon sphere. Each resonance can be a simple dipole mode but also a more complex mode like a quadrupole. While in metals collective dipole oscillations of conduction electrons termed local surface plasmon resonances are mainly induced by the electric field, the response of dielectric materials is more rich as both, electric and magnetic fields couple to the metaatom.[131] This is evident in Figure 2.9b, where the spectrum contains various modes, which can be each associated with a field distribution around the metaatom, shown here for the electric and magnetic dipole resonances. This apparent field enhancement in the near field of the nanoscale scatterer, i.e. at distance $r \ll k^{-1}$, is key for their utilization in sensing applications or alike.[131,138] It shall be noted, that treatments beyond the dipole approximation, are often necessary to describe such multipoles and resultant electric or magnetic fields in the vicinity of the metaatom. This may

be achieved i.e. by Mie theory, or in common practice often directly by solving Maxwell's equations on a mesh around the structure by means of numerical methods.

On a metasurface, the situation thus far depicted merely for a single metaatom is additionally complicated by the fact that metaatoms do not behave as separate scatterers, but interact with each other due to their proximity in the lattice. Thus, each metaatom is not only driven by the impinging light field, but additionally by the scattered fields and near-fields of its neighboring metaatoms. The description of the dipole moment for a single metaatom in Equation 2.29 thus needs to be expanded to include the interaction of a metaatom i, located at $\boldsymbol{r}_\mathrm{i}$, with other metaatoms j, located at $\boldsymbol{r}_\mathrm{j}$:[29]

$$\begin{pmatrix} \boldsymbol{\mu} \\ \boldsymbol{m} \end{pmatrix}_\mathrm{i} = \overleftrightarrow{\alpha}_\mathrm{i} \left[\begin{pmatrix} \boldsymbol{E} \\ \boldsymbol{H} \end{pmatrix} (\boldsymbol{r}_\mathrm{i}) + \sum_{i \neq j} \overleftrightarrow{G}(\boldsymbol{r}_\mathrm{i}, \boldsymbol{r}_\mathrm{j}) \begin{pmatrix} \boldsymbol{\mu} \\ \boldsymbol{m} \end{pmatrix}_\mathrm{j} \right] \tag{2.30}$$

Dipole-dipole interactions between metaatoms are characterized by the Green function $\overleftrightarrow{G}(\boldsymbol{r}_\mathrm{i}, \boldsymbol{r}_\mathrm{j})$. Overall, this constitutes a set of equations, one for each metaatom, all dependent on each other and characteristic for a certain arrangement. This additional interaction equips the user with a large playground for modifications and thereby tunability of e.g. near field enhancement. A comparable simple example are Bragg diffractions, which can give rise e.g. to surface plasmon resonances in metallic arrays. In such a scenario, the single metasurface resonances get coupled to each other due to in-plane diffraction orders of the periodic structure.[131] Resonances occur when the wavelength present in the surrounding medium, i.e. the substrate or the air slab, matches the pitch p of the metasurface, i.e. $p = \lambda_0/n$ with n as the refractive index of the medium. Such surface plasmon resonances can give rise to narrow line widths and significantly enhanced near field intensities.[145] Often however, higher order Bragg diffractions are unwanted and then the pitch multiplied with the refractive index is kept smaller than the wavelength of light it is interacting with.[146]
The interaction in metasurfaces can cause the evolution of complex behaviors that can be precisely tuned. For instance, metasurfaces have been reported that support bound states in the continuum,[147,148] characterized by extremely sharp resonances within the mid-infrared. This has been demonstrated to hold huge potential for molecular sensing.[147] Other systems, composed of silicon nanopillars[149] and lately also LHP,[150] have proven to be applicable as antireflection coatings. Furthermore, metasurfaces have recently been tested for coding information and also boosting interaction of light with atomically thin two dimensional materials.[137] Finally, the combination of metasurfaces with emitters to enhance both, absorption and emission, has been explored.[29] This includes several combinations with LHP films, demonstrating e.g. large Purcell enhancement factors for their emission[30] or an enhanced two-photon absorption.[151] In the context of combining metasurfaces with emitters, the pos-

sibility to directly address different polarization states is intriguing. An introduction to the polarization of light and its control by metasurfaces is thus provided in the next section.

2.3.3 Controlled Interactions with Polarized Light

The electric field of a light wave, as defined in Equation 2.28, is a vector quantity that adopts a certain orientation as a function of time and location along the wave's axis of propagation. The pattern obtained by this timely variation in space at a fixed location is called its polarization.[139] When the pattern rapidly changes on the order of the decay time of emitters (approx. 10^{-8} s), the light is randomly polarized. This is e.g. the case for sun light. However, coherent light sources possess well defined patterns which can be described by decomposing the electric field vector in its amplitude E_0 and a normalized Jones vector $\boldsymbol{J}$ representative for the polarization:[139]

$$\boldsymbol{E}_0 = \begin{pmatrix} E_x \\ E_y \end{pmatrix} = \begin{pmatrix} E_{0,x} e^{i\varphi_x} \\ E_{0,y} e^{i\varphi_y} \end{pmatrix} =: E_0 \boldsymbol{J} \tag{2.31}$$

The vector components E_x and E_y are generally complex numbers, defined here for a wave propagating in z-direction in the usual Cartesian coordinate system. The normalized Jones vector $\boldsymbol{J}$ therefore contains the phase information of the two components with respect to each other. In Figure 2.10, a few important distinguished polarization states are presented. Both, their Jones vectors and the timely traces of the respective electric field vector's tip within the xy-plane are shown when viewed along the axis of propagation.
First of all, Jones vectors with only real numbers correspond to linear polarized light. The electric field vector oscillates on a straight characterized by its angle α towards the x-axis. Together with the propagation direction, this spans the plane of polarization. Secondly, one component of the Jones vector may be complex. This describes elliptically polarized

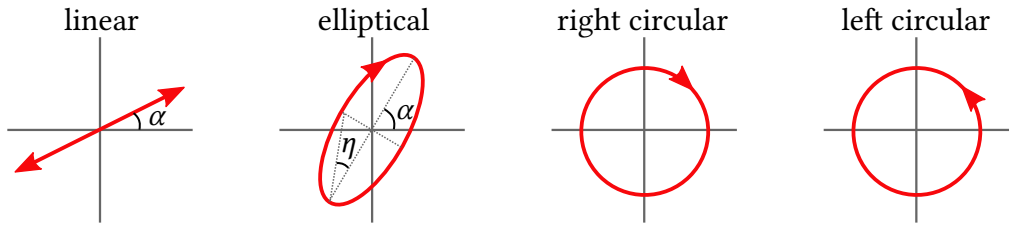

$$J = \begin{pmatrix} \cos\alpha \\ \sin\alpha \end{pmatrix} \qquad J = \begin{pmatrix} \cos B \\ e^{i\delta} \sin B \end{pmatrix} \qquad J = \frac{1}{\sqrt{2}} \begin{pmatrix} 1 \\ -i \end{pmatrix} \qquad J = \frac{1}{\sqrt{2}} \begin{pmatrix} 1 \\ +i \end{pmatrix}$$

$$\text{with } \tan\delta = \frac{\tan 2\eta}{\sin 2\alpha},\ B = \left| \arctan \sqrt{\frac{1-\cos 2\eta \cos 2\alpha}{1+\cos 2\eta \sin 2\alpha}} \right|$$

Figure 2.10: Selected Polarization States of Light. The trace performed by the electric field vector's tip is depicted in the xy-plane with the respective normalized Jones vector given beneath.

light, i.e. the vector moves at an elliptical track with a right or left handed rotation. The ellipse's orientation in the xy-plane is characterized again by the orientation angle α, while an additional angle η is a measure for its ellipticity. The normalized Jones vector can be directly described by these parameters as stated in Figure 2.10.[152] Positive values of η denote a left-handed anti-clockwise rotation, while negative values represent the right-handed clockwise direction. The sign represents the beam's helicity. The two border cases, $\eta = +45^\circ$ and -45°, are left- and right circularly polarized (CP) light, respectively, where the vector's tip moves at a circular track. Similarly to the xy-basis chosen in Equation 2.31, these two states form a basis set. Therefore, every polarized light can be described as a superposition of right and left circularly polarized states.[139]

Most matter is not sensitive to an interaction with left compared to right CP light. LHP NCs, for instance, possess two degenerate band edge states that can be separately addressed with CP light of different handedness, however, the probability for excitation is equivalent.[52,153] Yet, there is a broad range of applications that benefit from a difference in interaction with CP light. CP light sources may, for instance, be applied in 3D imaging and also potentially in quantum computing, while polarization sensitive absorption can serve for selective sensors for biological systems.[153] Thus, efforts have been undertaken to equip materials such as LHP with a sensitivity for CP light. A difference in absorption of polarized light is referred to as dichroism. The word originates from the fact that specific minerals such as tourmaline expose two colors dependent on the direction they are viewed at. This has been linked to their polarization and wavelength selective absorption of linearly polarized light dependent on its orientation towards a specific crystal axis.[139] Similar to this linear dichroism, natural occurring materials can possess a circular dichroism, although the effect is usually several orders of magnitude smaller.[154] Such an effect is observed for many physiologically relevant bio molecules, ranging form sugars over amino acids up to the DNA itself.[153,155] All these molecules lack an intrinsic mirror plane, i.e. they are characterized by structural handedness termed chirality.[154]

As a consequence of chirality, optical transitions ($|g\rangle \rightarrow |f\rangle$) within these materials are supported that are characterized by a simultaneous electric and magnetic perturbation in terms of a Hamiltonian $H' = -\boldsymbol{\mu}\boldsymbol{E} - \boldsymbol{m}\boldsymbol{B}$. Here, $\boldsymbol{\mu}$ and $\boldsymbol{m}$ are the induced electric and magnetic dipole moments, respectively.[154] With Fermi's golden rule as defined in Equation 2.23, the resultant difference in absorption coefficients of left and right CP light can thus be estimated as:[154]

$$\begin{aligned}\Delta\alpha_{\mathrm{CP}} &= \alpha_{\mathrm{LCP}} - \alpha_{\mathrm{RCP}} \\ &\propto \left(\langle g|\boldsymbol{\mu}|f\rangle\hat{e}_{\mathrm{RCP}}\langle f|\boldsymbol{m}|g\rangle\hat{b}_{\mathrm{LCP}} - \langle g|\boldsymbol{\mu}|f\rangle\hat{e}_{\mathrm{LCP}}\langle f|\boldsymbol{m}|g\rangle\hat{b}_{\mathrm{RCP}}\right) \\ &\propto \mathrm{Im}(\langle g|\boldsymbol{\mu}|f\rangle \cdot \langle f|\boldsymbol{m}|g\rangle)\end{aligned} \tag{2.32}$$

This relation is known as the Rosenfeld equation, named after the author who introduced this theoretical description,[156] later extended to a rigorous treatment of chiral media by elec-

trodynamics with chiral constitutive equations $\boldsymbol{D}(\boldsymbol{E}, \boldsymbol{H})$ and $\boldsymbol{B}(\boldsymbol{H}, \boldsymbol{E})$.[155] In its derivation, the definition of the unit vectors $\hat{e}$ and $\hat{b}$ of the electric and magnetic field in terms of CP light (see Figure 2.10) and their orthogonality has been utilized. Notably, a difference in absorption is obtained only when the respective electric and magnetic transition dipole moments are non-perpendicular towards each other. Thus, this establishes a criterion for the occurrence of circular dichroism.

The behavior can be mimicked at a metasurface: As evident from Equation 2.29, the electric and magnetic dipole moments induced within a metaatom are non-orthogonal if the off-diagonal terms of the polarizability tensor $\overleftrightarrow{\alpha}$ are non-zero. Thus, these terms that couple the electric and magnetic response enable a control of the interaction with CP light. A metasurface's response includes absorption within the structure, but likewise the scattering ability and thus the near field intensities carry such a discrimination of CP light. The presence is closely linked to structural chirality. This is exemplary shown in Figure 2.11a for a split ring resonator, a curved metaatom made of gold. For an excitation parallel to the gap with a

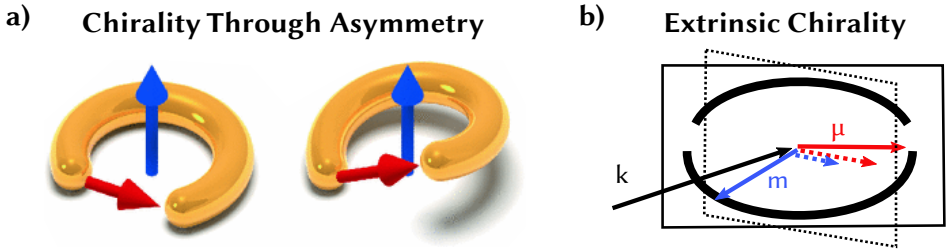

Figure 2.11: Chiral Effects of Metaatoms. a An intrinsically chiral, i.e. asymmetric metaatom, gives rise to a non-zero product of electric(red) and magnetic (blue) dipole moments. Reproduced from [155] **b** Demonstration of extrinsic chirality, evolving upon non-normal incidence due to parallel components of electric and magnetic dipole moments, $\boldsymbol{\mu}$ and $\boldsymbol{m}$, within the plane perpendicular to the beam. Adapted from [157]

normal incident beam, an electric dipole moment evolves between the tips, while a magnetic dipole moment is found perpendicular to the metaatom.[155] If one end of the metaatom is bent out of the plane chirality is created, and only then magnetic and electric dipole moments are non-perpendicular to each other. Thus, asymmetric metaatoms and in consequence also asymmetric metasurfaces are prone to show a selective interaction with left and right CP light based on such a coupling of electric and magnetic dipole moments.[155,158] However, for planar symmetric objects such a coupling may also evolve, as shown in Figure 2.11b.[157] The key to this extrinsic chirality is an asymmetric arrangement of the complete system, i.e. considering both, the object and the illumination source.[157] In the plane normal to the beam, parallel components of the electric and magnetic dipole moment are obtained. In other words, extrinsic chirality is possible for non-normal illumination with respect to the symmetry axis of the metasurface.

While the effective CP polarized discrimination, also termed chiral discrimination, achieved in LHP NC through combination with naturally occurring materials are mostly limited to less than 1 %,[103,159,160] chiral metasurfaces enable almost selective light-matter interactions as a function of CP upon careful design.[161] As such, a modulation of LHP properties through chiral metasurfaces seems promising, as explored in combination with bulk LHP films.[32,162] Yet, a modulation also of LHP NCs in terms of circular dichroism would be intriguing in view of their favorable optical properties and increased flexibility in device fabrication compared to the LHP bulk counterpart. I will provide an example of such a modulation in Chapter 5.

3

Materials and Experimental Methods

The findings presented in this thesis rely on suitable materials and analytical methods. This chapter is thus devoted to introduce the employed experimental techniques in detail. Materials with nanoscale dimensions, on which my investigations are based, can generally be obtained by so called bottom-up and top-down procedures. While bottom-up approaches arrange small units in a defined way, top-down methods rely on reshaping a macroscopic building block.[163] The first process was found to be suitable to obtain the self-synthesized $CsPbBr_3$ QDs of 5-13 nm diameter and is described in Section 3.1. Asymmetrically shaped metasurfaces with structural units of a few hundred nanometers were made by a top-down process introduced in Section 3.2. Subsequent imaging of these nanoscale structures requires microscopic techniques described in Section 3.3. Finally, the aim of my thesis – observing manipulations in the luminescence of $CsPbBr_3$ QDs – is realized by a variety of optical techniques, which are discussed in detail in Section 3.4.

3.1 How to synthesize Quantum Dots of a Defined Size

A close analysis of optical transitions in QDs with prevalent confinement effects demands samples with precisely defined size and shape. Although LHP NCs can be produced by top-down techniques such as exfoliation[57] or milling,[164] these syntheses are not strongly size selective, and require extensive post-synthetic separation procedures to obtain monodisperse samples.[57] Thus, bottom-up methods employing atomic building blocks in solution-based processes became popular which – given the right conditions – allow both, size and shape control.[27] This is important since each of my studies, the microscopic adsorption process discussed in Chapter 4 and the substrate induced excitation control analyzed in Chapter 5, has different demands. I have used two synthetic procedures, a ligand controlled growth and a hot-injection synthesis, respectively, to produce QDs with specific properties. Both are based on the same concept which I first explain before giving details of the exact implementation for each procedure.

Nucleation and Growth: The LaMer Diagram

The basic concept of forming nanocrystalline material in solution is depicted in Figure 3.1a. Two main phases can be distinguished: nucleation and growth. In the nucleation phase, nuclei form from monomers A and B, which contain the atoms inherent to the target material AB. This is followed by a growth phase during which the nuclei increase in size by consumption of more monomers.[165–167] Monomers are formed from precursors, which for LHP QDs are metal salts, such as $PbBr_2$ or Cs_2CO_3.[61,62] They are solubilized as complexes assisted by well-chosen

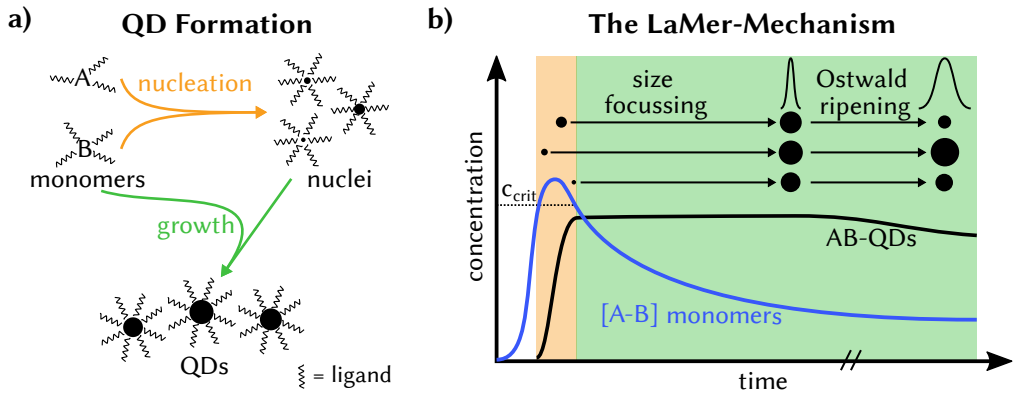

Figure 3.1: The Concept of Quantum Dot Formation in Solution. (a) QDs are formed by nucleation and growth from monomers A and B. Both, monomers and QDs, are stabilized in solution via ligands. **(b)** The LaMer-Mechanism of nucleation and growth. Precursors react to form monomer units [A-B] of the target material, whose fast increase in concentration causes a burst of nucleation. The subsequent growth phase is characterized by size focusing and Ostwald ripening, during which existing nuclei grow at a speed depending on the monomer concentration.

ligands. The ligand's binding strength is balanced such that the metal salts are stabilized in solution, but are made available by a fast decomposition of the complex during nucleation and growth.[166] Often, these ligands have a dual purpose and additionally serve as surfactants at the organic-inorganic interface of the growing nucleus.[168]
To generate a monodisperse sample while accounting for nuclei growing approximately at the same speed, all nuclei need to start growing at the same point in time.[167,169] Thus, a separation of nucleation and growth is compulsory. One option is a spatial separation, i.e. formation of nuclei in one vessel followed by their injection in the reaction solution for a so-called seeded growth.[170] This enables material combinations such as core-shell structures, provided that the energy barrier of formation is small enough to allow a growth.[171,172] However, it requires a preliminary synthesis of the nuclei, then called seeds. Alternatively, both nucleation and growth can happen in the same vessel but be temporarily separated with ideally a fixed point in time when all nuclei form. This is feasible via a kinetic control introduced by LaMer and Dinegar.[173] The different phases of this mechanism are shown in a diagram named in their honor (see Figure 3.1b) by means of the time dependent concentration for nuclei and soluble joint monomer unit [A-B] of the target material.
Firstly, the barrier for nucleation needs to be overcome. This can be described based on the Gibbs free energy ΔG_n to form a nucleus composed of n joint monomers [A-B]:[174]

$$\Delta G_n = \psi_n - \mathrm{k_B} T \ln(S)\, n \overset{!}{<} 0 \tag{3.1}$$

It is a balance between the surface energy of the nucleus, ψ_n, and the stabilization gained by the bulk formation. While the former increases with decreasing nucleus radius, the latter strongly depends on the supersaturation S and thus concentration of free joint monomer [A-B], with T denoting the temperature and $\mathrm{k_B}$ Boltzmann's constant. In the LaMer mechanism, such a supersaturation is provoked by a fast increase in concentration of the joint monomer [A-B].[174] The change can be initiated by various means, for example a sudden drop in temperature, solubility, or a mixture of precursors.[27,166] Once a critical concentration c_{crit} is surpassed, the growth rate at the respective conditions is sufficient to allow the formation of a stable nucleus, i.e. the energy gained through bulk formation exceeds the energy required to form a surface for a nucleus of small radius.[165,174] A burst of nucleation is the consequence, forming many bulk nuclei AB within a small time window. Subsequently, the nucleation needs to be stopped. This is provided by the decrease in concentration of monomer units [A-B] due to nucleation[166] but may be aided by a temperature drop.[167]
The nuclei, stabilized as a colloidal dispersion in solution with the help of surfactants, subsequently grow when monomers diffuse to their surface. Within this growth phase, size-focusing and Ostwald ripening occur.[165,175] These two competing processes cause a narrowing and broadening of the size distribution, respectively, which can be understood in the realm of

Equation 3.1. While the concentration of monomers is still large, smaller particles grow faster owing to the reduced amount of material needed to build a new layer. This is the size-focusing regime. At lower monomer concentrations and thus lower growth rate, however, higher surface energies of small particles causes large particles to grow on their expense, known as Ostwald ripening.[166,167] Thus, reactions need to be stopped at a "sweet spot" to achieve maximal monodisperse samples.

Hot-Injection and Ligand Controlled Growth

Two implementations of the LaMer mechanism, the hot-injection (HI) and the ligand controlled growth (LCG), were applied to synthesize $CsPbBr_3$ QDs (see Appendix for detailed protocols). Both are governed by the same synthetic steps, shown in Figure 3.2 together with the respective conditions for each method. The syntheses are based on a sudden injection of a prior prepared cesium monomer to a lead bromide monomer which initiates a burst nucleation. After a subsequent growth phase, purification steps serve to isolate the as-synthesized QDs. The hot-injection (HI) method, named for its operation at elevated temperatures during the injection step, has thus far dominated the synthesis of semiconductor QDs.[27] Introduced for

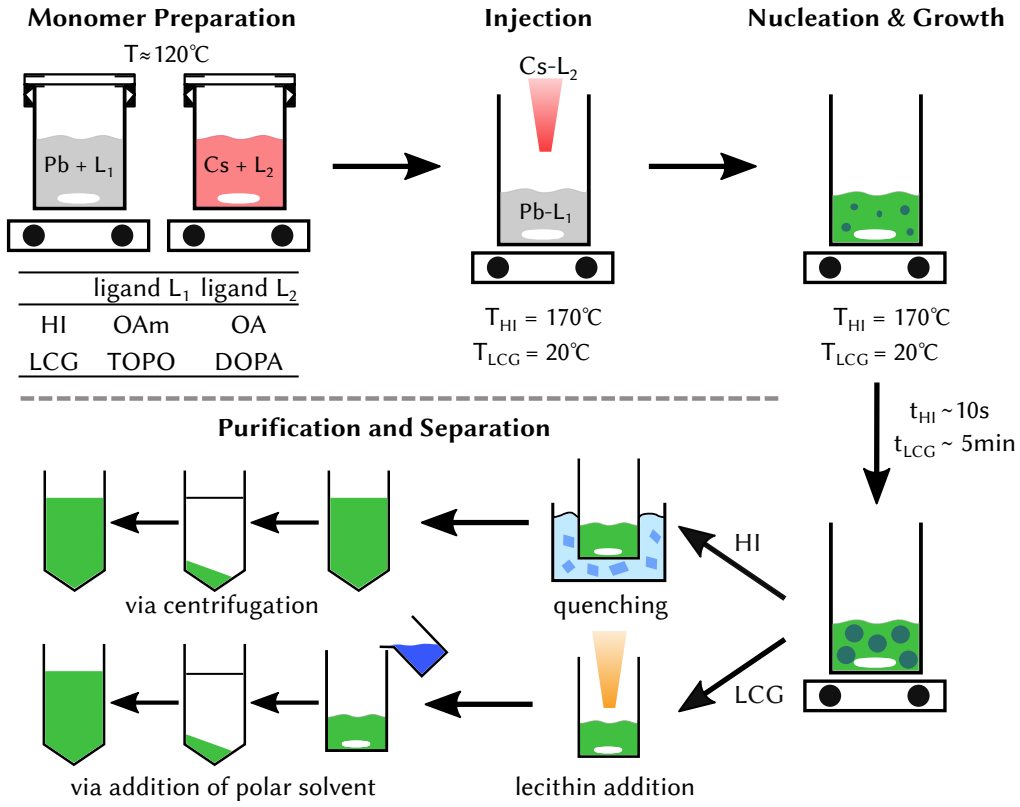

Figure 3.2: Synthesis of QDs with a Defined Size. The hot-injection (HI) and ligand controlled growth (LCG) method to achieve nearly mono-disperse QDs according to the LaMer-mechanism are governed by the same steps but rely on a different ligand system, synthesis temperature T and reaction time t.

CdSe QDs by Murray et al.[16] in the 90's, it has been adapted by Protesecu et al.[61] to yield cubic, inorganic LHP QDs. Although high-quality particles are predominantly made at inert gas atmosphere to prevent oxidation at elevated temperatures,[27] slight adjustments allow to refrain from such time-demanding inter-gas conditions.[176,177] Monomers are formed at elevated temperatures in octadecene (ODE) as a high boiling solvent by complexation of $PbBr_2$ and Cs_2CO_3 metal salts with long-chain amines, namely oleyl amine (OAm) and oleic acid (OA).[61] Both additionally serve as surfactants of the nuclei which are formed instantaneously upon injection of an aliquot of the as-prepared Cs-oleate to the $PbBr_2$ solution kept at elevated temperature.
In the HI-method, the size of the QDs is controlled by this reaction temperature. An increase allows to obtain larger QDs owing to weakening of the precursor complexes and faster diffusion.[167] Nucleation and growth happen instantaneously in this process with an overall reaction time of only a few seconds.[27] Thus, it is crucial to assure a quick injection and fast homogenization of the mixture by vigorous stirring while minimizing temperature variations. After the short reaction time, the growth is slowed by initiating a sudden temperature drop. Finally, the QDs need to be separated from unreacted precursors and excess ligands. For the HI-method, this is simply achieved by destabilizing the colloidal dispersion in a centrifugation step at high speed. The QDs precipitate, can thus be separated from the supernatant and freshly dispersed. Subsequent centrifugations varying the speed then allow to post-synthetically sharpen the particle size distribution and remove small or large particles from the solution, respectively.[57,166] Correctly speaking, the product is not a solution but a colloidal suspension, defined as a heterogeneous mixture of solid particles of small dimension within a continuous liquid medium.[178] For simplicity and following common practice, I further on refer to the QD colloidal suspension as the QD solution.

Although fairly monodisperse QDs can be obtained via the HI method, a precise control of the growth process and its parameters is impossible owing to the short reaction time. This results in varying sample quality and larger particle size distributions.[179] Additionally, the temperature range used to vary the size is limited by the solubility of the precursors, such that specifically small particles cannot be obtained easily.[61] Very recently, a synthetic procedure has been introduced which enables a better control and a separation of nucleation and growth processes.[62] This process is referred to as the ligand controlled growth (LCG) and is shown in Figure 3.2, too. OAm and OA are replaced by alkyl phosphine oxides,[62] which have proven their value already in conventional II-VI semiconductor synthesis.[16,166] The rationale behind this replacement is that long chain amines and acids, such as OAm and OA, strongly bind to the $CsPbBr_3$ QD surface while the metal salt complexes are rather weak.[176] Phospho-ligands on the contrary, such as trioctylphosphineoxide (TOPO) and diisooctylphosphonic acid (DOPA) employed here, are characterized by a rather weak binding strength to $CsPbBr_3$ and an in-

creased interaction with metal salts.[62] Thus, stable complexes are formed which significantly alters the growth dynamics. Similar to the HI-method, supersaturation is achieved by a quick injection of a Cs-DOPA to the reaction solution containing a $PbBr_2$-TOPO monomer. However, the reaction itself is conducted at room temperature and slow on the timescale of minutes.[62] Instead of temperature variation, control of the amount of TOPO in the reaction solution allows to alter the QD's size. Larger amounts of TOPO reduce the available $PbBr_2$ concentration. In consequence, less nuclei are created during the nucleation phase and overall larger particles are obtained.
The beauty of the LCG approach is manifold: most obviously, the slower reaction without amine ligands, known to participate in Ostwald ripening,[176] allows to achieve extremely monodisperse samples.[62] Secondly, nucleation and growth can potentially be completely separated which should allow for core-shell structures. Furthermore, the slow reaction time allows to monitor and thus analyze the process by in-situ spectroscopy. Finally, the choice of ligands with a weak affinity to the QD's surface enables an easy exchange and thus adjustment to a specific application's need. Here, lecithin solution was used to stabilize the QDs. This bulky, bidentate ligand with its zwitterionic head group strongly binds to the QD's surface[180] and thus allows to treat as-capped QDs with polar solvents usually known to destroy lead halide perovskites.[180,181] Thus, instead of being limited to the centrifugal force, a destabilization of the QD dispersion for purification is feasible via addition of polar solvents and collecting the precipitated QDs by a mild centrifugation. This is additionally advantageous as it allows several washing steps to remove any excess ligands.

QDs synthesized by the HI and LCG methods are shown in Figure 3.3. A difference in shape is apparent. While cubic particles are obtained via the HI-method, the LCG method yields spherically shaped QDs. This is a result of the different ligand systems, amines versus phosphine oxides, that control the surface chemistry during the QD growth. The ligands dynamically attach and detach from the QD surface driven by the facet-dependent binding strength. This can readily be exploited to stir the growth process. A reduced coverage causes a faster growth and thus induces the formation of different shapes.[166,182] This has been

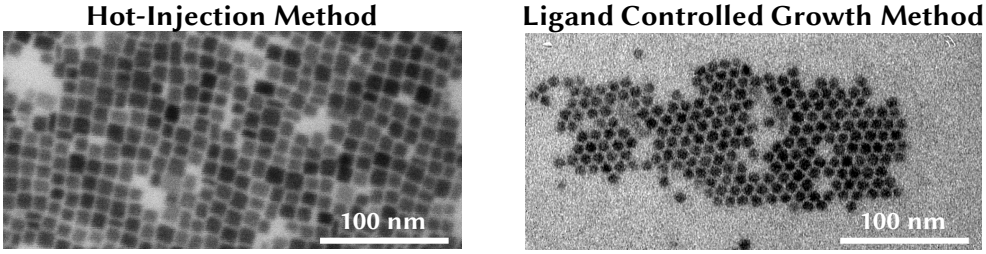

Figure 3.3: Ligand Impact on the QD Shape. The influence of an alteration in surfactants is shown by the cubic and spherical shape of QDs synthesized via the HI and LCG method, respectively.

extensively used for metallic[168] and conventional semiconductor NCs[183,184] but has also been demonstrated for perovskite NCs upon variation of type and amount of the amine and acid ligands.[185,186] Amine ligands employed in the HI-method strongly bind to the 110-facet, which thus induces the growth of cubic crystals.[187,188] TOPO, on the other hand, has a very weak affinity for all crystal facets. Together with the slow growth rate of the LCG method that leads to a thermodynamic control, this favors the formation of more round shaped crystals.[166]

3.2 Producing a Nano-Structured Surface

Generally, patterns of nanoscale scatterers may be obtained by top-down approaches, such as lithography or imprinting, and bottom-up methods, i.e. self-assembly.[163] For complex patterns on the nanoscale, nanolithographic techniques are advantageous given their high flexibility.[189] A focused beam deflected across a material surface by means of a scanning microscope setup is used to subscribe a defined pattern into a material that is sensitive to beam exposure. As the resolution is limited by the beam's dimension and thus depends on the wavelength (see also Section 3.3), especially electron beam (e-beam) lithography has been established to obtain structures of a few nanometer resolution.[189] Multiple steps characterize an e-beam lithography process. These steps are shown in Figure 3.4. They have been conducted by D. De Gregorio and F. Wendisch to produce the herein applied metasurfaces, and are thus only briefly discussed.

In a first step, the material itself that ought to be shaped, here a 120 nm amorphous silicon (a-Si) layer, is deposited on a glass substrate of $1 \times 1\,\mathrm{cm}^2$ by means of plasma-enhanced chemical vapor deposition (CVD). Next, the substrate is prepared for e-beam lithography by spin-coating a polymer layer as the resist, here polymethylmetacrylate (PMMA), on top (hardened at 170 °C). This is followed by deposition of a thin conductive polymer layer (Espacer) as an electron dissipating material, preventing charging during the subsequent lithography process. The as-prepared sample is selectively exposed to the focused electron beam (30 kV, 20 µm aperture, 10 mm working distance) in a designed pattern. In our case, an area of $40{\times}40\,\mu\mathrm{m}^2$ has

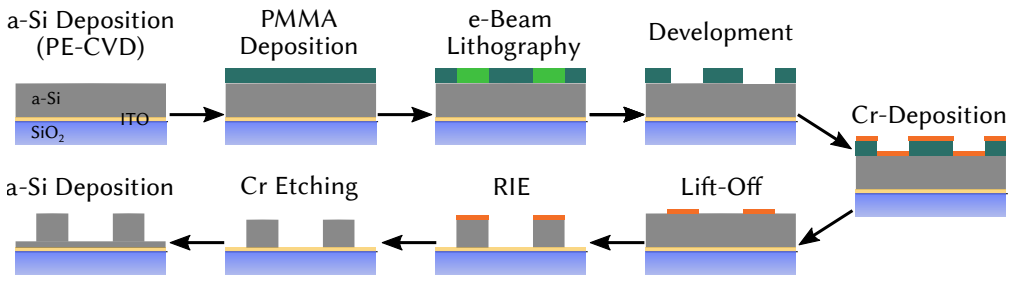

Figure 3.4: E-Beam Lithography Process. The process includes several deposition steps prior to the e-beam lithography itself, which is followed by development, lift-off and etching steps to transfer the desired pattern to the material of interest, here amorphous silicon.

been covered by an array of 40 x 40 metaatoms. For a positive resist, this exposure increases the solubility by scission of polymer chains. Material exposed to the beam is removed by chemical treatment (with methylisobutylketone(MIBK)) and a negative of the pattern remains. The next two steps serve to transfer the pattern as a chromium layer to the a-Si surface. First, a 30 nm chromium layer is deposited. Subsequently, the remaining polymer is removed (microposit remover 1165) in the so-called lift-off process. Afterwards, reactive ion-etching (RIE) with a Ar/Cl_2 mixture shapes the a-Si in the desired way by removing material not protected by chromium. The latter is then removed with a commercial etchant. At the very end, an additional 13 nm a-Si layer is deposited by CVD.

3.3 Imaging QDs and their Arrangement

As a first measure in characterizing the QDs and metaatoms, their size, shape, and arrangement towards each other need to be determined. Generally, microscopy techniques serve to obtain a magnified image of small objects. According to Abbe's famous formula,[190] the minimal distance d at which two spots can be distinguished is limited by the wavelength λ of illumination and the numerical aperture NA of the microscope's imaging objective:

$$d = \frac{\lambda}{2NA} \tag{3.2}$$

Here, $NA = n \cdot \sin(\alpha)$ is defined by the opening angle 2α of the focal cone and the refractive index n. For a system in air or vacuum, NA is limited to unity. Thus, visible light with $\lambda >$ 400 nm clearly does not provide a sufficient resolution to image the nanometer sized objects of interest, given that distances as small as twice a ligand's dimension at the QD's surface, i.e. approximately 4 nm, need to be distinguished. Much shorter wavelengths can however be achieved with accelerated electrons, as their De-Broglie wavelength scales inversely with the square root of their kinetic energy E and the electron's mass m_e according to[191]

$$\lambda_e = \frac{h}{\sqrt{2m_e E}} \tag{3.3}$$

with h being Planck's constant. This requires an electron source, their acceleration and an imaging system, i.e. lenses capable of focusing an electron beam, which can be constructed by inhomogeneous magnetic and electric fields.

Transmission Electron Microscopy

A transmission electron microscope (TEM), first introduced by E. Ruska based on the principle of a transmission light microscope using an electron beam and electromagnetic lenses,[192,193] is shown in Figure 3.5a. Electrons emitted from a field emission gun are accelerated along

a vertical electrical field and focused by means of a condenser system to homogeneously irradiate a sample spot. Within the specimen, electrons are absorbed, scattered and diffracted depending on the specific material properties, i.e. its thickness, elemental composition, and crystallinity.[193] The transmitted electrons are collected and imaged with the help of an objective and projection system on a scintillator, converting them to photons which in turn are detected with a charge coupled device (CCD) camera. Naturally, the complete setup needs to be operated at high vacuum conditions to avoid any unwanted matter-electron interactions.[193,194] The intensity contrast at the detector is representative for the interaction happening at the specimen. This can be exploited to detect the size and shape of QDs dropcasted from diluted solutions to yield a thin layer on a carbon coated copper TEM grid (Science Services GmbH, FCF200-CU-50). Images presented in this thesis have been taken by Q. Akkerman at a *Jeol JEM-1011* operating at an acceleration voltage of 80 kV. This provides an overall resolution of approximately 0.4 nm, allowing to visualize the dimensions d of QDs as exemplary shown in an acquired image in Figure 3.5a. Notably, modern high-resolution TEMs even enable the detection of single atoms.[193]

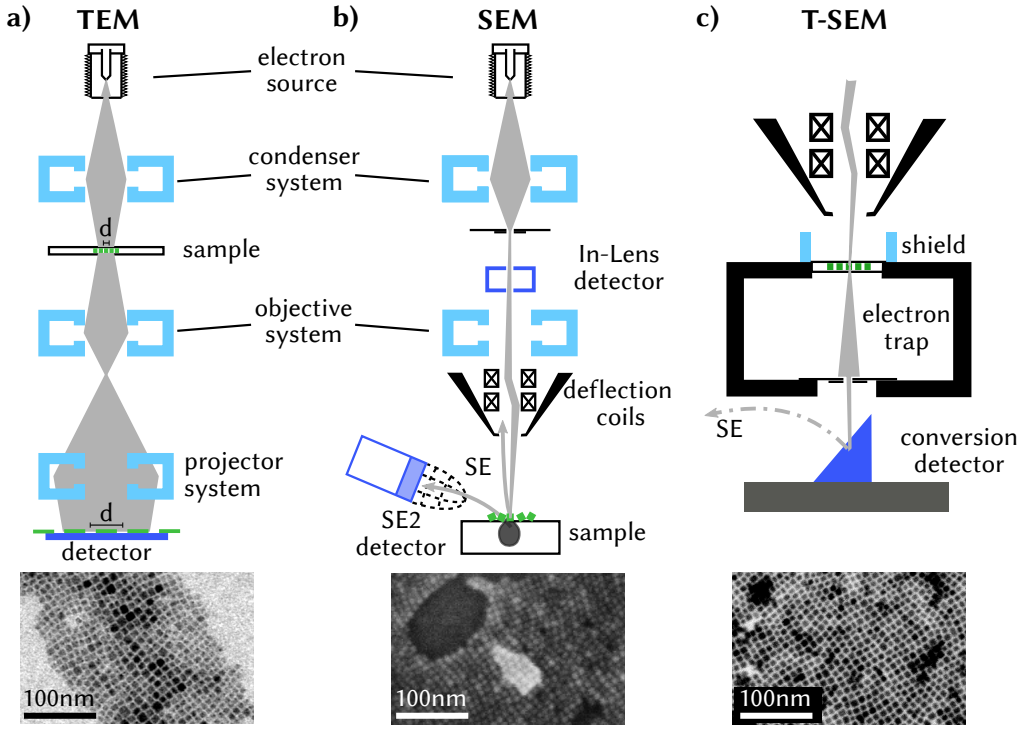

Figure 3.5: Illustration of Electron Microscopy Techniques. (a) A transmission electron microscope (TEM) enables the magnification of nm-thin samples to determine i.e. the size (d) and shape of QDs. Its construction resembles a classical transmission light microscope. **(b)** Arrangements of QDs on conductive substrates can be probed with a scanning electron microscope (SEM), relying on the point-to-point detection of secondary electron (SE). **(c)** T-SEM allows to obtain TEM-images with a standard SEM by means of a special holder. A representative image of 8 nm cubic QDs obtained with each technique is shown below the respective setup.

Scanning Electron Microscopy

Although a TEM serves well to image QDs, the investigation is restricted to samples of less than 100 nm thickness as transmittivity needs to be assured.[193] Additionally, only a small portion of the sample is placed at the focus, making a motion of the sample necessary to image different regions. Due to their thickness, metasurfaces and the arrangement of QDs deposited on a substrate can therefore not be imaged by a TEM. Instead, such thick conductive substrates can be investigated using a scanning electron microscope (SEM). A sketch of the SEM (*Gemini Ultra Plus field emission SEM*, Zeiss) and a typical image obtained for the QDs arrangement on a silicon substrate are shown in Figure 3.5b.
The system is derived from a TEM, however, the three-dimensional substrate whose surface shall be probed is placed after the objective lens and a projection system is omitted. Instead, various signals resulting from the matter-electron interaction at the focal spot are detected. Deflection coils allow to scan the electron beam across the sample, thus enabling large area imaging via a point-to-point collection of information. High energetic back-scattered electrons and material-selective x-rays emitted upon relaxation of ionized atoms can be used to obtain a material contrast.[194] However, to image QD arrangements all composed of the same material, a detection of secondary electrons (SEs) created through inelastic scattering at either the built-in In-Lens or Everhart Thronley SE2-detector is more practical. Owing to the SE's low energy of less than 10 meV once emerged at the material's surface, the detected amount per sample spot depends on their shielding towards the detector and is thus characteristic for the surface roughness.[194] Compared to a TEM, much lower acceleration voltages, here of only 3 kV, are applied as charging effects shall be avoided. Together with the extended interaction volume of the electron beam in the three-dimensional sample, the SEM's resolution is thus overall limited to more than 1 nm.[194]

T-SEM - the Combination of Both Worlds

The large area imaging enabled by the scanning method is advantageous to ensure sample homogeneity during size and morphology characterization. Thus, a specialized sample holder provided by Zeiss has been used to operate the SEM in transmission mode (see Figure 3.5c) at an increased acceleration voltage of 30 kV. This T-SEM single unit is composed of a substrate holder for standard TEM grids and a conversion detector. The latter serves to transform transmitted to secondary electrons, which are subsequently detected with the built-in SE2-detector. An extra aperture (electron trap) assures that only non-deflected electrons are detected while the shield prevents SE-electrons created in the substrate to reach the SE2-detector. Similar to a TEM image, the intensity at a given spot depends on the number of transmitted electrons. While profiting from the point-wise scanning of a large area, a higher contrast is achieved by reducing the multiple scattering events intrinsic to the three-

dimensional substrate of a standard SEM operation.[192] The comparison of images obtained by T-SEM and TEM in Figure 3.5 demonstrates that an almost identical resolution can be achieved for the devices applied here. Thus, given a direct accessibility of the SEM facility, T-SEM has been applied within this thesis as an alternative to standard TEM measurements.

3.4 Optical Analysis of QDs and their Arrangement

Optical spectroscopy is most generally speaking an energy dispersive detection of either absorbed or emitted light.[40,139] As such, it provides a detailed insight on the optical transitions between electronic states within QDs that have been described in Subsection 2.1.3. The specific techniques applied within this thesis for investigating QDs and their arrangements are subsequently introduced in more detail. Subsection 3.4.1 focuses on the steady-state spectroscopy of QDs in solution. In Subsection 3.4.2, a setup that allows for a spatially selective observation of QD arrangements is introduced. Finally, time-resolved techniques enabling to monitor dynamics of the excited state are discussed in Subsection 3.4.3.

3.4.1 Steady-State Spectroscopy for Characterizing QDs

Valuable information on the fundamental electronic structure but also about ensemble characteristics of QDs is gained by probing their time-integrated interaction with light, i.e. based on intensity measurements.[78] QD solutions as obtained during their synthesis can be directly investigated. The basic principle of such steady-state absorption and PL measurements is shown in Figure 3.6.

The amount of absorbed photons is measured indirectly by a reduction in intensity of light rays from a white light source when they traverse the QD suspension. The transmitted light beam is guided through a spectrograph to spatially spread light rays of different wavelength λ with the help of a grating. This allows for an energy dispersive detection of the transmitted light intensity $I_\mathrm{t}(\lambda)$ at a photodetector either using an array detector or step wise scanning the spectrum.[40] The wavelength dependence of I_t is subsequently implied but not explicitly written. Besides absorption, generally scattering and reflection that change the light wave's direction[195] contribute to such a transmission signal. These effects are usually considered to be negligible for colloidal well dispersed QDs of sizes much smaller than the light's wavelength. Background effects from the glass vial are on the other hand taken into account with a reference measurement, that allows to obtain a corrected impinging light intensity I_0'. Overall, the as-corrected intensity ratio of light exiting and entering the sample, the transmission T, is governed by the absorption A and can be expressed as:

$$T = \frac{I_\mathrm{t}}{I_0'} = \mathrm{e}^{-\alpha d}, \tag{3.4}$$

as evident from a comparison with Equation 2.9. It exponentially decays with the sample's thickness d and the absorption coefficient α that relies on the material dependent properties such as on transitions between excited states in the material.[195]
Photoluminescence measurements are performed in a very similar fashion, however, a few adjustments are necessary to allow for the detection of light emitted from the material subsequent to an excitation process. Most importantly, the geometry between the excitation light beam and the detection light path is altered to an angled position, which is often 90°. This prevents the excitation light beam and most of its stray light from hitting the detector unit.[78] The emitted light however, subject to spherically radiation for QDs in non-viscous solutions,[78] can be collected with a lens and its energy can be dispersively detected using a spectrograph. Usually, the sample is excited with light of a specific wavelength λ_{ex} for a selective excitation.

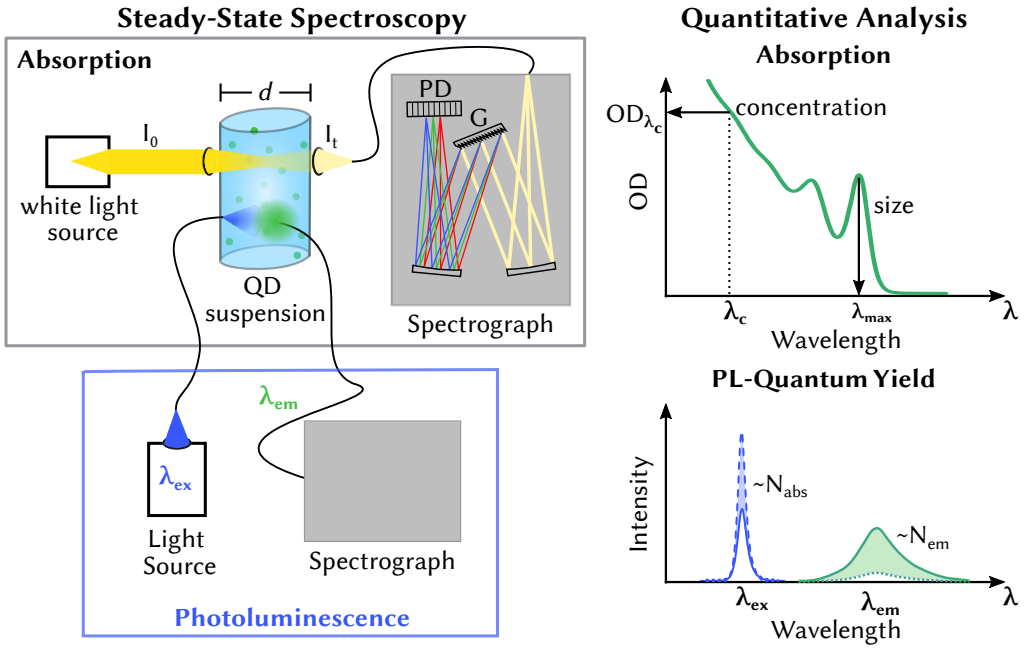

Figure 3.6: Steady-state Spectroscopy and the Quantitative Spectral Analysis. A QD suspension of thickness d is probed for its absorbance in a directional arrangement, detecting the reduction in the white light's intensity from I_0 to I_t upon transmission with a spectrograph composed of a grating G and an array detector PD. The photoluminescence setup is characterized by an angled arrangement – here based on fiber optics – to selectively detect the emitted light (λ_{em}) with a similar spectrograph following an excitation. A typical QD's absorption spectrum is shown on the right. The QD's size can be extracted from the excitonic peak position while the absorbance outside of the confinement regime is proportional to the solutions' concentration. A quantitative analysis of the PL is feasible by an integration of spectra acquired for a sample placed within an integration sphere, yielding the ratio of absorbed (N_{abs}) to emitted (N_{em}) photons.

What an Excitonic Absorption Reveals about Size and Concentration of QDs

Absorption spectra have been acquired with a *Cary 60 UV-Vis* spectrophotometer (Agilent Technologies). A typical absorption spectrum of a QD solution is shown in Figure 3.6. Commonly, the absorption is expressed in terms of the negative decadic logarithm of the transmission, the so called absorbance *OD*:[195]

$$OD = \lg\left(\frac{1}{T}\right) = \frac{\alpha}{\ln 10} d \tag{3.5}$$

Clearly, *OD* depends on the energy of the interacting photon. This is related to the material dependent absorption coefficient α. If the material is a QD suspension, α is inherent to the exact composition of the solution i.e. solvent, type of the colloidal material and particle density.[196] A quantitative analysis of the absorbance makes use of exactly this dependence. For homogeneous and diluted solutions, it is valid to assume a linear relation between the solutions' absorption coefficient and the volume fraction f occupied by the QDs, $\alpha = \mu_\mathrm{i} f$ with a material and solvent dependent intrinsic absorption coefficient μ_i.[196] This is essentially the Lambert-Beer law, linearly relating the absorbance *OD* with the material's concentration c and extinction coefficient ϵ:

$$OD = \frac{\alpha}{\ln 10} d = \frac{\mu_\mathrm{i} f}{\ln 10} d = \frac{\mu_\mathrm{i}}{\ln 10} V_\mathrm{u} N_\mathrm{A} c d =: \epsilon c d \tag{3.6}$$

The penultimate equality considers that the volume fraction f relates to the material's concentration c by the volumetric size of one stochiometric unit V_u. Thus, analyzing the quantity of the absorbance reveals the concentration of the QD material and – for a known particle size – the concentration of QDs, provided that the material's μ_i is known for the specific wavelength and solvent. For $CsPbBr_3$, Maes et al.[110] determined μ_i in hexane and toluene at 335 nm and 400 nm. The corresponding values are given in Table 3.1 and have been used to calculate the concentration of $CsPbBr_3$ within the QD solutions.

Table 3.1: Intrinsic Absorption Coefficients of $CsPbBr_3$ NCs according to Maes et al.[110]

	hexane	toluene
$\mu_{i,335\,\mathrm{nm}}\,(\mathrm{cm}^{-1})$	$(15.9 \pm 0.5)10^4$	$(17.9 \pm 0.6)10^4$
$\mu_{i,400\,\mathrm{nm}}\,(\mathrm{cm}^{-1})$	$(7.7 \pm 0.8)10^4$	$(8.7 \pm 0.9)10^4$

The apparent energy dependence of μ_i can be utilized to determine the composition and size of a confined system. This is due to the fact that it represents the probability to undergo a certain electronic transition (see Subsection 2.3.1). For confined materials such as a QD, these electronic states are discrete excitonic states characteristic for its size and composition (see Subsection 2.1.1). In the absorption spectrum, the discrete transition lines are broadened to Gaussian shaped peaks mainly owing to inhomogeneous broadening which

increasingly overlap at larger excitation energies.[67,197] The energetically lowest transitions are still well separated for sufficiently monodisperse samples. Akkerman et al.[62] exploited this to determine the diameter d of spheroidal $CsPbBr_3$ QDs using an empirical relation for the first excitonic peak's position E_{X1}:

$$d/\mathrm{nm} = 2.42342 \cdot (E_{X1}/\mathrm{eV} - 2.402)^{-0.45388} \tag{3.7}$$

A good agreement with the theoretical square-root dependence of weakly confined systems is evident. Equation 3.7 has been applied to determine the sizes of spheroidal QDs in addition to analyses with a TEM.

Radiation Efficiency: The Photoluminescence Quantum Yield

While the absorbance reveals composition, size and concentration in solution of QDs, a closer analysis of the PL is insightful for understanding the relaxation behavior of a material. In the commercial PL spectrometer applied within this thesis (*Fluorlog FL 3-22*, Horiba), a white light xenon lamp combined with a monochromator serves as the monochromatic excitation source. This enables a modulation of the excitation wavelength within a broad spectral range from 240 nm to 600 nm[198] while monitoring the emission intensity at a fixed λ_{em}. The result of such a measurement is a photoluminescence excitation (PLE) spectrum. It is governed by the efficiency to absorb a photon of certain energy – i.e. the absorbance – combined with the efficiency to relax and radiatively emit a photon, the so called PLQY. This PLQY is defined as the ratio between the number of absorbed and emitted photons and is very insightful for identifying non-radiative relaxation processes (see Subsection 2.1.3). A comparison of PLE and absorption thus already allows to qualitatively analyze the PLQY evolution with the excitation wavelength. A quantitative determination of PLQY(λ_{ex}) is however more challenging, as it requires a precise knowledge of the emitted and absorbed photon numbers instead of a mere intensity measurement.

Two techniques have been established thus far, the comparative Parker-Rees method relying on reference fluorophores[199,200] and the more flexible absolute method. The latter was used within this thesis and is now described in detail. The absolute determination is feasible with the help of an integration sphere (*K-Sphere Petite*, Horiba), a hollow sphere commonly equipped with a highly diffuse reflective coating[201] placed above the sample. The entrance and exit port are designed such that light only exits the sphere after being multiply reflected. Thus, anisotropic effects can be neglected. The intensity is equivalent to the number of emitted photons when detection takes place within the wavelength range of emission. Upon detection at the excitation range, it is proportional to the transmitted and scattered photons.[202] One measurement at each wavelength range for both, the sample and a blank solution, enables to

determine the PLQY via the following relation:

$$QY = \frac{N_{\mathrm{em}}}{N_{\mathrm{abs}}} = \frac{\int k(\lambda_{\mathrm{em}}) \left[I_{\mathrm{s}}(\lambda_{\mathrm{em}}) - I_{\mathrm{b}}(\lambda_{\mathrm{em}}) \right] \mathrm{d}\lambda_{\mathrm{em}}}{\int k(\lambda_{\mathrm{ex}}) \left[I_{\mathrm{b}}(\lambda_{\mathrm{ex}}) - I_{\mathrm{s}}(\lambda_{\mathrm{ex}}) \right] \mathrm{d}\lambda_{\mathrm{ex}}}, \tag{3.8}$$

Here, $I_{\mathrm{s/b}}(\lambda_{\mathrm{em}})$ and $I_{\mathrm{s/b}}(\lambda_{\mathrm{ex}})$ are the intensities of emitted and transmitted light for a sample and a blank solution, respectively. $k(\lambda_{\mathrm{em}}/\lambda_{\mathrm{ex}})$ is a proportionality constant determined via calibration. The integrated differences are shown in Figure 3.6 and marked in blue (green) for the number of absorbed (emitted) photons. Although this seems straightforward, it shall be noted that a reliable PLQY measurement is indeed challenging. Apart from an accurate calibration, dilution related effects such as re-absorption can influence the result significantly which overall limits the accuracy to ±5 %.[203]

In-Situ Spectroscopy: A Glimpse in the Reaction Vessel

The section thus far has shown how absorption and emission spectroscopy reveal valuable information on a material's composition, its size and radiation ability. As such, obtaining these spectral information right at the moment of growth or modification of a nanoscale material would be a great benefit. It allows to disentangle effects of single synthetic parameters stirring a reaction's fate and thereby provide the necessary clues to reconstruct e.g. a synthesis mechanism. Such an in-situ monitoring requires a setup that can acquire spectra at a short timescale (sub-seconds) and thereby distinguish the different phases of particle formation described in Section 3.1. Thus, the commercial spectrometers operating with a precise single photodetector and step wise acquisition need to be replaced by a simplified spectrometer setup offering a fast response time.
A setup fulfilling this prerequisite has been reported by Akkerman et al.[62] as sketched in Figure 3.6 and has been used for in-situ studies within this thesis. Based on compact CCD spectrometers (Thorlabs, *CCS200/M*), a spectrum is projected on an array detector instead of a step wise scanning allowing for a sampling of up to 200 spectra per second. Absorption and PL spectra are measured simultaneously within the well-mixed solution at different heights. A white-light deuterium-tungsten light source (Ocean Optics, *DH-2000-BAL-TTL-24V*) is used in the absorption line. For the PL measurement the sample is illuminated at a 350 nm (*Convoy 53 UV flashlight*) in a front face configuration using a bifurcated optical fiber that serves for detection and excitation. As a downside of the fast scanning, the signal to noise ratio is limited to less than 200:1. However, for an absorbance exceeding $OD = 0.1$ at the first excitonic position this is still sufficient to distinguish the signal shape and thus analyze modifications of the material in-situ.

3.4.2 The µ-PL-Setup: A Versatile Tool for Spatially Resolved Studies

One aspect of my thesis is the PL control of QD monolayers with a structured substrate, a metasurface. This requires a locally resolved observation of the PL to distinguish structured and unstructured substrate parts, feasible with a home-built setup sketched in Figure 3.7. Its construction is described in detail in the PhD thesis of Alexander Richter.[204] Thus, only main functionalities relevant for the current study and modifications taken to adjust the setup for the described task are mentioned here.

Overall, the setup is a fluorescence microscope which operates on the same basic principles as discussed in Section 3.3 for electron microscopy. A sample is illuminated perpendicularly with a laser beam and the emitted PL light is collected and subsequently imaged on a CCD camera (*PIXIS 400BR eXcelon*, Princeton Instruments). Using a simple mirror within the preceding spectrograph (*Acton SpectraPro SP-2300*), a real image and thus a spatially resolved intensity projection of the PL signal is achieved, whose resolution is limited to approximately 1 µm as a consequence of the operation with visible light. Alternatively, the PL spectrum can be imaged when a slit selects a small spot and the light is passed over a grating within the spectrograph.

To allow for the normal incidence of the excitation laser light, a dichroic mirror (DM) couples the laser beam into an objective (*40x, NA 0.55, SLCPlanFL*, Olympus) that serves to focus

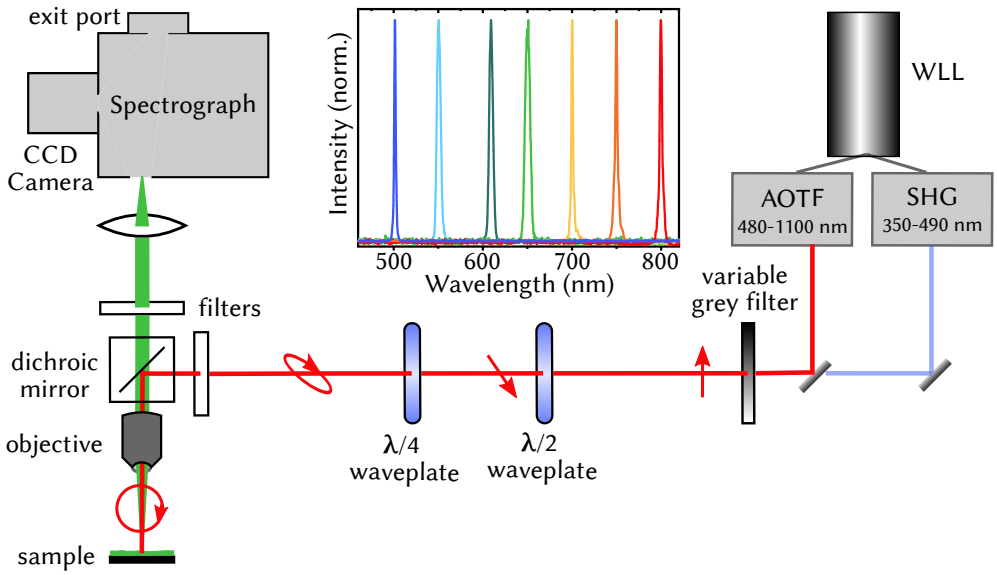

Figure 3.7: The µ-PL-Setup. The home-built fluorescence microscope couples a laser beam via a dichroic mirror into an objective, allowing for a localized excitation of a sample, while emitted light is collected and transmitted towards a spectrograph. PL light is imaged with a grating or mirror on a CCD camera for spectrally or locally resolved detection, respectively. Spectrally narrow excitation within a broad wavelength range (350-1100 nm) is achieved with a pulsed white light laser beam coupled to a wavelength selection system, while additional optics in the light's path allow its modulation in terms of intensity (gray filter) and polarization (waveplates).

the excitation light on the sample's surface. At the same time, it collects the PL light that is subsequently transmitted through the dichroic mirror. A long pass (LP) and a short pass (SP) filter in emission and excitation path aid to remove any reminiscent laser light for solely imaging the PL. This is crucial to enable an intensity analysis based on these images as described later on. The cutoff wavelength of the respective filters are usually chosen such that the dichroic separation wavelength lies in between. Linear PL signals have been acquired with the combination $SP_{492\,nm}$ - LP-$DM_{495\,nm}$ - $LP_{496\,nm}$, with the number being the respective cutoff wavelength. For PL detection upon below band gap excitation, a combination of $LP_{675\,nm}$ - SP-$DM_{556\,nm}$ - $SP_{600\,nm}$ has been used. With its 1 µm resolution, the setup is generally able to spatially distinguish PL light originating from spots on the metasurface and surrounding unstructured surface parts of a substrate that contains the 40×40 μm^2 metasurface at a defined location. The required local illumination is feasible given the excitation with a laser beam, that can be focused to a size of $5 - 10\,\mu m^2$ or $60 - 70\,\mu m^2$ for visible and UV light, respectively. Additionally, illumination with a torch instead of the laser allowed to easily locate the metasurface on a substrate of several millimeters edge length and place it at the center of the illumination cone. Finally, a piezo-stage (*P-545 PI nano™XYZ*, PI) capable of shifts as small as 1 nm,[205] enabled a fine adjustment of the substrates position with absolute sufficient precision.

Apart from its spatial resolution, the main advantage of this home-built setup is its large flexibility. A variable illumination source is necessary to realize the excitation dependent studies presented in this thesis. This is met by the pulsed super-continuum white light laser (*SuperK EXTREME EXR-20*, NKT Photonics, 0.12-78 MHz repetition rate with 30-90 ps pulse length). It can be coupled either with an acousto-optic modulator (*SuperK SELECT*, NKT Photonics) to select a suitable wavelength within the visible to near IR range (470 nm to 1100 nm) or with a UV selection box based on second harmonics generation (*SuperK EXTEND-UV*) for an irradiation at 330 nm to 480 nm. The latter has been used to investigate the linear PL response while the former was applied for multi-photon absorption studies. Importantly, the laser beam is spectrally narrow with its small full width at half maximum (FWHM) limited to 5 nm (470 nm - 1100 nm) and 10 nm (400 nm - 480 nm), respectively, enabling a precise excitation dependent interpretation of PL signals. Additionally, a second exit port at the spectrograph enables time-resolved PL studies discussed in detail in Subsection 3.4.3. Finally, unlike in closed-off commercial setups, an inclusion of additional optics is feasible. This has been exploited to vary not only the excitation wavelength but also its polarization state with the aim to quantitatively compare PL intensities upon various excitation conditions. Thus, a gray filter and two waveplates have been inserted in the excitation beam path. The purpose of these three parts is discussed in more detail.

Obtaining Control of the Light's Power and Polarization

Firstly, the gray filter regulates the laser power P_λ to precisely achieve the same number of photons N at the sample position, independent of the excitation wavelength λ:

$$P_\lambda = N \cdot E_\lambda \cdot \nu_{\text{rep}} = \frac{N \cdot hc \cdot \nu_{\text{rep}}}{\lambda}, \tag{3.9}$$

This is necessary for a comparative analysis of the excitation dependent emission intensity, with E_λ as a photon's energy and ν_{rep} the laser's repetition rate. The respective gray filter position has been determined as a function of the wavelength by placing a powermeter at the sample's position.
Secondly, the laser output, both in the visible and the UV range, is initially linearly polarized in a horizontal direction.[206,207] In order to alter its orientation and also helicity to address different polarization states (see Chapter 2), optical elements need to be added in the beam path. This is the task of the waveplates in Figure 3.7. Compared to reflective or absorptive polarizing optical elements that block light of unwanted polarization, waveplates use a uniaxial birefringent material to convert the polarization and thus do not attenuate the beam intensity.[208] The basic principle of a waveplate is sketched in Figure 3.8. In a birefringent material, the refractive index n differs for light polarized along crystallographically different axes. For a light wave (red) incident on a waveplate, one component polarized along the axis of higher refractive index, the so called "slow axis", propagates through the material at a lower

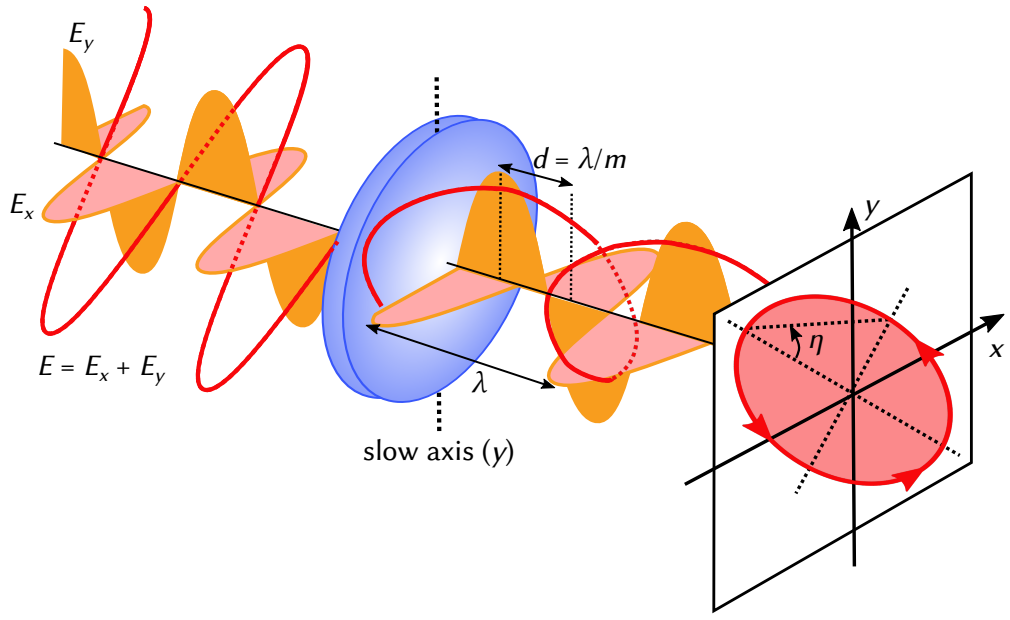

Figure 3.8: Principle of Light Modulation by a Waveplate. The light wave is depicted in red, while its components parallel and perpendicular to the "slow axis" of the waveplate are shown in orange and pink, respectively. Their path difference d causes an elliptical polarization of the originally linearly polarized wave with the electric field vector projected on the screen.

speed compared to its perpendicular counterpart.[‡] This so-called retardation induces a phase shift δ between these rays at the point of exit, linked to the refractive index difference Δn of the two distinguished axes and the light's vacuum wavelength λ by $\delta = 2\pi D\Delta n/\lambda$. It can be easily adjusted through the material's thickness D. The polarization state is modified such that the electric field vector now encompasses in general an elliptical trajectory. This can be visualized upon its projection on a screen as indicated with its ellipticity η (see also Subsection 2.3.3). Waveplates are categorized according to the retardation commonly expressed in terms of the path difference d in units of the wavelength, with m as an integer. Here, an achromatic $\frac{\lambda}{2}$ (450 - 800 nm, *AQWP05M-630*, Thorlabs) and $\frac{\lambda}{4}$ waveplate (325 - 1100 nm, *SAQWP05M-700*, Thorlabs) have been used. The former induces a phase shift of π, thereby rotating the plane of a linearly polarized light wave, while the latter causes a circularly polarized beam based on the phase shift of $\frac{\pi}{2}$ for linearly polarized at 45° to the "slow" axis. The term "achromatic" implies that the retardation does not vary with the wavelength, which can be achieved by combining different birefringent materials,[209] here MgF_2 and crystalline quartz.
With the above description of the waveplates, it should be possible to predict the polarization state at the sample's position (see Figure 3.7) based on the waveplate orientation and the laser beam polarization using the Jones-Matrix formalism.[139] However, things are complicated by guiding the light past a dichroic mirror prior to hitting the sample. Fresnel showed and explained that the reflection of a light's component with a parallel and perpendicularly orientation to the plane of incidence differ, and this additionally depends on the wavelength.[139,208] As a consequence, an initially well defined polarization state is modulated by the dichroic mirror. The waveplates' position thus need to be adjusted to yield elliptically polarized light which is subsequently transformed to an exactly circularly polarized light at the sample's location (see Figure 3.7). Although the overall polarization modification by the series of optical elements can theoretically be determined, too, it is prone to slight variations when elements are inserted or removed from the beam path in this multi-user setup. Thus, the waveplates' rotation has been calibrated for each wavelength and desired polarization state prior to conducting an experiment with the help of a polarization analyzer (*SK010PA*, Schäfter and Kirchhoff) placed at the sample's location. Note that an individual adjustment of both waveplates for each wavelength and polarization state is necessary.

Programmed Image Acquisition and Analysis

During the excitation dependent measurements presented in Chapter 5, series of images have been acquired upon a variation of the excitation power, wavelength, and polarization. A small estimation shall demonstrate the demand of such a measurement: Testing fifteen different excitation wavelengths with four distinguished polarization states at five spots on the

[‡]Uniaxial crystals posses one axis differing in refractive index. Waveplates are cut parallel to this axis with the so called "extraordinary ray" polarized along it. That may but doesn't need to be the "slow" axis.

surface, implies a 75 fold precise adjustment of the grey filter position while each waveplate has to be rotated even 400 times. This illustrates the necessity to automate the setup in order to allow for repeatable measurement conditions within a suitable time frame. The workflow of the automated image acquisition is sketched in Figure 3.9. Prior to conducting

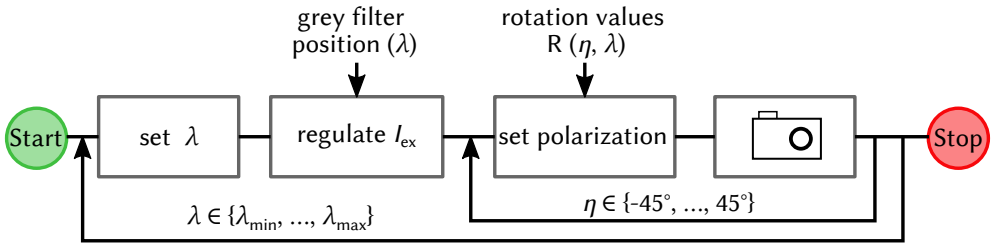

Figure 3.9: Workflow of Automatized Image Acquisition. Once started, the LABVIEW based program enables the spatially resolved acquisition of the sample's PL, iterating over a set range of excitation wavelengths λ and polarization states η by an automated adjustment of the gray filter and waveplate rotation values R.

a measurement series, the system has been calibrated regarding the wavelength dependent grey filter position and the rotation value $R(\eta, \lambda)$ for both, the $\frac{\lambda}{2}$ and $\frac{\lambda}{4}$ waveplate, to obtain light of defined ellipticity η at the samples' position. These calibration files and a list of the tested wavelengths has been fed to a self-written LABVIEW program which manages the image acquisition. Firstly, the laser is set to an operation wavelength and the gradient grey filter is accordingly positioned using a mechanical stage. Next, the waveplates situated in motorized rotational mounts (*ELL14K*, THORLABS) are rotated to their respective position. A beam block, placed on a motorized flip mount in the excitation path, is removed and subsequent to an equilibration period of 2 s, the sample's PL response integrated over 3 s is acquired at the CCD camera. The beam block is reinserted and the acquisition process is repeated, iterating over the polarization states and tested wavelengths.
The as-obtained images are subsequently analyzed based on a PYTHON program, which determines the maximum PL intensity value, removes glitches caused by cosmic rays and integrates the intensity of each image within an area of 40×40 pixels around the PL maximum. Next, the intensity values are sorted with respect to the excitation wavelength and polarization to allow for a calculation of the circular dichroic signal at a respective wavelength.

3.4.3 Time-Resolved Spectroscopy

Although valuable insight on the energy landscape can be obtained by the steady-state spectroscopic techniques discussed thus far, processes happening on different time scales within the excited sample cannot be distinguished. As a consequence, short-lived intermediate states that often play a key role for a material's performance are missed out. Thus, time-resolved techniques have been developed to obtain a more complete picture of the energy

landscape. They monitor the dynamical change of an excited state taking snapshots of its emissive and absorptive properties at different points in time. Information on the radiative recombination capability, defined by the number of excitons for an excitonic material, is gained by time-resolved PL spectroscopy. Time-resolved absorbance measurements on the other hand provide dynamics of the electronic states' population, which is governed by both, excitons and single carriers. A combination of both thus allows to obtain a complete picture and identify i.e. the exact nature of the relaxation channels described in Subsection 2.1.3. Techniques applied within this work for PL and absorbance measurements, time correlated single photon counting (TCSPC) and transient absorption spectroscopy (TAS), are sketched in Figure 3.10.

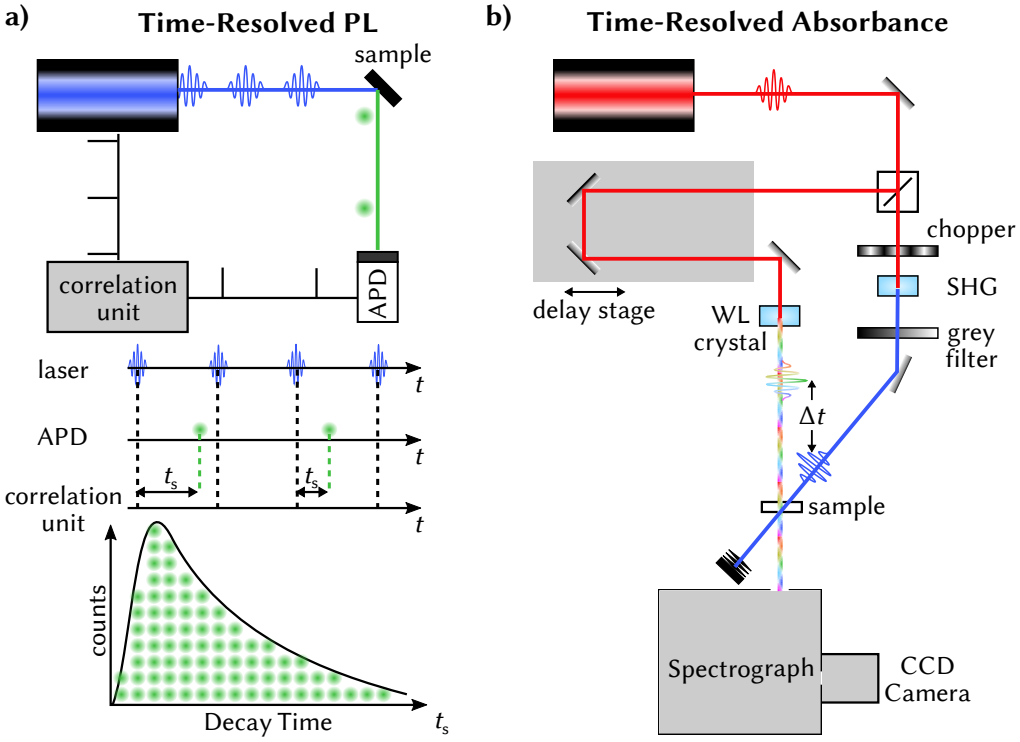

Figure 3.10: Time-resolved Spectroscopy Techniques. a) Time-resolved PL measurement by time correlated single photon counting. TCSPC is based on the stop-watch principle, where a correlation unit allows to temporally match the time of excitation by a laser pulse with the time of detection at an avalanche photodetector (APD) for a correspondingly emitted photon from the excited sample. Delay times t_s for multiple excitation-detection cycles are summed up in a histogram to yield the decay dynamics. **b)** Time-resolved absorbance measurement by transient absorption spectroscopy. An ultrashort 800 nm laser pulse is divided by a beam-splitter into pump and probe pulse, which subsequent to an individual modulation arrive at the sample with a temporal delay δt, While the pump pulse hits a beam stopper, the white-light probe pulse is detected as a spectrum at a CCD camera.

Time correlated Single Photon Counting Spectroscopy

TCSPC spectroscopy monitors the radiative relaxation of an excited state by detecting the single photons emitted subsequent to an excitation.[78,210] A prerequisite for the evolution study is a creation of the excited state at a defined point in time. This is possible using a pulsed laser source. The measurement principle is then based on three parts: the laser to excite the sample, a detector sensitive enough to register a single emitted photon and a unit that correlates the time of excitation and emission (Figure 3.10a).
The laser operated at a repetition rate of 1.22 MHz electronically triggers the time counting unit (*TimeHarp 260 P*, PicoQuant) each time a pulse is sent to the sample. This starts a sweep voltage, which is stopped when an emitted photon arrives at an avalanche photodiode (APD) by sending a signal to the correlation unit.[211] The final voltage value proportional to the evolved time t_s is saved. Multiple excitation-detection cycles allow to obtain a histogram of the photon impacts detected within a certain time window. As shown in Figure 3.10a, not in every excitation cycle a photon is emitted and subsequently detected. On the contrary, the count rate is deliberately kept below 1 % by limiting the excitation power. This accounts for the dead time of the detection system, which cannot process any other events after an incidence for several nanoseconds. Thus, the low count rate assures that a representative statistics is obtained and photons emitted at later points in time are not systematically missed out. The utilized TCSPC setup is integrated in the aforementioned μ-PL setup (see Figure 3.7). Instead of directing the PL signal to a camera, a flip mirror allows to project a small spectral window around the center wavelength of the grating on the fiber coupler connected to the APD.

Overall, TCSPC is a very sensitive technique and even poorly emitting samples can be measured. However, it is limited in terms of its temporal and spectral resolution. As the APD is insensitive to the wavelength of the detected photon, spectral information can only be obtained by sweeping the center wavelengths projected on the fiber end. Additionally, the system depends on electronic signal conversion and processing. This introduces an uncertainty in time in the read out of the APD. Further time uncertainty is introduced by the laser pulse length of 90 ps, causing a slight variation in the time of excitation. Overall, the temporal resolution is limited to approximately 1 ns, as determined with the laser signal itself measured under similar experimental conditions, the so called instrumental response function (IRF). The PL signal shown by the histogram in Figure 3.10 is thus a convolution of this IRF with the true PL signal starting at a sharp point in time. Although a deconvolution is possible, an interpretation of signals shorter than the IRF is tedious. In this case, other systems such as a STREAK-camera that provide a larger temporal and simultaneously spectral resolution are very advantageous.

Transient Absorption Spectroscopy

Apart from time-resolved PL spectroscopy, the evolution of an excited state can be followed based on the change in the sample's absorbance subsequent to an excitation. A sketch of such a transient absorption spectrometer (TAS, Newport Inc.) is shown in Figure 3.10b. The custom-built setup is well described in the PhD theses of Bernhard Bohn[212] and all TAS measurements presented in this thesis have been performed by A. Barfüßer. Thus, only the basic principle is briefly mentioned.
Similar to a conventional absorbance setup discussed in Subsection 3.4.1, the sample is exposed to white light and its wavelength dependent transmission is recorded with a spectrograph (*MS260i*, Newport Inc.), probing the absorbance *OD* of the sample. However, a pulsed illumination is used which – thanks to a femtosecond laser system – provides the desired high temporal resolution. Prior to every second white light probe pulse, the sample is excited with a pump pulse at a temporal offset of Δt which gives the system its name pump-probe spectroscopy. To assure a homogeneous excitation while reducing the number of multiple events, a pump beam diameter much larger than the probe beam and a low excitation density of 15 $\mu J/cm^2$ have been used. The low pulse frequency of 1 kHz allows to block every second pump pulse with a chopper. This generates pairs of spectra, which are used to obtain the differential absorbance $\Delta OD(\Delta t) = OD_{\text{pump}}(\Delta t) - OD_{\text{nopump}}$. The comparison eliminates contributions from non-excited material and thus directly exposes optical transitions blocked or created as a consequence of a depopulation and population of ground state and excited states, respectively. Naturally, the spectrum OD_{pump} depends on the time Δt passed between pump and probe beam hitting the sample. An alteration of this elapsed time allows to obtain the so called transient absorption signal. A defined temporal relation of pump and probe beam is assured by using the same laser source, an 800 nm ultrashort laser pulse with a pulse length of approximately 100 fs (*Libra-HE+ Ti:Sapphire amplifier system*, Coherent Inc.). It is split 98:2 to generate the pump and probe pulse, respectively. While the pump pulse is frequency doubled with the help of a BBO crystal to excite the sample at 400 nm, the probe beam is guided through a delay stage prior to white light generation with the help of a CaF_2 crystal. A variable adjustment of the delay stage then enables to adjust the time delay Δt between the arrival of pump and probe beam at the sample position.

4

Unraveling the Adsorption Process on QDs via Quenching Dynamics

Within this chapter based on Reference 213, I aim to develop a microscopic understanding of the interaction that LHP NCs are exposed to during post-synthetic treatments. Often, metal salts are added for e.g. doping or boosting the luminescence and thereby locally modify the NCs' surrounding. Rather than relying on a defectious NC system that is cured, I focus on the targeted introduction of a luminescence quencher to an initially pristine, highly luminescent NC sample. $CsPbBr_3$ QDs with profound excitonic absorption and emission features are introduced as such a sample in Section 4.1. As the trivalent bismuth atom was established as an efficient quencher upon doping studies, the interaction between these QDs and solubilized $BiBr_3$ salt shall then serve as a model system for a mechanistic study.
In Section 4.2, I provide evidence that $BiBr_3$ acts as a quencher for the QD luminescence by generating trap states at the QDs' surface in a reversible adsorption process. An analysis of quenching dynamics based on a statistical model allowed me to extract the surprisingly severe impact this adsorption imposes on the luminescence. As shown in Section 4.3, already a single adsorption process, i.e. one trap state, is sufficient to completely quench the luminescence of a QD. I expanded this approach in Section 4.4 to obtain a microscopic picture of the interaction, demonstrating that adsorption preferentially occurs on facet junctions and can be effectively limited by the ligand coverage. Finally, the chapter concludes with Section 4.5, where I show the versatility of this approach by investigating the interaction of QDs with other metal salts.

4.1 Spheroidal $CsPbBr_3$ QDs – an Ideal Model System

A mechanistic investigation of interactions between metal salts and NCs relies on a system equipped with certain prerequisites. Firstly, the NCs need to possess characteristic optical features that enable the identification of even slight modifications in the energetic landscape, size or shape. Secondly, an easy modification is required to allow for i.e. size-dependent studies. Finally, the material has to be resistant towards any additional surfactants in order to exclude other than the desired interaction. Among the variety of LHP NCs, spheroidal $CsPbBr_3$ QDs recently introduced by Akkerman et al.[62] present an excellent model system for an in-depth mechanistic study of an additive-QD interaction, as I will show within this section.

Spheroidal $CsPbBr_3$ QDs have been readily synthesized based on the ligand controlled growth method described in Chapter 3. The optical properties of an as-synthesized 6.2 nm $CsPbBr_3$ QD sample are summarized in Figure 4.1. A steady-state absorption spectrum of the QD solution is shown in Figure 4.1a. It features several well distinguished resonances. These resonances have recently been well described by 1S excitonic transitions within a weak confinement model.[63]

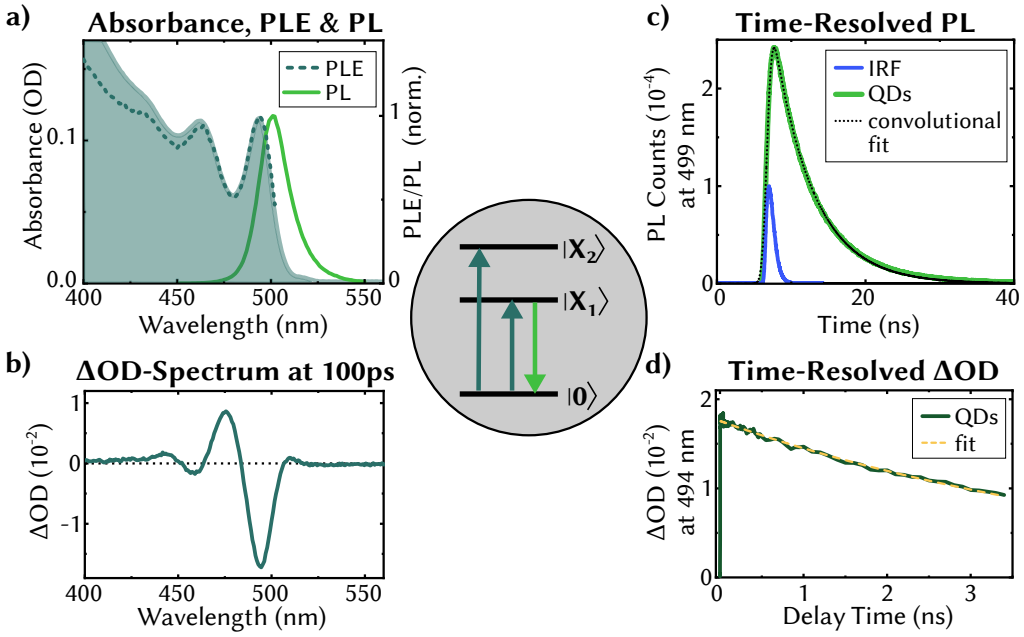

Figure 4.1: Optical Properties of Spheroidal $CsPbBr_3$ QDs. The central sketch depicts the center of mass motion confined excitonic levels which dictate the optical properties of these QDs. **a** Absorption, PLE and PL spectra of a 6.2 nm QD sample. PLE was detected at 505 nm while the PL was excited at 400 nm. **b** Transient absorption spectrum of the QDs upon excitation at 400 nm for a delay of 100 ps. **c** PL recombination dynamics as measured with TCSPC. The QDs were excited at 400 nm and a convolutional fit (black dots) was empolyed to model their monoexponential PL decay (green line) based on the knowledge of the instrumental response function (IRF) (blue line). **d** Transient absorption for the bleach at the fist excitonic transition with a monoexponential fit (dashed yellow line).

In such a system, Wannier-Mott type 1S excitons created upon excitation are confined in their center of mass motion due to the small QD size. As discussed in Subsection 2.1.1, this quantization induces distinguished excitonic states can be labeled by their center of mass motion quantum number as $|X_1\rangle$, $|X_2\rangle$ etc. (central sketch in Figure 4.1). Their position is sensitive to the system's size such that the observation of well resolved resonances can be taken as a sign of the sample's monodispersity. Thus, any changes in the particles dimension by additives would be immediately visible. Using the characteristic position of the first excitonic transition, $\lambda_{X1} = 494\,\text{nm}$, a particle diameter of 6.2 nm, comparable to the exciton Bohr diameter of $\sim 6\,\text{nm}$,[61,63,214] was determined for this sample (see Subsection 3.4.1 for more details).

In addition to the absorbance, these $CsPbBr_3$ QDs also exhibit a characteristic PL signal with a narrow FWHM of less than 19 nm (100 meV). The emission is centered at 499 nm and can thus be attributed to the lowest excitonic transition. Relaxation to the luminescent state is efficient as revealed by the PLE-spectrum in Figure 4.1a. It follows well the absorbance and a PLQY $\approx 69\,\%$ is found upon excitation at 400 nm. Therefore, these QDs readily fulfill the requirement of being a strong and efficient emitter, such that a reduction in their luminescence by a quencher should be well detectable.

Regarding the combination with a quencher, the additional benefit is the pure excitonic system since charge transfer is directly visible by a change in the excitonic absorbance. This is evident from the characteristic ΔOD-spectrum shown in Figure 4.1b, which has been recorded 100 ps after an ultrafast laser pulse has excited the QDs. Negative signals, also referred to as bleach signals, are obtained at the energetic position of the excitonic transitions since these states cannot be excited anymore as single exciton states. Positive signals red-shifted to the excitonic positions on the other hand can be interpreted as the formation of biexcitons reduced in energy compared to the exciton levels due to the biexciton binding energy.[63] The claim of a purely excitonic material is further supported by the recombination dynamics recorded at the PL maximum (Figure 4.1c) and the first excitonic peak position of the ΔOD signal (Figure 4.1d), respectively. As discussed in Subsection 2.1.3, the signal intensity of a purely excitonic recombination decays exponentially according to $I(t) = I_0 \cdot \mathrm{e}^{-k_\mathrm{r} t}$ with k_r referring here to the total recombination rate. A respective fit of the transient ΔOD signal (dashed yellow line in Figure 4.1d) revealed a decay time of $\tau_0 = k_\mathrm{r}^{-1} = 5.2\,\text{ns}$. This agrees well with the value of 5.3 ns obtained from a convolutional fit $G(t) * I(t)$ (black dots in Figure 4.1c) of the time-resolved PL signal. Here, $G(t)$ is a gaussian distribution fit with a width of $\sigma = 0.526\,\text{ns}$ to the IRF. It accounts for the limited time-resolution of a TCSPC-measurement as evident by the $FWHM = 2.3\sigma = 1.2\,\text{ns}$ of the IRF.

Overall, the spheroidal $CsPbBr_3$ QDs are governed by the excitonic energetic level system sketched in Figure 4.1 with a characteristic steady-state and time-resolved absorbance and PL. Thus, these QDs are well suited to monitor any changes when combined with metal salts.

The second key factor making these QDs an excellent candidate for such a study is their lecithin capping in combination with the choice of mild ligands to solubilize the metal salt. Lecithin acts as a bulky organic surfactant at the QD solvent interface. It profits from the chelate effect[180,181] and thus makes the QD resistant against an excess of both ligands that need to be employed in the subsequent mechanistic investigation: lecithin and the metal salt's ligand TOPO, which is known to only weakly interact with the QD surface.[176] I demonstrate this resistivity by the test measurements shown in Figure 4.2. The QDs can withstand an excess of more than 1000 lecithin or TOPO molecules per QD (Figure 4.2a) without any change in their spectral features and luminescent efficiency.

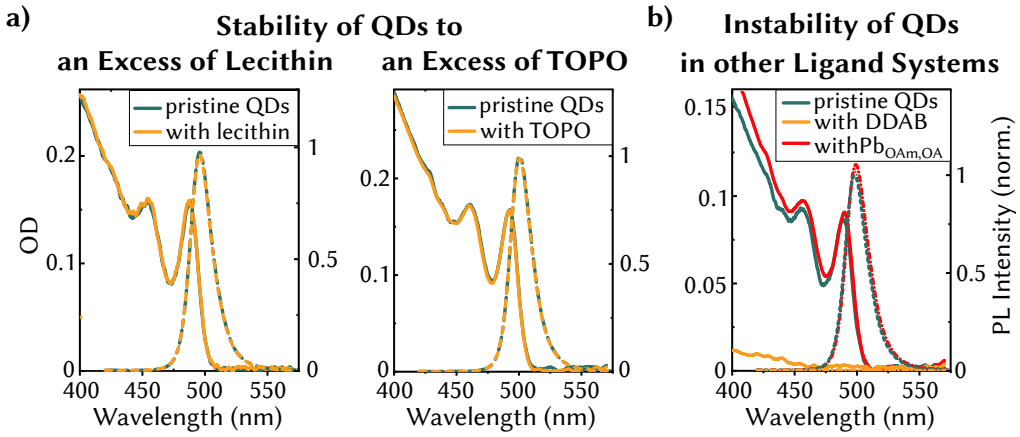

Figure 4.2: Ligand Influence on $CsPbBr_3$ QDs. Change in optical properties upon exposure of 6.2 nm QDs to an excess of different ligands ($\sim 5 \cdot 10^4$ ligands/QD). **a** The stability of the QDs towards the phospholigands lecithin and TOPO is demonstrated based on their unaltered absorbance and PL signal 10 min after addition. **b** The same QDs are heavily affected by the commonly employed ammonium based ligand systems, as demonstrated by treatment with DDAB and a Pb/OAm/OA mixture after the sime time exposure time.

The robustness is an important advantage compared to conventionally used ammonium ligands. This is evident from the comparison of absorbance and PL spectra prior and subsequent to the exposure of a comparable excess of such ligands (Figure 4.2b). Whereas the addition of a Pb/OA/OAm mixture employed in luminescent enhancement of NCs[26] induces a redshift of both, absorbance and PL, an exposure to didodecyldimethylammonium bromide (DDAB) even causes a complete dissolution of the QDs, visible by the loss of its characteristic absorption features within a few minutes after the addition. Thus, using a phospholipid based surfactant system like lecithin that does not suffer from i.e. acid-base equilibrium such as the common OA/OAm system[180,181,185] enables to eliminate ligand related impacts on the QD's optical properties. It has to be mentioned though, that very large excesses of TOPO are known to also cause dissolution of lecithin capped QDs.[176] Thus, the TOPO amount has been carefully controlled to always remain within the stability range.

Finally, I would like to emphasize the precise size control over a broad size range enabled by the chosen synthetic strategy. A set of QD samples covering a size range from 5 nm up to 12 nm diameter is depicted in Figure 4.3. With increasing size, the emission and excitonic resonances redshift as a consequence of reduced confinement. At least three prevalent excitonic absorption resonances are visible for all samples, stressing their monodispersity as also evident from the TEM images. A narrow size distribution and an average size comparable to that determined from the first excitonic absorption resonance using the correlation reported by Akkerman et al.[62] (see Equation 3.7) is found when closely analyzing the TEM images of a 6.2 nm sample. The flexibility to precisely modify the QD size adds to the list of advantages that make these spheroidal $CsPbBr_3$ QDs an ideal model system for an interaction study between QDs and metal salts.

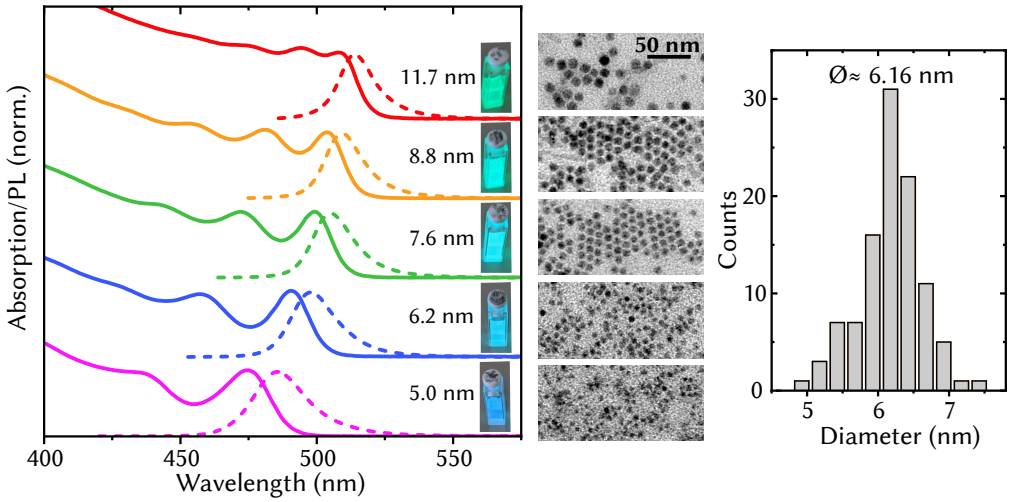

Figure 4.3: Properties of QDs with Variable Size. Absorption and PL spectra for QDs within a size range from 5-12 nm. The inset image show their luminescent color. Sizes were determined from the first excitonic absorption resonance in good agreement with TEM images shown alongside, demonstrating the QDs' spheroidal shape and narrow size distribution as evident from the statistical analysis for a 6.2 nm QD sample.

4.2 Controlled Trap Formation by $BiBr_3$ Adsorption

With a suitable QD model system found, I chose a QD sample of 6.2 nm to investigate the interaction between $CsPbBr_3$ QDs and $BiBr_3$-metal salt during a post-synthetic treatment. The impact of such an interaction has been tested by adding a 53 molar excess of metal salt to a diluted QD solution (75 nM) upon vigorous stirring while monitoring the change of the solution's absorbance and PL in-situ (see Subsection 3.4.1). Through the homogenization and the chosen metal salt excess, at least one $BiBr_3$ moiety should be present in the vicinity of each QD. The impact of the interaction is shown in Figure 4.4 based on the time trace of the integrated PL spectrum and the corresponding absorption spectra at selected points in time

prior and subsequent to the addition of the $BiBr_3$ solution at $t = 0.24$ min.
Within seconds, the photoluminescence drops up to an almost complete quenching of the originally highly luminescent $CsPbBr_3$ QDs. Notably, this quenched state is maintained throughout the recorded time span of 30 min (Figure 4.4a). These two facts hint towards a surface-driven equilibrium process as the root of the quenching: Firstly, with seconds sufficient to quench the luminescence, a surface attachment is very likely. Only anion exchange is known to happen on comparable time scales,[84,215] while bulk material cation exchange reactions at the Pb-site usually require significantly longer time frames.[216] Secondly, the robustness of the quenched state speaks in favor that indeed an equilibrium is reached without subsequent cation exchange taking place on the longer run. This is supported by the fact that the characteristic excitonic absorption resonances are maintained at all time (Figure 4.4a). Neither their position nor their relative intensity is altered, implying a constant size and energetic landscape of the QDs. Only at high energies (at wavelengths below 430 nm), a slight increase in absorbance can be noticed. This might be related to the intrinsic absorption of $BiBr_3$ and its solubilized TOPO complex, as suggested by a comparison with the absorption spectrum of a pure $BiBr_3$-TOPO solution. In line with previous doping studies,[99] $BiBr_3$ thus seems to be an efficient quencher. When applied post-synthetically, it adsorbs on the surface and remains there.

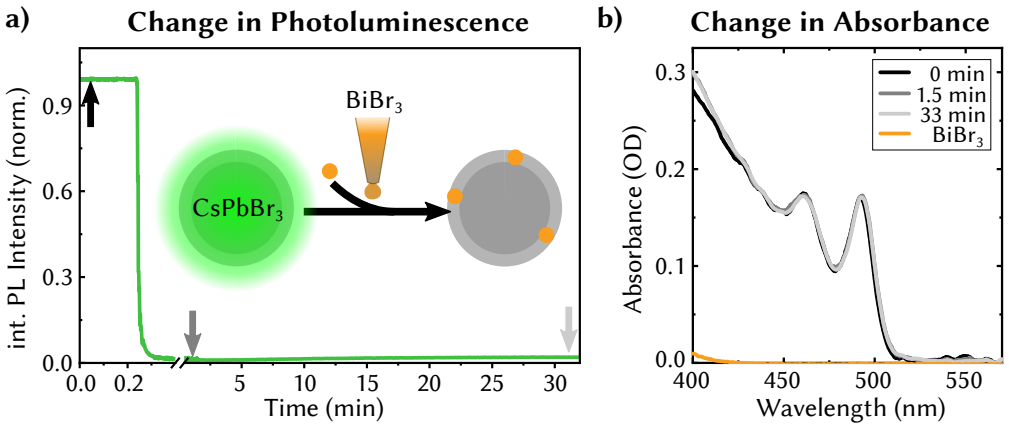

Figure 4.4: Adsorption of $BiBr_3$ on $CsPbBr_3$ QDs. a Change in integrated PL intensity of a 6.2 nm QD sample (75 nM) upon addition of 16 nmol of a $BiBr_3$-solution (53 Bi/QD), monitored in-situ with the addition taking place at 0.24 min. **b** Absorbance at selected points in time. The orange line represents the absorbance of a pure solution of the $BiBr_3$-TOPO complex.

Naturally, the fact that quenching can be observed upon a mere surface attachment raises the question on the exact nature of this process. Quenching may result due to two processes: charge injection from trivalent Bi^{3+} and thus accelerated Auger recombination at the QD, or formation of traps and thus removal of either the exciton or a single charge carrier from the excited state. In order to decipher which of the named effect is dominant, I

prepared a series of QD samples that contain a variable aliquot of $BiBr_3$-solution and analyzed them by means of steady-state and time-resolved spectroscopy techniques. Images of these solutions in Figure 4.5a demonstrate a gradual color change from slightly greenish to brown. This can be related to the concomitant loss of fluorescence as very well visible upon UV-illumination, which can apparently be precisely controlled by an alteration of the added $BiBr_3$ amount. Note that already small amounts of quencher – the smallest aliquot of 4 nmol accounts to approximately 4 Bi/QD added to the solution – cause a significant impact on the PL (Figure 4.5b).

While the PL changes significantly, PLE spectra appear unchanged, even for very low emissive samples with a PLQY $\approx 0.3\,\%$. The PLE spectra have been recorded at an emission wavelength of 505 nm under identical conditions and simply scaled by the luminescence intensity for comparison. As such, relaxation to the emissive state subsequent to the QDs' excitation seems to remain unaltered for those QDs contributing to the emission, taking into account that the absorbance is completely maintained in the $BiBr_3$ treated samples, too (Figure 4.5c). While the PL only probes those QDs which are luminescent, the complete QD ensemble is represented within the absorption spectra. The unaltered absorbance therefore suggests that also QDs subject to a strong quenching caused by their interaction with $BiBr_3$ are characterized by the same excitonic structure. More precisely, this supports the previous claim of a surface adsorption process. In addition, a charge injection which would result in a partial filling of the excited state and thus a reduced absorbance of the respective transition is unlikely.

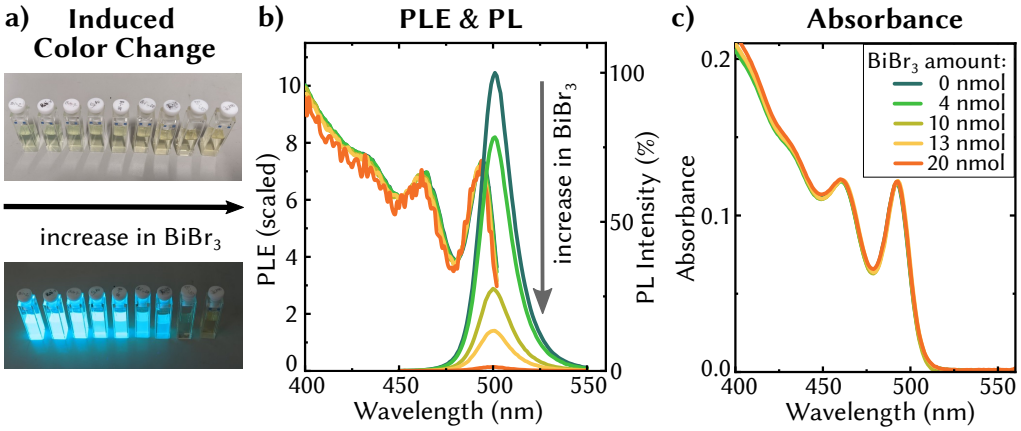

Figure 4.5: Steady-State Spectroscopy of $BiBr_3$-treated $CsPbBr_3$ QDs. a Images show the change in luminescence and color for a series of 6.2 nm QD solutions (0.46 µM) containing a varying amount of $BiBr_3$. **b,c** PLE, PL and absorbance spectra for selected samples. PL was measured upon excitation at 400 nm while PLE was recorded at 505 nm.

Overall, the observed quenching is expected to be ascribable to trapping as sketched in Figure 4.6. In this scenario, trap states introduced by $BiBr_3$ adsorption form an additional non-radiative channel with a decay rate k_{nr} aside the radiative decay channel characterized by k_r. In order to support this claim, power dependent PL measurements have been conducted

(Figure 4.6a). A linear behavior is maintained throughout the tested power range for all samples. However, a dominance of Auger recombination and thus non-linearity would be expected if charge injection was to play a major role. Thus, this result supports the stated scenario. The fact that such a scenario is indeed feasible is additionally supported by reports of DFT calculations.[100] The authors reported that an addition of Bi at a Pb-site and of Br as an interstitial is thermodynamically favorable, but causes the formation of deep traps, which is perfectly in line with my experimental results.

Thus far, it is still unclear if the exciton or only one carrier is trapped. In order to closer pinpoint the nature of the trapping in these post-synthetically modified QDs, the dynamics of the excited state were monitored for the samples subject to different $BiBr_3$ amounts. Firstly, the recombination dynamics have been analyzed by means of the PL signal shown in Figure 4.6b. Most apparent, only a minor change in the decay rate can be identified. As evident in the logarithmic representation, the monoexponential behavior is mostly maintained even for low luminescent samples. However, the initial intensity is drastically reduced. A comparison with the decrease in the samples' PLQY in Table 4.1 shows that this initial intensity is closely correlated to the samples' PLQY reduction. This may be a hint that trapping takes place on a

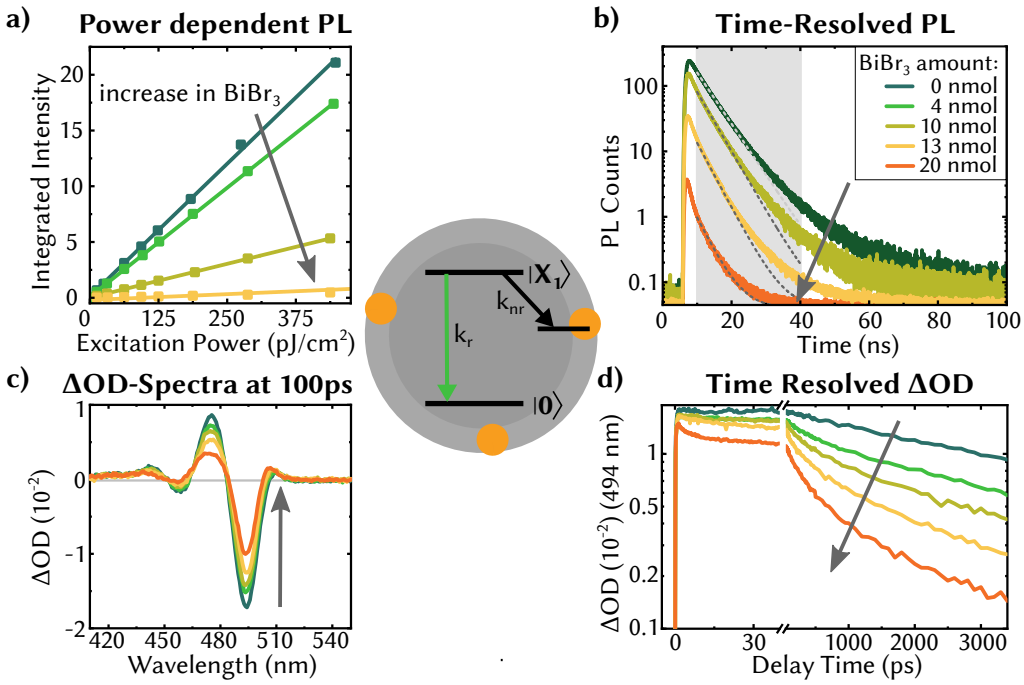

Figure 4.6: Trap Formation in $BiBr_3$ treated $CsPbBr_3$ QDs. The central sketch is a tentative representation of the additional trap level introduced by $BiBr_3$ treatment of the QDs with the radiative, k_r, and trapp realted non-radiative, k_{nr}, decay rates of the treated QDs. **a** Power-dependent PL meausrements for 6.2 nm QD samples with different $BiBr_3$ amounts. The solid lines represent linear fits to the data. **b** PL recombination dynamics as measured with TCSPC. The samples were excited at 400 nm and fit with monoexponential functions (grey dahsed lines) within the marked area. **c** ΔOD spectrum of these QD samples upon excitation at 400 nm for a delay of 100 ps. **d** Transient ΔOD as obtained for the bleach at the fist excitonic transition.

Table 4.1: Fit of Time-Resolved PL upon $BiBr_3$ Treatment.

$BiBr_3$ Amount (nmol)	0	10	13	20
Decay Time τ (ns)	5.5	4.8	4.4	4.1
Amplitude I_0 (cnts)	97.1	65.3	13.2	1.1
PLQY (%)	69	19	9	0.2

time scale not resolved by the TCSPC method limited in time resolution to the nanosecond regime. Additionally, the QDs seem to be still subject to a radiative decay with an almost unchanged recombination rate. This can be explained by a long-lasting (over the time span of the radiative recombination) filling of the QDs' trap states or by a subset of QDs that do not possess any trap state at all.
In order to shine more light on the process, transient absorption measurements that are characterized by a much higher temporal resolution of less than 1 ps have been conducted. The ΔOD spectra are shown in Figure 4.6c and are characterized by the same features as previously described in Section 4.1 for the pristine $CsPbBr_3$ QDs. However, the transient ΔOD signals recorded at the first excitonic peak position (Figure 4.6d) show a complex multiexponential behavior. Fast decay components on the order of a few picoseconds could be observed for samples subject to a $BiBr_3$ treatment. Still, a closer analysis for the sample with the largest $BiBr_3$ amount reveals a residual signal intensity of more than 15 % at a delay time of 1.5 ns. On the contrary, the TCSPC measurement of the same sample possessed a maximum intensity of only 1 % (see Table 4.1). Considering the TCSPC time resolution of $\sim$ 1.5 ns, it can be deduced that the PL signal at a delay time of 1.5 ns is significantly smaller than its transient ΔOD counterpart. This directly implies that only one charge carrier is trapped, in agreement with some previous reports for intrinsically Bi-doped samples.[100,217,218]

Up to this point, I have shown an efficient and controllable introduction of trap states via a post-synthetic treatment of $CsPbBr_3$ QDs with $BiBr_3$. The separation of QD synthesis and trap formation process allowed to clarify the nature of such traps, which has been of debate in literature.[99,218–220] Based on power dependent PL measurements and the maintenance of the steady state absorbance, quenching due to charge injection as reported for single crystalline samples[220,221] could be ruled out for these QDs. Instead, a dominant role of surface based traps states and trapping of only one charge carrier was found by a combined PL and ΔOD time-resolved analysis. The efficacy of surface traps is an important result, as core traps were previously suggested to be necessary for the quenching.[101] Also, it demonstrates that trapping does not necessarily rely on interstitial Br, which was identified as the main cause of quenching in film samples[100,218] based on the interstitial's IR-luminescence not observed within my QD samples. Which charge carrier is trapped in this post-synthetically modified QDs, the electron or the hole, cannot be deduced from the current data but would require

further extensive analysis. I however want to instead exploit the as-identified controlled trap formation to obtain further mechanistic insight to the adsorption process preceding the trap formation.

A couple of questions are raised regarding this process by the presented time-resolved data. Both, the almost unaltered luminescence decay time and the complex multiexponential ΔOD transients suggest that the formed traps are not equally distributed throughout the QD ensemble. Instead, an inhomogeneous adsorption, i.e. the coexistence of QDs with different amounts of trap levels, and a subset of QDs that have no $BiBr_3$ moieties adsorbed at all could explain the observed data. The pristine QDs are expected to dominate the luminescence, matching the almost constant PL recombination rate, but also the unchanged PLE spectral shape. The multi-exponential behavior of transient ΔOD on the other hand can then be understood as a superposition of QDs which are subject to a variable quenching.

In this regard, it would be convenient to find a model for such a distribution of Bi at the QDs that explains the apparent inhomogeneity. It is still unclear how much Bi $\overline{m}_{Bi}$ is actually added on average at a QD for an amount of N_{Bi} $BiBr_3$ moieties added to the solution. Once the number of attached Bi per QD was known, it would also be possible to identify the ratio of radiative and non-radiative trapping, as sketched in Figure 4.7. Although the time-resolved ΔOD data reveal that trapping can be very fast with decay components on a timescale of tens of picoseconds observed, it is tedious to extract the non-radiative trap rate without the knowledge of the adsorbed $BiBr_3$ moieties. For the often as defect tolerant considered $CsPbBr_3$ QDs, it would be surprising if this decay components represented the rate of a single trap, knowing that the radiative decay rate is much slower. Thus, it is very interesting to clarify how much $BiBr_3$ is actually needed to quench a QD. Is it gradually "turned off" by the adsorption of several $BiBr_3$ moieties or is a single trap sufficient?

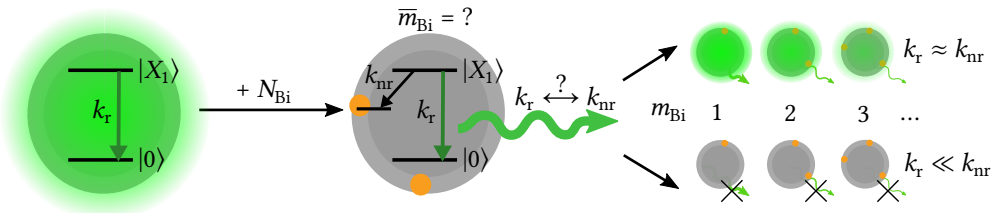

Figure 4.7: PL-Quenching of $BiBr_3$ treated $CsPbBr_3$ QDs. Upon addition of N_{Bi} to a QD solution, an average number of $\overline{m}_{Bi}$ adsorbs at the QD creating trap states. These are characterized by a non-radiative decay rate k_{nr} whose ratio to the radiative decay rate k_r determines how much Bi is needed to completely quench a QD.

4.3 A Statistical Model for Metal Salt-QD Interactions

In order to tackle the aforementioned question, a major focus was placed on analyzing the quenching dynamics for the $BiBr_3$-QD interaction. This was introduced in Subsection 2.2.3 as a powerful tool and exploits the characteristic shape of the concentration dependent PL intensity reduction. Thus, I conducted a titration of the $CsPbBr_3$ QDs with $BiBr_3$ as the quencher. This is shown in Figure 4.8. With an in-situ setup (see Subsection 3.4.1), the reduction in PL intensity has been recorded as a function of time while repeatedly adding aliquots of $BiBr_3$ to step by step form traps at the QDs (Figure 4.8a). The total added volume has been kept small enough to ensure that dilution effects can be neglected. A transformation from time-domain to concentration reveals the Stern-Volmer plot (Figure 4.8b). The quenching appears to be strictly exponential and can be well fitted with a monoexponential function

$$I(c_{\mathrm{Bi}}) = I_0 \cdot \mathrm{e}^{-0.66 c_{\mathrm{Bi}}/\mu\mathrm{M}}. \tag{4.1}$$

Quenching mechanisms with their respective characteristic Stern-Volmer equations have been introduced in-depth in Subsection 2.2.3. Evidently, the simple homogeneous quenching models with their $I_0/I \propto c_{\mathrm{Bi}}$ relation do not match the observed quenching dynamics. Such a model would be expected, if an identical equilibrium between dissolved and adsorbed $BiBr_3$ was present for each QD. Instead, as suspected based on the time-resolved analysis in Section 4.2, the $BiBr_3$ quenchers interact inhomogeneously with the QDs.
An inhomogeneity in the point in time of interaction for different QDs, i.e. the distant dependent quenching (DDQ) quenching mechanism, is unlikely. Such a timely varying interaction would result in a significant alteration of the QD ensemble's lifetime. However, this is not supported by the data presented in Section 4.2. Furthermore, diffusion through the

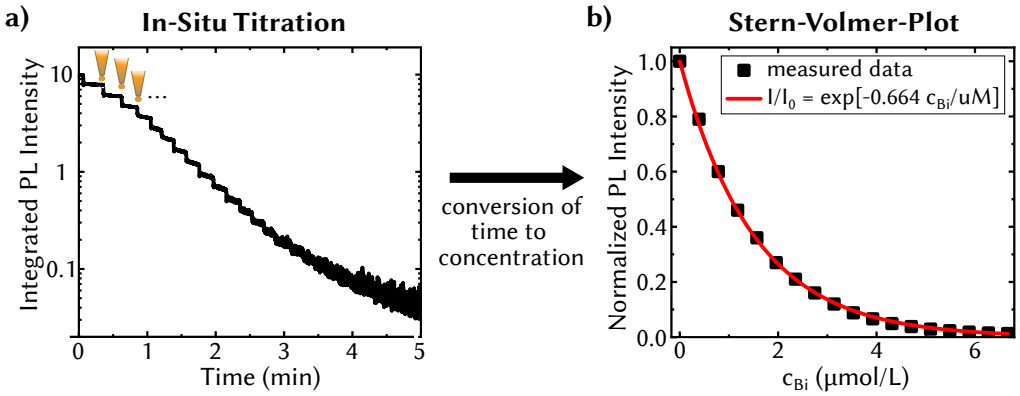

Figure 4.8: Quenching Dynamics of $CsPbBr_3$ QDs. **a** Titration of a 0.2 µM QD solution with defined $BiBr_3$-aliquots (0.8 nmol), recorded in-situ as a function of time based on the PL signal upon excitation at 365 nm. **b** Stern-Volmer plot for $BiBr_3$ adsorption as obtained form this stepwise reduction in PL intensity.

organic surfactant layer at the QDs is assumed to be slow compared to diffusion in the organic solvent hexane, given the high viscosity of lipid layers.[222] However, only if this process happened within the lifetime of the QDs' excited state could the observed inhomogeneous quenching be explained by a timely variation of attached quenchers. In combination with the absence of a significant change in lifetime, a static number of $BiBr_3$ at a QD is thus assumed to characterize each excitation cycle. Therefore, rather the Sphere of Action model, where the cause of inhomogeneity lies in a static but statistical distribution of $BiBr_3$ at the QDs, might explain the observed quenching.

The Sphere of Action model has originally been developed for molecules: it assumes a statistical distribution of quenchers in the solution and it defines a volume fraction V_{int} surrounding the molecule called its sphere of action, within which an immediate collision induced quenching occurs once a quencher is present (see Subsection 2.2.3). The occurrence of such a distribution in case of $BiBr_3$ addition to a QD solution can be understood by the post-synthetic modification process. When an aliquot containing a number of N_{Bi} $BiBr_3$ moieties is injected in the QD solution of total volume V, the vigorous stirring assures that all injected $BiBr_3$ are statistically distributed within the solution's volume. Thus, the probability that a $BiBr_3$ moiety ends up in a small volume aliquot V_{int} that contains a QD is:

$$P_{\text{QD}} = \frac{V_{\text{int}}}{V} \tag{4.2}$$

According to the model, the sphere of action with its volume V_{int} is chosen such that an interaction between a quencher, $BiBr_3$, and a QD is assured. Naturally, the dilution of the solution has to be kept large to ensure that no more than one QD is present within the volume V_{int}, i.e. that the QDs independently interact with the $BiBr_3$ moieties. In such a case $P_{\text{QD}} \ll 1$ and the probability of a QD to simultaneously interact with m $BiBr_3$ moieties is obtained according to Equation 2.20 by a Poisson distribution as:

$$P_m = \frac{\left(N_{\text{Bi}} P_{\text{QD}}\right)^m}{m!} \mathrm{e}^{-N_{\text{Bi}} P_{\text{QD}}} \tag{4.3}$$

Thus far, the assumptions are identical to the classical Sphere of Action model. Now however, modulations need to be introduced. The classical model does not distinguish whether one or several quenchers occupy the defined sphere of action. Once one quencher is present, deactivation is assumed to occur immediately by collision. Here however, the deactivation process is linked to adsorption of $BiBr_3$ and the thereby induced trapping. One trap is not per se sufficient to deactivate the PL. This is subject of Subsection 4.3.1. Furthermore, with a physical contact between $BiBr_3$ assumed to be present, the sphere of action cannot be interpreted as a radius for the collision anymore. In view of this fact, the meaning of the sphere of action for the metal salt-QD interaction will be discussed in detail in Subsection 4.3.2.

4.3.1 A Single Trap State is the Quencher

The identified Poisson distribution for the interaction between QDs and $BiBr_3$ is sketched in Figure 4.9a. It can be utilized to estimate the expected emission intensity upon addition of a certain number of $BiBr_3$ moieties N_{Bi} to a QD solution. This is demonstrated in Figure 4.9b.

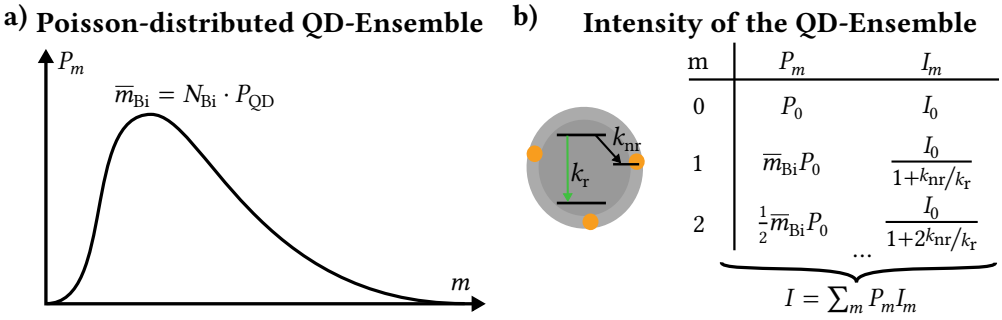

Figure 4.9: The Statistical Model for the Interaction Process. a Probability distribution for a QD to interact with m $BiBr_3$ moieties. The average number $\overline{m}_{Bi}$ depends on the total added amount N_{Bi} and the probability P_{QD} to interact with one $BiBr_3$ moiety. **a** Each QD is characterized by a corresponding PL intensity I_m, that depends on the strength of the formed trap state ($k_{nr} \leftrightarrow k_r$). For simplicity, only radiative recombination is assumed for the pristine QD.

As mentioned above, one trap is not per se sufficient to deactivate the luminescence of a QD, but only reduces its luminescence according to Equation 2.14. As such, the expected steady-state emission intensity upon addition of N_{Bi} for a solution containing one QD cannot be simply defined via the probability to not find a quencher in the environment, i.e. P_0. Instead, it is given by its intensity I_m upon interaction with m_{Bi} $BiBr_3$, weighted by the probability P_m for this interaction to occur:

$$I(N_{Bi}) = \sum_{m=0}^{N_{Bi}} P_m I_m \underset{\uparrow}{=} I_0 e^{-N_{Bi}P_{QD}} \sum_{m=0}^{N_{Bi}} \frac{(N_{Bi}P_{QD})^m}{m!(1 + k_{nr}\tau_0 m)} \tag{4.4}$$

Equation 2.14, 4.3

Of course, a QD solution does not only contain one QD but millions. Considering that for each QD the probability to interact with a $BiBr_3$ moiety is identical and independent of the presence of other QDs, the same relation characterizes the intensity of the overall QD solution. In other words, as long as interactions between QDs can be excluded, the relative quenching is not influenced by the overall dilution of the solution and Equation 4.4 can be directly applied to predict the solution's quenching dynamics presented in the Stern-Volmer plot in Figure 4.8. A comparison of the preliminary fit function (Equation 4.1) with Equation 4.4 already suggests that the sum term in Equation 4.4 is approximately unity, considering that $N_{Bi}P_{QD} = c_{Bi}N_A V_{int}$. This is only true if $k_{nr}\tau_0 = {}^{k_{nr}}/_{k_r} \gg 1$. Thus, this allows to arrive at a substantial conclusion: A single trap state, i.e. the interaction with only one $BiBr_3$ moiety, is sufficient to quench a QD!

To put a figure on the trapping rate k_{nr}, the quenching dynamics was analyzed including the sum term in Equation 4.4. Knowing that N_{Bi} is very large, the sum relation is not very practical since it requires significant computational effort. It can therefore be approximated with the help of a gamma function, assuming that $N_{Bi} \to \infty$:

$$\begin{aligned} I(c_{Bi}) &\approx I_0 e^{-c_{Bi}N_A V_{int}} \sum_{m=0}^{\infty} \frac{(c_{Bi}N_A V_{int})^m}{m!(1+k_{nr}\tau_0 m)} \\ &\underset{N_{Bi}\to\infty}{=} I_0 e^{-c_{Bi}N_A V_{int}} \left[\frac{1}{k_{nr}\tau_0} (-c_{Bi}N_A V_{int})^{-(k_{nr}\tau_0)^{-1}} \int_0^{-c_{Bi}N_A V_{int}} e^{-t} \cdot t^{(k_{nr}\tau_0)^{-1}-1} \, dt \right] \end{aligned} \tag{4.5}$$

A respective adjustment upon variation of the unknown parameters, V_{int} and k_{nr}, has been conducted as presented in Figure 4.10. The radiative decay time of $\tau_0 = k_r^{-1} = 5.2$ ns obtained for the pristine QDs (see Section 4.1) was used, while V_{int} and k_{nr} were adjusted. Evidently, a good fit is obtained only for large values of $k_{nr} \approx 500 k_r = 0.1\,ps^{-1}$. This is consistent with the fast relaxation on the order of picoseconds observed in the ΔOD transients (see Section 4.2). Thus, the presented analysis supports that deep traps are formed upon interaction with $BiBr_3$, and allows to conclude that apparently only one trap is sufficient to quench a QD. As such, quenching dynamics upon $BiBr_3$-adsorption on $CsPbBr_3$ QDs can be well predicted by

$$I(c_{Bi}) = I_0 e^{-N_{Bi}P_{QD}} = I_0 e^{-c_{Bi}N_A V_{int}} \tag{4.6}$$

This relation is indeed very useful itself to obtain more insight on the adsorption mechanism. Firstly, it allows to estimate the average number of adsorbed $BiBr_3$ moieties $\overline{m}_{Bi}$ for a solution quenched to a certain state. According to the Poisson distribution shown in Figure 4.9,

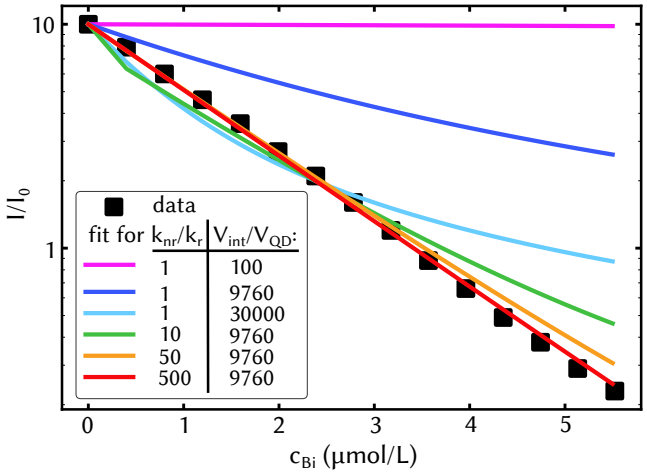

Figure 4.10: Prediction of PL Quenching for $BiBr_3$ treated $CsPbBr_3$ QDs. The experimental data (black dots) are compared with predicted quenching dynamics characterized by a certain trap strength k_{nr}/k_r and the size of the interaction sphere V_{int}, related to the QD volume V_{QD}.

$\overline{m}_{Bi}$ is directly obtained from the exponent as

$$\overline{m}_{Bi} = N_{Bi} P_{QD} \underset{\text{Equation 4.6}}{=} \ln\left(\frac{I_0}{I}\right) \tag{4.7}$$

Values of $\overline{m}_{Bi} \leq 4.3$ are found. Given the QDs' size of 6.2 nm, this yields an average Bi/Pb content of less than 0.8 % during the quenching experiment, comparable to previous Bi levels upon intrinsic doping.[99,223]

The second important result is hidden in the slope of the exponential function. A comparison of Equation 4.1 and 4.6 reveals the interaction sphere volume V_{int} that represents the volume aliquot occupied by a QD. Surprisingly, this is not simply the QD volume, but includes a large space of solution around. Actually, the mismatch accounts for 4 orders of magnitude (Figure 4.10). A special focus shall thus be placed on interpreting this sphere of action.

4.3.2 The Sphere of Action for QDs

Intuitively, the QD's volume would be expected to coincide with the interaction sphere, considering that trapping requires a physical contact between the QD and its quencher $BiBr_3$. Thus, the sphere of action does not represent the actual location of the $BiBr_3$-quencher, but the outreach of the surface potential of a QD, as sketched in Figure 4.11a.

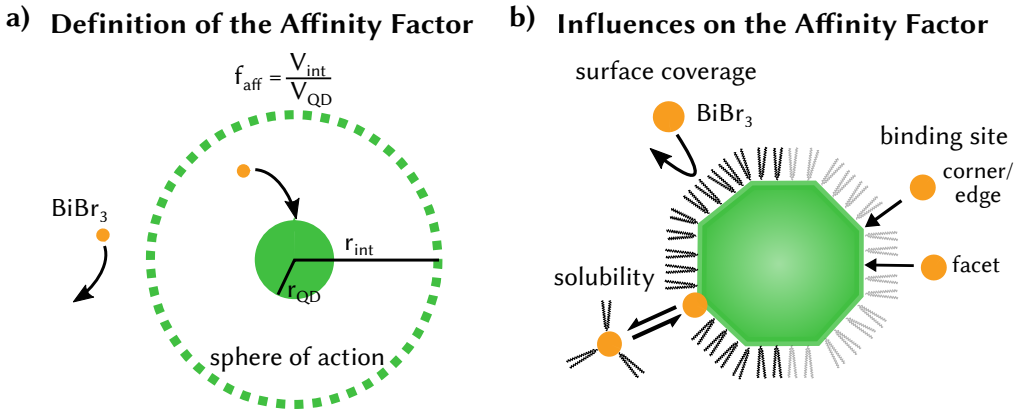

Figure 4.11: The Affinity Factor. a The sphere of action (dashed green line) of a QD (green) is defined as the region wherein $BiBr_3$ moieties (orange) diffuse to the surface and get adsorbed, characterized by their volumetric ratio called the affinity factor. **b** With the quencher's solubility, the QD's coverage by surfactants and the distinctive crystallographic binding sites three common factors of influence for the affinity factor are depicted.

Within a certain range around the QD, the bismuth metal salt diffuses to the surface and gets adsorbed. As such, the size of the sphere of action is determined by the ease with which a $BiBr_3$ permeates the ligand shell, and the strength for its adsorption at the QD surface. In fact, it is much more favorable for a $BiBr_3$ to be adsorbed on the QD´s surface compared to

lingering in solution. In other words, the probability for a $BiBr_3$ to interact with a QD is increased beyond the mere statistically driven factor $P_{QD,stat} = {}^{V_{QD}}/_{V}$ which would result if $BiBr_3$ had no preference for a localization on the surface compared to the solution. In order to describe the deviation between $P_{QD,stat}$ and the actual probability P_{QD} (Equation 4.2) that results from this affinity of $BiBr_3$ to the QD surface, a so called affinity factor

$$f_{aff} = \frac{P_{QD}}{P_{QD,stat}} = \frac{V_{int}}{V_{QD}} \tag{4.8}$$

is introduced. This affinity factor is dependent on a number of surface inherent properties as exemplary shown in Figure 4.11b for three main impacts. Firstly, the ligand shell itself imposes a barrier for the adsorption, that is characterized by its density and the ligand's binding strength to a surface site. Accordingly, the solubility of $BiBr_3$ by i.e. an appropriate complexation agents will compete with its adsorption at the QD's surface. Secondly, the QD itself may exhibit binding sites of different affinity, with the structurally distinguished facets, corners and edges as presumable candidates.

4.4 Making Use of the Surface Dependent Affinity

The affinity's dependence on inherent surface properties is a useful tool to unravel factors that steer the adsorption process. A simple steady-state PL measurement while forming traps through adsorption of $BiBr_3$ is sufficient to obtain the affinity factor. Now, suitable parameters linked to the respective surface property need to be identified and varied accordingly. The characteristic change in affinity should then reveal the property under debate.

4.4.1 Facet Junctions are the Anchor Points

At first, I would like to pursue which is the favored binding site at the QD's surface. Three distinct sites – facets, edges, and corners – have been introduced in Figure 4.11. A parameter that is inextricably linked with their respective surface contribution is the QD's size. Figure 4.12a illustrates how the surface fraction occupied by the corners is altered when the size of the QD is varied. While the number of corners is constant upon an increase in size, the facets grow with the QD radius's square. Thus, the contribution of the corners is significantly reduced for larger sized QDs. This fact can be exploited to identify the major binding site. Generally, with adsorption being a surface effect, the affinity can be divided into parts proportional to the binding sites' contribution to the QD surface A_s:

$$f_{aff} = \sum_{i=c,e,f} f_i^{'} N_i \frac{A_i}{A_s} = \frac{f_c}{r^2} + \frac{f_e}{r} + f_f \tag{4.9}$$

Here, f_i', N_i, and A_i denote the specific affinity, the number of occurrence and the surface area occupied by one binding site, respectively, while the labels *c*, *e*, and *f* represent corners, edges and facets. The surface area A_s increases with the square r^2 of the QD radius *r*, while the shape of the QD is approximately the same. This is explicated in the second equivalence. It joins all constants while accounting for the fact that the number of binding sites N_i is stationary, proportional to the QD's radius *r* or to its square r^2 for corners, edges and facets, respectively. Thus, if one can succeed to vary the QD size while keeping the probability for a $BiBr_3$ to come across a QD constant, the functional dependence of Equation 4.9 will enable to tell the contribution of different binding sites apart. This prerequisite is fulfilled when the volume fraction f_{Cs}, i.e. the total volume of $CsPbBr_3$ present per solution aliquot, is kept constant according to

$$c_{Bi} N_A V_{int} = \frac{N_{Bi}}{N_{QD}} f_{Cs} f_{aff}. \tag{4.10}$$

The number of Bi per QD in Equation 4.10 is equivalent to the number of Bi per exciton. This is the relevant quantity in terms of trapping. Thus, I used it for comparing the PL intensity reduction recorded for differently sized QDs. These quenching dynamics are shown in a logarithmic representation in Figure 4.12b. A rearrangement of Equation 4.6 reveals that the

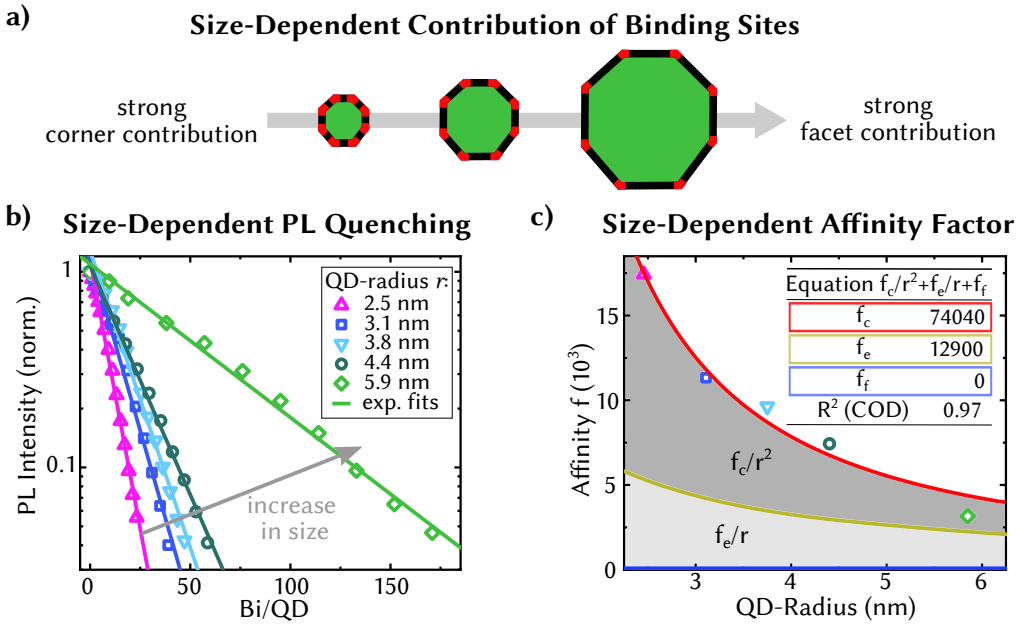

Figure 4.12: Identification of Bindings Sites by the Size-Dependent Affinity. **a** Graphical representation of the surface contribution of corners (red) and facets (black) upon variation of the QD's radius. **b** Quenching dynamics for $CsPbBr_3$ QDs of various sizes upon addition of $BiBr_3$ and their fit with exponential functions. A constant $CsPbBr_3$ volume fraction of $7.25 \cdot 10^{-6}$ was assured and an extra added amount of lecithin set its concentration in solution to 100 µmol L^{-1}. **c** Size dependence of the affinity factor. The functional expression from Equation 4.9 was fitted to the data set extracted from the quenching dynamics.

obtained slope is a direct measure for the change in the affinity factor:

$$\ln\left(\frac{I}{I_0}\right) \underset{\uparrow}{=} -\frac{N_{\mathrm{Bi}}}{N_{\mathrm{QD}}} f_{\mathrm{Cs}} f_{\mathrm{aff}}. \tag{4.11}$$

Equation 4.10

A significant decrease in slope with increasing QD size occurs, with the affinity as a function of QD radius r depicted in Figure 4.12c. The functional dependence from Equation 4.9 is shown, too, revealing an amplitude ratio of 5.75:1:0 for corners:edges:facets, respectively, with the corner and edge contribution marked accordingly. This clearly demonstrates that, especially for smaller QDs, corners are the major point of entrance to the QD's surface. The outstanding role of corners and edges may be rationalized in a microscopic picture: They are prone to possess a higher surface potential[224,225] combined with a reduced density in ligand coverage at the corners and edges, taking into account that the major anchor points for ligands are the facets.[188,226]

4.4.2 The Ligand Coverage Competes with Adsorption

Throughout the preceding discussion on the size dependent affinity factor, the intrinsic concentration of lecithin as the QDs' surfactant was kept constant at $100\,\mu\mathrm{mol\,L^{-1}}$. This served to compensate any variations in ligand coverage that may appear from the QDs' synthesis: in the final synthesis step, a fixed amount of lecithin is added while the surface fraction will vary with QD size. A size-independent surface coverage however needed to be assured to unmistakably disentangle the binding sites' influence, knowing that the integrity of the surfactant layer itself already has a major impact on the affinity factor, as I will demonstrate within this section.

Upon an increase in lecithin concentration, the quencher $BiBr_3$ and lecithin as the QD's surfactant start to compete for empty binding sites at the QD's surface. At the same time, lecithin may also act as a complexation agent and thus modulate the quencher's solubility. These two processes are depicted in Figure 4.13a. An alteration of the surfactant concentration may help to clarify the competitive role of surfactant and metal salt at the QD's surface. Additionally, it may also provide a hint on the complexation strength for $BiBr_3$ by lecithin. Therefore, I described each process under debate by an analytical model to predict the lecithin dependent change in affinity factor.

For a complex formation, at least one ligand L needs to interact with Bi, i.e. a reaction $\mathrm{Bi} + n\,\mathrm{L} \xrightarrow{\mathrm{k}} [\mathrm{L}_n - \mathrm{Bi}]$ with $n \geq 1$ is assumed. If the complex is very stable, the amount of Bi available for adsorption is reduced to only the non-complexed Bi according to the law of mass action to

$$c_{\mathrm{Bi}} = \frac{c_{\mathrm{Bi},0}}{1 + k c_{\mathrm{L}}^{n}}. \tag{4.12}$$

Here, c_L is the ligand's concentration, $c_{Bi,0}$ the total added Bi amount, and k is the complex formation constant. c_{Bi} is the concentration, that determines the decrease in intensity and enters Equation 4.6. The amount of Bi measured in an actual experiment is however $c_{Bi,0}$. As such, an affinity factor following the functional dependence in Equation 4.12 would be expected, provided that complexation plays a major role.
For the competitive adsorption of the quencher $BiBr_3$ and lecithin on the other hand, a monolayer formation of surfactant can be assumed in terms of a "Langmuir-isotherm model",[227] which is a common model for chemisorbed ligands on QDs.[228–230] In this case, the affinity is represented by a sum of two factors:

$$f_{aff} = A\,(1-\theta) + B = A\left(1 - \frac{c_L}{1/K + c_L}\right) + B. \tag{4.13}$$

The first term is proportional to the fraction of unoccupied surface sites, given by the occupancy rate θ, while the proportionality constant A takes the strength of a $BiBr_3$ adsorption to empty surface sites into account. The constant term B is a measure for the ease of $BiBr_3$ to permeate a perfect surfactant shell. The occupancy rate θ can be expressed in the realm of the Langmuir model as a function of the concentration c_L of the occupant, here lecithin, and its association constant K with the surface.[227]

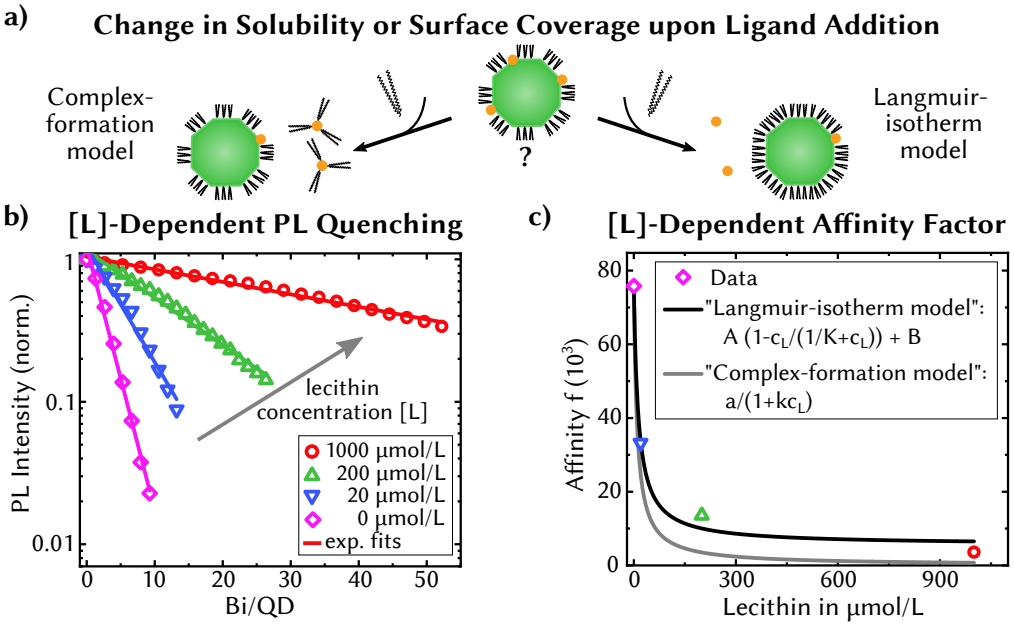

Figure 4.13: Competition of Ligand and Metal Salt Adsorption. a Graphical representation of two possible impacts of an increase in surfactant concentration. **b** Quenching dynamics for $CsPbBr_3$ QDs upon addition of $BiBr_3$ in the presence of a variable lecithin amount. A fixed QD concentration of 0.09 µmol L^{-1} was employed and the data were fit by exponential laws. **c** Dependence of the affinity factor on the lecithin concentration. The functional expression from Equation 4.12 and Equation 4.13 were fit to the data set extracted from the quenching dynamics.

While both models predict a strong reduction in affinity with increasing lecithin content, the exact functional dependence on the lecithin concentration c_L is different. This has been used to assign the major impact. I performed a series of measurements with alternating lecithin concentration for a 5.9 nm sized QD sample. Indeed, the strong reduction in affinity predicted by both models is manifested in a significant slower quenching for higher lecithin contents (see Figure 4.13b). The affinity factor is plotted as a function of lecithin concentration in Figure 4.13c.
Evidently, the Langmuir type coverage describes the steep onset of the affinity much better. As such, the results confirm the formation of a monolayer coverage by the surfactant at the QD surface, in agreement with previous studies for different QD-ligand systems.[229,230] Furthermore, with a ratio of $A : B = 12$, $BiBr_3$ adsorption at empty surface sites dominates compared to its diffusion through a ligand shell, with the surfactant apparently effectively shielding the QD surface. Thus, care has to be taken when comparing different samples to make sure that a comparable occupancy rate θ is maintained. Finally, complexation of $BiBr_3$ seems to play a minor role. Though trivalent ions have been reported to show an interact with lecithin,[231] the presented results suggest that it cannot compete with the $BiBr_3$ adsorption at the QD surface.

4.5 The Versatility of Post-Synthetic Surface Treatments

The investigation of quenching dynamics in conjunction with the sphere of action model has thus far proven to be a valuable tool that allowed to develop a microscopic understanding of the adsorption process and uncover key parameters. With its precisely controlled trap formation taking place at the surface only, the adsorption of $BiBr_3$ served as an ideal model system in this context and allowed to focus on the adsorption mechanism only. However, for systems where the basic assumptions of slow diffusion and an equilibrium process hold, the same statistical description should generally be applicable.

For instance, assume a metal salt does not provoke quenching but possesses a comparable affinity to QDs as the quencher $BiBr_3$. Then, it should be capable of expelling the quencher from the QD's interaction sphere, similar to the trap repair during boosting experiments. $PbBr_2$ can serve as such a metal salt according to previous theoretical studies[100] and its use as a PL boosting agent.[26] The addition of $PbBr_2$ subsequent to quenching a QD sample by treatment with $BiBr_3$ has thus been tested with the result shown in Figure 4.14. As demonstrated by the in-situ PL measurement (Figure 4.14a), the QDs are instantaneously quenched by the injection of $BiBr_3$. However, upon a subsequent injection of an excess of $PbBr_2$, the PL can indeed be recovered. This is evident from the integrated spectral intensity with a retrieval of 94 % emission intensity, although over a much longer time frame of 2 h. The simultaneously

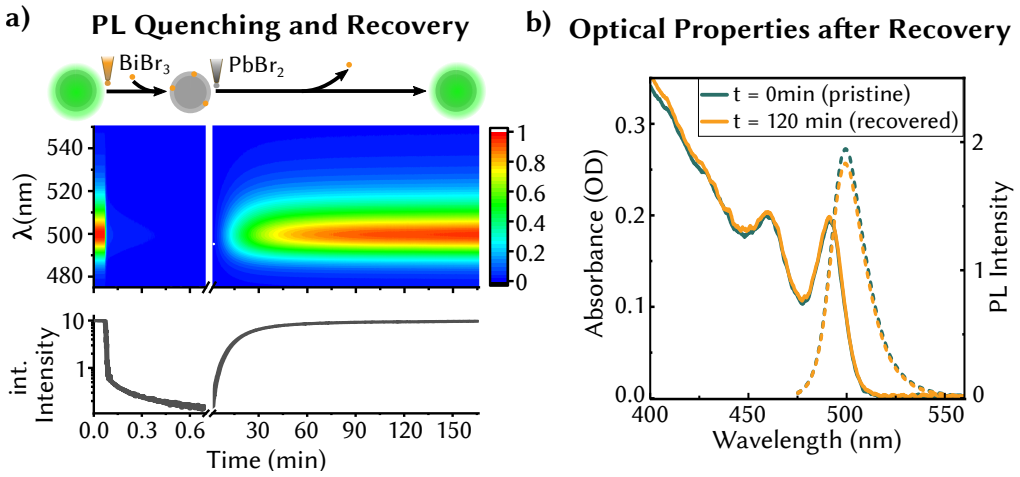

Figure 4.14: PL Recovery upon $PbBr_2$-Treatment. a PL evolution for an 6.2 nm sized QD sample (0.17 µmol L^{-1}) upon addition of (i) an equivalent of 36 Bi/QD $BiBr_3$ followed by the subsequent addition of an equivalent of $1.4 \cdot 10^4$ Pb/QD $PbBr_2$ solution. **b** Absorbance and PL spectra of the as-treated QDs before being subject to any metal salt addition and after 2 h.

acquired absorbance spectra in Figure 4.14b show that the QDs remain intact throughout the complete process.

As such, the Sphere of Action model holds for the addition of mixtures of metal salts, too. According to the principle of Le-Chatelier (which requires that the chemical system adjusts to a new equilibrium that counteracts the externally applied force[232]) $BiBr_3$ is exchanged by $PbBr_2$ competing for adsorption in a statistically driven process. In that sense, $PbBr_2$ induces a reduction in the affinity factor for the $BiBr_3$ adsorption, i.e. the affinity factor becomes a function of the added $PbBr_2$ content. In effect, f_{aff} apparently approaches zero as the $PbBr_2$ content is increased. A huge excess of $PbBr_2$ has to be applied, knowing that only the luminescence of QDs without any $BiBr_3$ present on their surface is recovered. This also explains the incomplete retrieval of the PL emission (94 % recovery), as there is still a slight possibility for the $BiBr_3$ to adsorb to the QD's surface, such that $f_{\text{aff}} \neq 0$. Thus, the fact that the quenching can effectively be revoked may serve as an additional sign for the validity of the introduced statistical model.

Beyond the interaction with the QD inherent $PbBr_2$, the presented versatile post-synthetic modification method should be applicable to characterize the interaction of $CsPbBr_3$ QDs with other metal salts, too. I have thus tested a few metal salts for this purpose. The respective PL evolution observed in-situ upon addition of a 5000 fold excess of various metal salts to a 59 nM QD solution is shown in Figure 4.15. Differences in the interaction behavior for the various metal salts with the QDs are immediately apparent. No impact is observed upon the addition of $InBr_3$ or $ZnBr_2$. $MgBr_2$ however apparently enhances the PL whereas both, $NiBr_2$ and $AuBr_3$, demonstrate a quenching effect. The as-treated solutions have been further

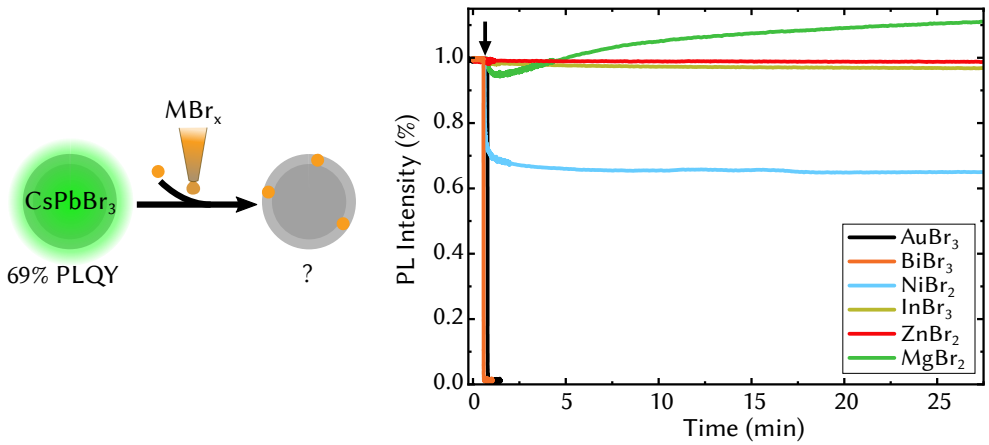

Figure 4.15: Quenching Dynamics for QD-MBr$_x$ Interaction. An excess of a metal salt MBr$_x$ (M = Au, Bi, Ni, In, Zn, Mg) of 5000 M/QD (except 190 Au/QD) was added at a certain point in time (black arrow) to a perovskite QD solution of volume fraction $f = 4 \cdot 10^{-6}$ while monitoring its integrated PL signal as a function of time.

characterized in terms of their optical properties (Figure 4.16). The unaltered absorption and PLE spectra, specifically the consistency of the excitonic resonances' position, confirm the suitability of this post-synthetic treatment for a non-destructive interaction test between these metal salts and the QDs. Minor changes of the absorbance observed upon treatment with $AuBr_3$ and $NiBr_2$ can be explained by the inherent absorption of the respective metal salt solution itself.

As for the luminescence, $AuBr_3$ acts as a specifically strong quencher. The PL decay rate (Figure 4.16c) of as-treated QDs qualitatively appears unchanged compared to a pristine sample but demonstrates a strongly reduced initial intensity. Thus, I speculate that a similar mechanism as for the $BiBr_3$ treated QDs, the formation of deep traps, characterizes these QDs. Bearing in mind that gold is frequently employed as an electrode material in $CsPbBr_3$ based photodetectors,[233,234] the hereby demonstrated impact on the $CsPbBr_3$ QDs' luminescence suggests that such combinations need to be carefully considered. On the other hand, the absence of any impact for In^{3+} and Zn^{2+}, also in terms of their PL decay rate, suggests that they may not interact with the QDs at all. Finally, a shortening in the PL decay is evident from Figure 4.16c for QDs subject to an interaction with both, Mg^{2+} and Ni^{2+}. This fits the observation of an enhanced PL for Mg^{2+}-treated samples in agreement with previous studies.[235] On the contrary, the shortened decay is rather surprising for Ni^{2+} in conjunction with its quenching effect, that also conflicts previous reports of an enhancing effect upon intrinsic doping with nickel.[236–238] However, this enhancement had been associated with structural changes,[236,237] which, given the unaltered absorption, can be ruled out in this post-synthetic treatment. As such, this post-synthetic study suggests that nickel may hold yet another impact on QDs so far not investigated, which for sure requires further attention in future investigations.

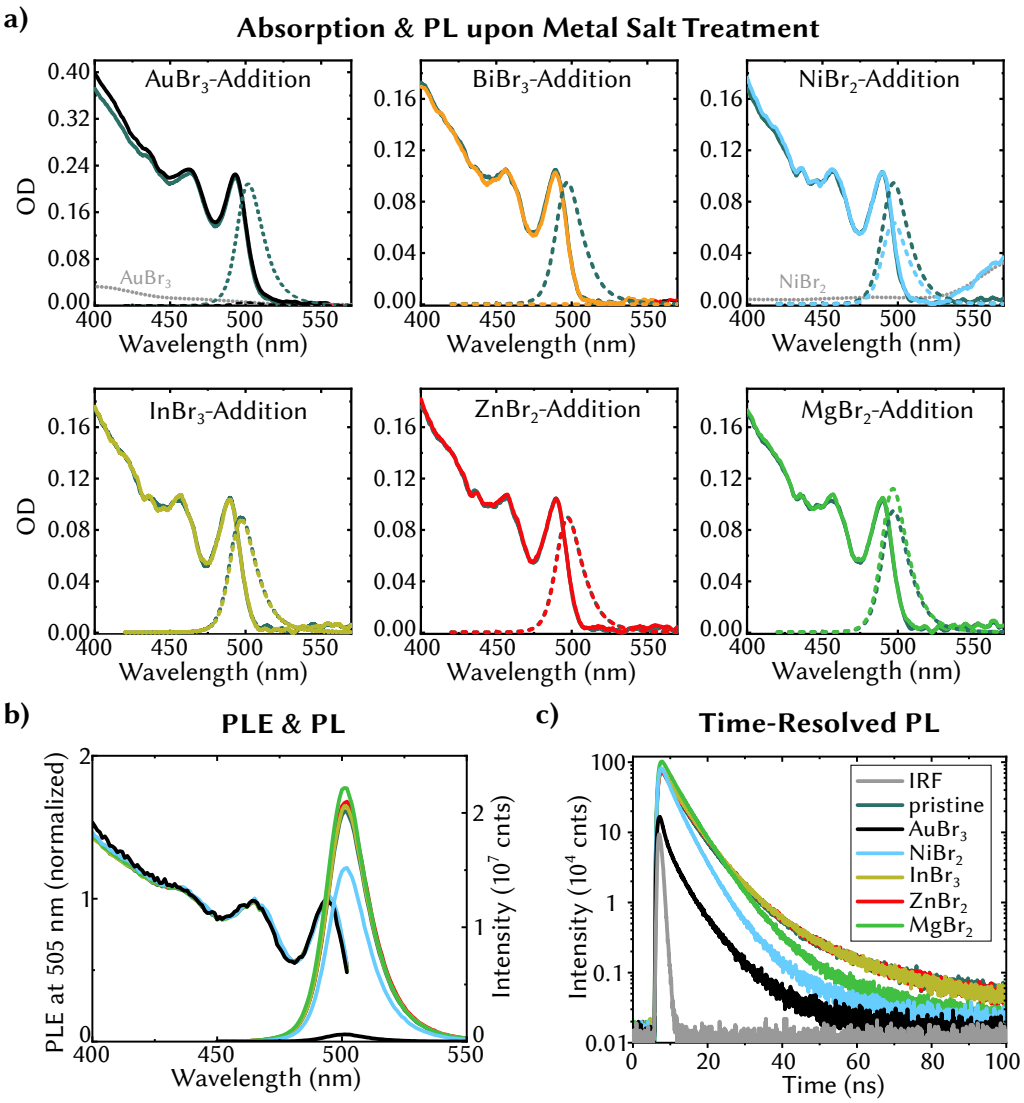

Figure 4.16: Optical Properties of MBr_x-treated $CsPbBr_3$ QDs. The same color code as in Figure 4.15 was employed for the metal salts. **a** Absorbance and PL spectra for $CsPbBr_3$ QDs before (dark green) and subsequent to the addition of the metal salt MBr_x. The intrinsic absorbance of $AuBr_3$ and $NiBr_2$ is depicted in the respective plots. **b** Steady state PL and PLE spectra before (pristine) and after adding the respective metal salt MBr_x. To enable a measurement of the $AuBr_3$-treated sample, the amount of $AuBr_3$ was reduced to 100 Au/QD. **c** PL recombination dynamics of the samples as measured with TCSPC upon excitation at 400 nm.

In conclusion, the study of post-synthetic quenching dynamics presents itself as a valuable addition to the existing tool kit, even though further investigations are necessary for each metal salt to decipher their physical impact. Yet, the theoretical model developed for the quenching dynamics can be flexibly adjusted to account for i.e. energy transfer by an according replacement of the description for the intensity I_m in Equation 4.4. As such, the microscopic understanding of the interaction process gained through the presented analytical treatment for a controlled defect generation can be helpful to promote advances in the application of these – not always defect tolerant – luminescent materials.

5

A Chiral Metasurface Sensitizes the Two-Photon Excitation of QDs

A selective response of LHP QDs to CP light may open up new avenues for sophisticated applications, as highlighted in Subsection 2.3.3. This chapter, based on Reference 177, thus explores the impact of a substrate on a LHP QD's absorption with the aim to enable a circular polarization dependent modification. Such a physical modification of the QD's surrounding is best investigated for a substrate that offers a rich and well-defined interaction with light. Metasurfaces, which upon an asymmetric design may also provide chiral discrimination, are ideal candidates.

In Section 5.1, a rational design of a metasurface that serves the purpose is introduced. Analyzing the surface's reflectance allowed me to reveal its profound chiral resonances in the red spectral range, that could eventually be attributed to scattering of light within the structure. I was able to construct a hybrid perovskite-metasurface via a facile solution-based deposition of self-synthesized cubic LHP QDs as a dense monolayer on the metasurface. This is detailed in Section 5.2. The impact of the substrate on the QD's excitation and emission process for both, above and below band gap excitation, has been quantified in Section 5.3. I provide evidence that the luminescence process is not impacted, while the absorption is enhanced by the excitation light confinement within the metasurface. This finally allowed me to conclude that the observed strong polarization dependent luminescence enhancement for QD in the hybrid system is a direct consequence of the two-photon circular dichroism stemming from the local field enhancement at the metasurface.

5.1 A z-Metasurface for Chiral Light-Matter Interactions

Exploiting a LHP QD's surrounding to achieve a polarization sensitive absorption implies that the substrate needs to provide a discrimination of left and right CP excitation light. A metasurface is perfectly suited for such a task. Both, the shape of the metaatoms and their arrangement as a metasurface are two pivotal parameters enabling a fine adjustment of its optical properties according to the individual requirements. Before diving into the specific design (Subsection 5.1.1) and the optical properties (Subsection 5.1.2) of the metasurface applied within this study, these demands shall be briefly clarified.
Firstly, the desired CP discrimination requires a chiral metasurface, i.e. without an intrinsic mirror plane. Secondly, metasurfaces usually operate in a certain wavelength range. This has to match a below band gap excitation of LHP QDs employed in this study: $CsPbBr_3$ QDs were chosen considering their higher PLQY and enlarged stability compared to their chloride and iodide counterparts.[239] With a band gap of approximately 530 nm,[240] two-photon absorption sets on at an excitation wavelength of 1060 nm. Its absorption cross section increases towards shorter wavelengths with a proportionality to the one-photon absorbance being reported.[241] Thus, a working range of 650 nm to 900 nm was defined. It takes advantage of a larger absorption cross section while still keeping the emission range, where the optical response was probed, and the excitation range well separated. Lastly, a suitable metasurface not only needs to exhibit polarization dependent interactions within the envisaged spectral range, but also avoid a strong absorbance within the metasurface material itself.

5.1.1 The Asymmetric Metasurface Design

With the aforementioned requirements in mind, a suitable metasurface was designed. Absorption related heat dissipation is a major drawback of metallic structures. Thus, I have deliberately chosen amorphous silicon (a-Si) as a dielectric material, which is also advantageous considering its direct compatibility with photonic devices.[242] The symmetry at a metasurface can be broken by the choice of a structurally asymmetric metaatom. A z-shaped, left-handed structure that fulfills this purpose is shown in Figure 5.1a. A total number of five parameters defines this shape: its height D, the core length L_1, its width W_1 and the length and width of the side branches, L_2 and W_2, respectively. Together, they offer a high flexibility for adjusting the metaatom in order to maximize the chiral discrimination within the chosen wavelength range. Additionally, the z-structure is closely related to common symmetric achiral designs, as shown in the electron-microscope images in Figure 5.1a. By omitting or symmetrically adding the side branches, a bar or a double-T structure is obtained, respectively. As such, these achiral structures can serve as references in subsequent optical studies (Subsection 5.1.2) in order to unambiguously pinpoint any determined polarization

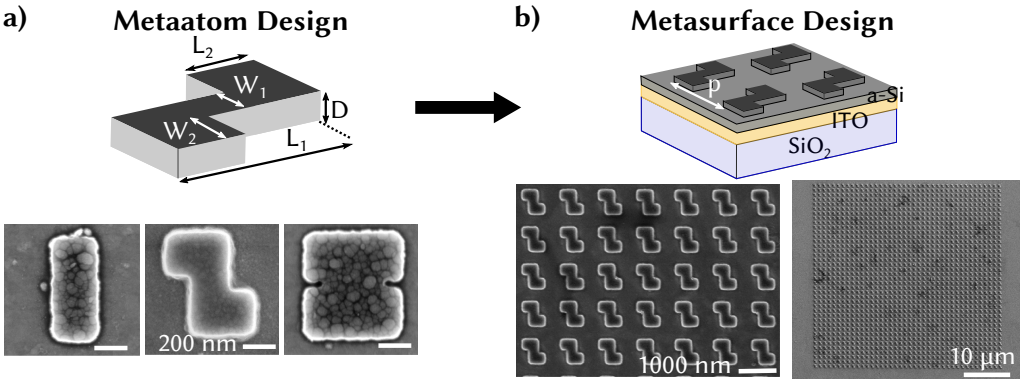

Figure 5.1: Design of the Asymmetric z-Metasurface. **a** Metaatoms were formed from amorphous silicon (a-Si). The subwavelength dimensions of the z-metaatom and its achiral analogues, a bar and a double-T structure, are shown in the SEM images with the scale bars accounting for 200 nm. Optimized z-metaatom dimensions of $L_1 = (637 \pm 7)$ nm, $L_2 = (273 \pm 5)$ nm, $W_1 = (235 \pm 4)$ nm, $W_2 = (151 \pm 8)$ nm, $D = 120$ nm were determined. **b** Z-metaatoms were arranged in a square lattice of periodicity p. The meta-atoms are formed on top of a 13 nm a-Si film and the as-obtained metasurface is located on an ITO-coated SiO_2 wafer. The SEM images show the metasurface dimension with a pitch $p = (980 \pm 10)$ nm and its 40×40 µm^2 area.

effects to the asymmetric structural design of the z-shape. With an already complex metaatom structure providing a five-dimensional parameter space, the metasurface design itself was kept simple. The z-metaatoms were arranged in a square lattice with the only parameter being the lattice periodicity p. This overall metasurface design is shown in Figure 5.1b. As evident, an additional thin layer of 13 nm beneath the z-metaatoms is part of the metasurface. This layer served to avoid any material-related impact on the deposition and arrangement of LHP QDs upon formation of the combined system (see Section 5.2).

Prior to producing and optically probing the z-metasurface, the set of parameters had to be optimized with the aim to achieve a high discrimination of left and right CP light within the chosen wavelength range (650-900 nm). This optimization was performed in collaboration with the *Chair in Hybrid Nanosystems* by D. De Gregorio and F. Wendisch based on finite-difference time-domain (FDTD) simulations with the simulation software from Lumerical Inc. In these simulations, Maxwell's equations are solved for a defined volume space and time around the z-structure, considering that an electromagnetic plane wave of set polarization (right or left) and wavelength (650-900 nm) propagates perpendicularly towards it (more details in Appendix). Its polarization dependent light-matter interactions were visualized based on the electric field distribution within a unit cell of the z-metasurface upon an incident light wave of 833 nm (Figure 5.2a). The color indicates the absolute value of the electric field at the respective spot. The dimensions of the optimized z-structure are clearly subwavelength, with a large pitch of 980 nm. Large field intensities are observed on and around the structure. This may be explained by an excitation of Mie-resonances within the subwavelength scatterer and a resultant scattering of light. Previously, such scattering has been reported to specifically

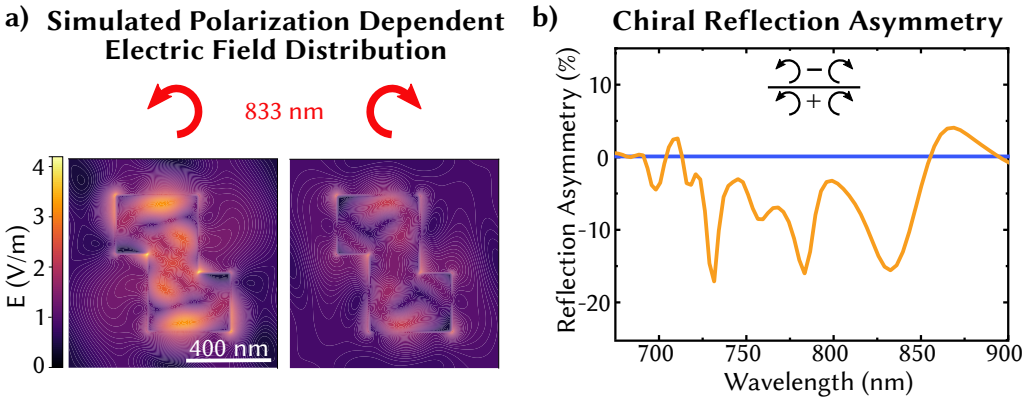

Figure 5.2: Electromagnetic Simulations of the z-Metasurface. A plane wave illumination source at a distance of 2 µm was used, altering its wavelength and polarization. **a** Distribution of absolute electric field values, indicated by the color, within the z-metasurface repetition unit at a height of $D/2$ upon illumination with right/left CP light of 833 nm. **b** Simulated reflection asymmetry δ_R (normalized difference in reflection of left to right CP light) determined at a distance of 3 µm above the z-metasurface. The orange line indicates the z-metasurface response, while the blue line represents a δ_R of zero, i.e. no chiroptical response, and is a guide to the eye.

affect the edges.[131] Additionally, a comparison between the left and right image suggests that the interaction with left CP light is stronger. This intensity difference is representative for the metasurface's ability to discriminate the left and right CP illumination and thus potentially provides a polarization dependent surrounding for any emitters placed on top of it. Certainly, this discrimination depends on the chosen wavelength of illumination.

To obtain a wavelength dependent value which can later be used for comparing the simulated response with experimentally measured data, the integrated signal received by a "detector" placed above the structure has been calculated. Instead of a complex spatial distribution, this yields an integrated value $R(p, \lambda)$ as a measure for the reflected light. It depends on the polarization p and the wavelength λ. With this, the asymmetry δ_R in reflection of CP light can be defined as

$$\delta_R(\lambda) = \frac{R(\mathrm{LCP}, \lambda) - R(\mathrm{RCP}, \lambda)}{R(\mathrm{LCP}, \lambda) + R(\mathrm{RCP}, \lambda)}. \tag{5.1}$$

It ranges from 0 % for an equal response to +100 % (−100 %), if only left (right) CP light is reflected. δ_R is shown as a function of λ in Figure 5.2b. Three major negative resonances are obtained between 700 and 850 nm. The negative sign is an indication that less light is reflected upon left CP illumination. This matches well with a stronger scattering and thus larger near-field values (Figure 5.2a). With such strong polarization dependent modulation within the aimed operation range, the herein presented metasurface structure seems well suited for the envisaged manipulation of the LHP QDs' optical properties. Thus, it has been accordingly fabricated by standard e-beam lithography (see Section 3.3) on ITO-coated SiO_2-wafers. Overall an area of 40 µm edge length was covered with the z-metasurface structure (see Figure 5.1), large enough to enable the subsequent optical characterization.

5.1.2 Chirality Revealed by Reflection Spectroscopy

A thorough optical characterization of the z-metasurface has been conducted prior to applying it as a substrate for the LHP QDs. This deems necessary to later on correlate modifications in the LHP QDs' emission to surface related properties. Thus, I probed the z-metasurface by reflection spectroscopy upon illumination with a tunable pulsed laser beam using the same µ-PL fluorescence microscope as subsequently employed in the detection of the LHP QDs' emission (details on the setup in Subsection 3.4.2). As sketched in Figure 5.3a, a perpendicular illumination was selected to rule out any extrinsic chiral effects. A focal spot size of approximately 5–10 µm^2 covering several z-structures at once assured that a representative surface area was probed.
Classification of the z-metasurface's reflective properties requires to separate material and structure related impacts. As such, the unstructured a-Si area on the same wafer next to the metasurface is a well suited reference. Composed of the same material but free from any structuring, its reflection is representative for the material's intrinsic optical properties. Measurements have thus been always conducted as pairs with the same conditions once for a spot at the z-metasurface and once for an unstructured part of the same wafer. Images as detected with the µ-PL setup upon alteration of the polarization for the incident light beam set to 760 nm are depicted in Figure 5.3b.

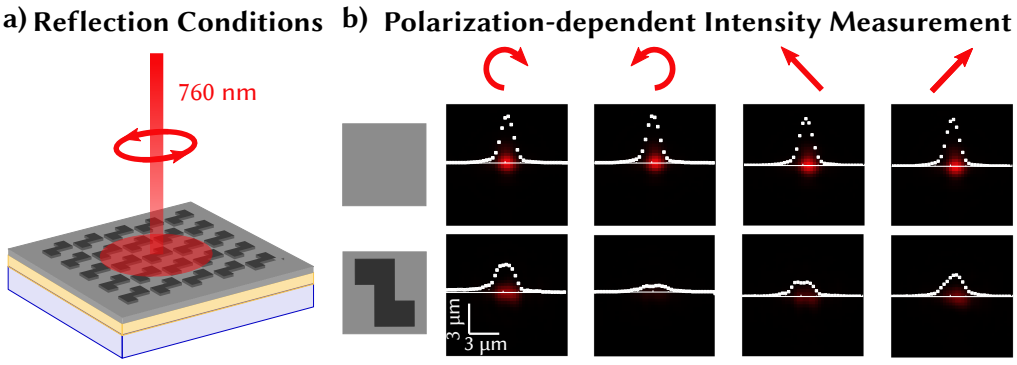

Figure 5.3: Reflective Properties of the z-Metasurface. **a** Sketch of the reflection measurement setup. A focal spot size covering several z-metaatoms (5–10 µm^2) and a perpendicular illumination were maintained. **b** Images of the reflected light detected upon illumination of different surface areas, the z-metasurface or a planar a-Si surface located on the same substrate, with light of defined polarization state. Apart from right and left CP light, linearly polarized light oriented along the z-metaatom or rotated by 90°, respectively, was employed. The white lines each represent the intensity profile along a cross section of the reflection spot.

Apart from CP light, linearly polarized light of two orientations has been tested, either possessing a maximal overlap with the z-structure direction or being rotated by 90° towards it. It is emphasized that it is not the reflected light that has been altered regarding its polarization, but all given polarization states solely refer to the incident light. The white lines represent the reflection spots' intensity profiles for a central cross section. A polarization independent

response is obtained for the reflection at the unstructured surface. This fits well with the expectation for a flat film of an isotropic material such as a-Si. Upon reflection from the z-metasurface, however, the reflected light beam is altered in terms of several aspects: Firstly, the intensity is significantly reduced in comparison to the reflection from the unstructured a-Si surface. Secondly, the spots appear modified in shape, i.e. broadened in one direction. Finally, the extent of intensity reduction significantly changes with the polarization state of the impinging light beam. A particularly strong difference is observed between a reflection of right and left CP light.
I presume that all these effects are directly linked to the structuring of the surface. The reduced reflection is caused by either an increase in scattering or absorption. In conjunction with the change in the reflection's spot shape, an increase in scattering on the edges of the corrugated surface is a likely scenario. The dependence on polarization, specifically the apparent discrimination of right and left CP light, is then suspected to be the consequence of the deliberate metasurface design, in particular the choice of an asymmetrically z-shaped metaatom. This interpretation is supported by the stronger reflection of right compared to left CP light for the chosen illumination at 760 nm. It also agrees with an equivalent behavior predicted from electromagnetic simulations presented in Figure 5.2.

The simulation additionally predicted a wavelength dependent effect with a characteristic line shape for the reflection asymmetry δ_R. Thus, the polarization dependent reflection has been analogously analyzed as a function of the incident wavelength within a broad range from 400 nm up to 800 nm (Figure 5.4). The acquired images have been integrated in terms of their intensity to yield a measure for the polarization and wavelength dependent reflectance

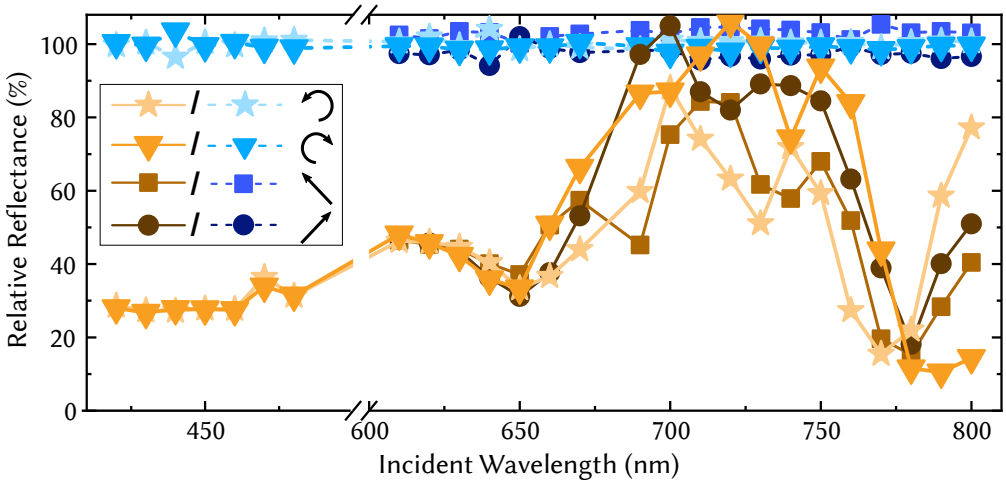

Figure 5.4: Wavelength and Polarization Selective Reflection at the z-Metasurface. The relative reflectance was determined as the integrated response with respect to the polarization averaged values of the planar a-Si reference surface for both, the z-metasurface (orange symbols) and the reference surface (blue symbols).

(details see Subsection 3.4.2). These values are presented as relative values with respect to the average reflectance obtained at the unstructured surface. Evidently, the polarization impact at the z-metasurface (orange lines) is strongly dependent on the wavelength of the impinging light. While a reduced reflectance is observed throughout the complete tested wavelength range, a significant difference as a function of polarization is absent for wavelengths smaller than 650 nm. On the contrary, a strong modulation with polarization is observed for red light up to wavelengths in the near infrared. This is true for both, linearly polarized and CP light. The dependence on the former matches with well known studies of achiral but anisotropic scatterers. Gold nanorods, for example, have shown a more efficient absorption and scattering behavior when the electric field vector's orientation of a linear polarized light beam was aligned with the structural orientation.[243–245] Similarly, for the current z-metasurface, a reduced reflectance has been observed when the electric field vector was oriented along the axis of the z-metaatom, i.e. when the overlap with the z-metaatom was increased.

In contrast to the linear polarized response, the observed modulation as a function of the light's handedness is unique for the chiral z-metaatoms and thus calls for a detailed analysis in terms of the reflection asymmetry δ_R. It can be directly calculated from the relative reflectance employing Equation 5.1.1. While the absence of any reflectance asymmetry for the planar a-Si reference (Figure 5.5a, blue line) serves as a validation of the experimental conditions, asymmetries up to 80 % can be determined for the z-metasurface (orange line) as an average from three spots randomly chosen on the $40 \times 40\,\mu m^2$ z-metasurface area. Its wavelength dependent modulation is characterized by three negative resonances at 670 nm, 730 nm, and 760 nm, and one positive resonance at 790 nm. This line shape with dominant negative chiral resonances qualitatively agrees with the predicted response from electromagnetic simulations

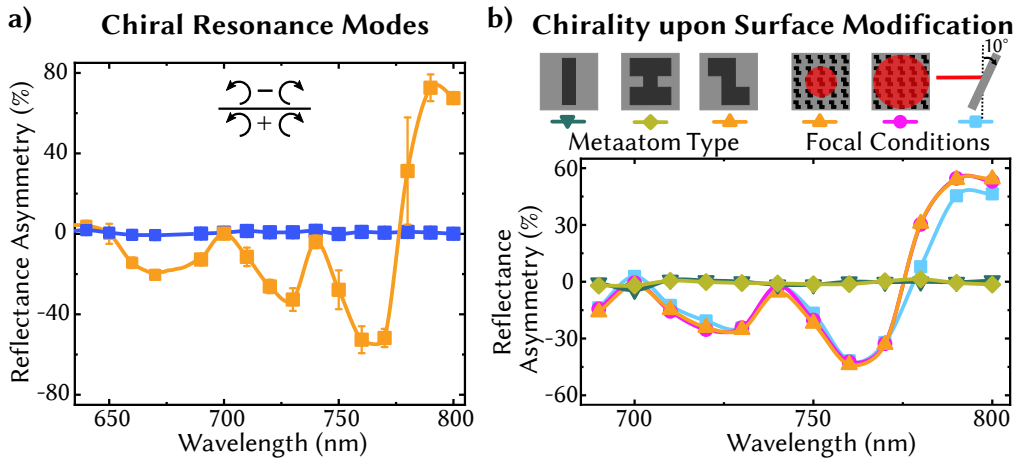

Figure 5.5: Chirality in the Reflection at the z-Metasurface. **a** Reflection asymmetry δ_R on the z-metasurface (orange) and the planar reference surface (blue) with clear chiral resonances only at the z-metasurface. **b** Reflection asymmetry upon variation of the z-metaatom symmetry (bar and double-T structure) and upon variation of the focal conditions, i.e. an increase in spot size by a factor of 5 and a tilt of the z-metasurface by 10° with respect to the optical axis.

(Figure 5.2). The positions, however, are blue shifted by 70 nm with respect to the simulation. Such an offset may be caused by slightly altered actual experimental conditions compared to the properties assumed within the simulation. With the surface being optimized to yield multiple strong resonances within a narrow wavelength range, it is quite sensitive to minor changes of already a few nanometer in its dimensions or shape, such as rounded edges, that cannot be accounted for with such precision in simulations. Additionally, the actual refractive index of a-Si strongly depends on the exact deposition procedure.[246] As such, the reference values employed in the electromagnetic simulation are only an approximation. In fact, the good qualitative agreement in spectral trend is already a reasonable affirmation for interpreting the observed negative chiral resonances in terms of a structure-induced discrimination of left compared to right CP light.
The robustness of these features has been tested for minor modulations in the focal conditions (Figure 5.5b). Neither defocussing the laser beam to yield a spot size of 25 μm^2, nor a moderate tilt of the z-metasurface with respect to the optical axis impacts the observed resonant modes. Finally, the pivotal role of the shape in the appearance of chiral resonances was manifested by a comparison with metasurfaces composed of symmetric metaatoms related to the z-structure (Figure 5.5b). For both, the bar and double-T design introduced in Figure 5.1, the chiral resonant modes are absent. As such, the reduced reflectance with chiral resonances at the z-metasurface can be assigned to the light's interaction at asymmetrically shaped nanoscale metaatoms. Given their spectral appearance between 650 nm and 800 nm, this z-metasurface is perfectly suited to analyze the impact of such a modification on the below band gap excitation and resultant emission of $CsPbBr_3$ QDs.

5.2 Constructing a Hybrid Perovskite-Metasurface

With a substrate set to analyze the impact of a physical modification in the surrounding of $CsPbBr_3$ QDs on their optical transitions, a suitable QD sample has been brought in contact with the surface. The formation of such a hybrid perovskite-metasurface is schematically shown in Figure 5.6. To assign modifications in the $CsPbBr_3$ QD emission to the surface related impact, an interaction between these QDs and the metasurface in the near-field regime

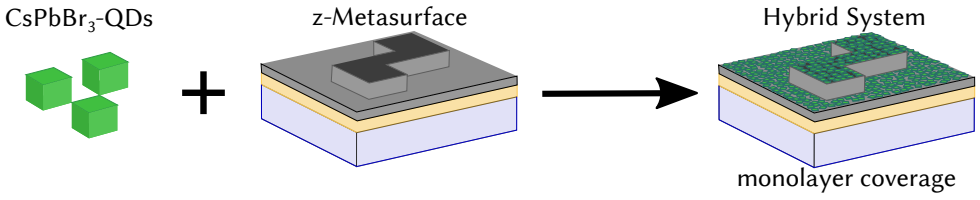

Figure 5.6: Sketch of the Formation of a Hybrid Perovskite Metasurface. Cubic perovskite QDs shall be combined with the z-metasurface to form a hybrid system characterized by a dense monolayer coverage both on and around the z-metaatom.

had to be established. Thus, the thickness of the LHP QD layer in the hybrid system had to be precisely controlled. Ideally, it is kept as thin as possible, i.e. reduced to a monolayer coverage. Furthermore, only formation of a dense film allows to reliably place LHP QDs at the regions of modified optical response. This includes the top of the z-metaatom, which was identified as a region of strong modulation (see Figure 5.2). In this regard, cubic $CsPbBr_3$ QDs capped with oleylamine/oleic acid as described in Section 3.1 are suited to construct such a hybrid perovskite-metasurface. Unlike the previously employed spheroidal lecithin capped $CsPbBr_3$ QDs, these cubic QDs are known to form densely packed ensembles.[76] Thus, I synthesized such cubic $CsPbBr_3$ QDs with their optical properties and assembly-formation ability demonstrated in Figure 5.7.

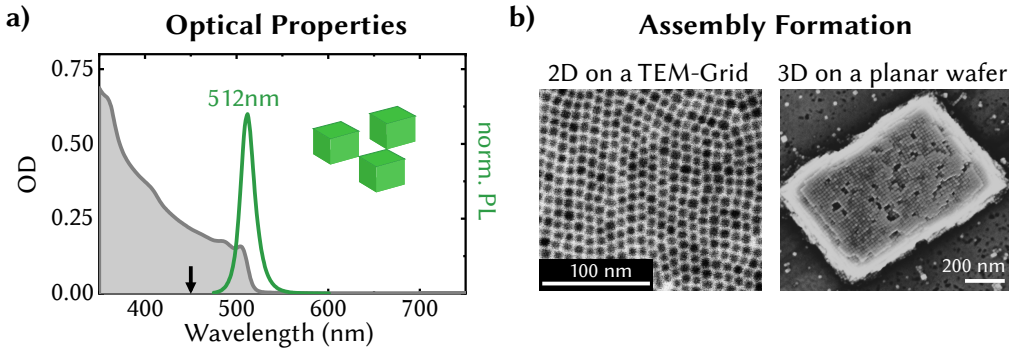

Figure 5.7: Cubic Perovskite QDs for Layer Formation. **a** Absorbance (grey line) and photoluminescence (green line) upon excitation at 450 nm for cubic perovskite QDs of 8 nm edge length. **b** Formation of assemblies of these cubic QDs on a TEM grid (2D), revealing their monodispersity, or as a supercrystal of $500 \times 800\,nm^2$ on a planar Si wafer (3D), illustrating their cubic shape and affinity to form dense packings. Both images were acquired with an SEM, operated in T-SEM mode for an investigation of TEM-grid deposited samples.

The QD's absorbance is characterized by a steep absorption onset at approximately 530 nm. Weak signs of quantum confinement can be observed, though less defined compared to the well separated excitonic transitions of spheroidal QDs (see Figure 4.1). Still, the QDs are characterized by a narrow size distribution as evident from their emission signals centered at 512 nm. An average edge length of 8 nm has been determined from T-SEM images, which show their cubic shape and affinity to form a tightly packed 2D-layer. These two aspects are also very obvious by the QDs ability to self assemble into an unequivocally 3D cubic-shaped supercrystal when I dropcasted them from a hexane solution on a planar silicon wafer followed by a controlled slow evaporation procedure (Figure 5.7b).

While such supercrystals are certainly interesting and an active research field on their own,[247,248] their formation is undesired in the realm of forming a dense and thin coverage on the entire substrate. Thus, I have optimized the deposition technique and sample properties to achieve the desired monolayer coverage. This optimization procedure, based on representative SEM images for each of its crucial parameters of influence, is illustrated in Figure 5.8.

With spin-coating, a different deposition technique has been employed. The substrate is fixed to a rotating plate, causing a droplet of LHP QD solution to be spread by the acting shear forces. A majority of the applied solution is ejected from the substrate in this process while QDs are deposited by evaporation of the solvent from the remaining thin layer.[249] Although high concentrations deem necessary to cover the loss of a huge part of the QD solution, the process is highly reproducible. Similar to spin coating of polymer films,[250] it thus allows a precise thickness control dependent on the chosen conditions. As such, it is advantageous especially for corrugated surfaces compared to dropcasting which refrains from rotating the substrate. Although sample losses are thereby avoided, a deposition of thin layers requires advanced sample engineering,[251] while still lacking a complete substrate coverage. On the contrary, by spin-coating the entire substrate was covered at once.
The deposition procedure has been optimized on a flat silicon surface first (steps (i) to (iv)) and ultimately refined to achieve a good coverage on the corrugated metasurface (steps (v) to (vi)). Firstly, the solvent has been exchanged from hexane (i) to octane (ii). This choice of a solvent with higher boiling assured a slow evaporation, allowing for a sufficient mobility of the QDs prior to depositing the then arranged layer. Thereby, island formation was avoided. In a second step, the concentration has been reduced (iii), which is a detrimental parameter for thickness control.[252] As evident from the uniform SE2-electron contrast, a monolayer has thereby been achieved, though featuring non-covered surface regions. These could be avoided by reducing the speed of rotation (iv) in a next optimization step. With a monolayer coverage on a flat substrate achieved, these conditions have been tested for spin-coating on

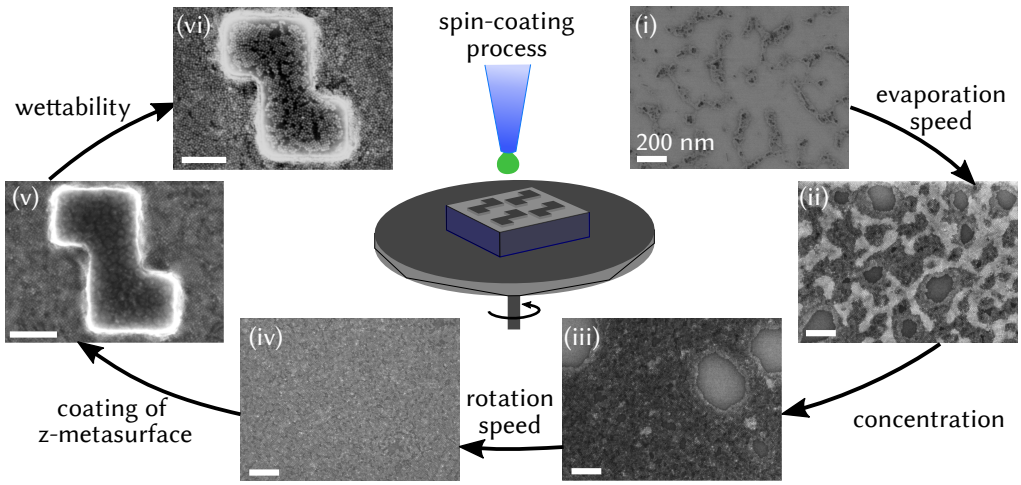

Figure 5.8: Formation of a Monolayer Coverage. In the spin-coating procedure, the z-metasurface is placed on a rotating plate while a small aliquot of green-colored perovskite QD solution is dropped on top. Representative SEM images taken during optimization of the coating procedure: (i-iv) deposition on a planar a-Si substrate from (i) hexane solution, 3.2 g L^{-1}, 2000 rpm; (ii) octane solution, 6.8 g L^{-1}, 2000 rpm; (iii) octane solution, 3.8 g L^{-1}, 2000 rpm; (iv) octane solution, 3.8 g L^{-1}, 1250 rpm. (v-vi) deposition on the z-metasurface from (v) octane solution, 3.8 g L^{-1}, 1250 rpm; (vi) toluene solution, 3.8 g L^{-1}, 1250 rpm.

the z-metasurface (v). Although a monolayer seems to be successfully formed at a first glance, a closer inspection reveals that the z-metaatoms are left out. No QDs are deposited on top of these a-Si pillars. However, having identified these z-metaatom regions as part of the metasurface offering a specifically large discrimination in the electric field distribution (Figure 5.2a), a deposition on top of the z-metaatoms is highly desirable. Thus, further adjustment in the solvent has been pursued as a measure to manipulate the wetting of the substrate (vi). This is a delicate process: On the one hand, the interaction between surface and QDs has to be favored over an interaction between different QDs for an efficient cover formation. However, a too good wetting of the substrate apparently has led the liquid to flow to the geographically lowest point, i.e. causing QDs to be deposited only between the z-metaatom pillars. Testing different solvents with boiling points comparable to octane, I was able to achieve a homogeneous monolayer formation, both on top and in between the z-metaatoms using toluene (vi). A possible explanation might be the slightly larger surface tension of toluene compared to octane.[253] Generally, silicon surfaces are reported to be lyophilic[254] with an increase in contact angle and thus reduced wetting for solvents featuring larger surface tension. Therefore, the slight increase in surface tension might be sufficient to prevent the solvent from accumulating only between the metaatoms and thus also enable a deposition of QDs on top of the metaatoms.

Overall, a facile solution based process was developed that enables the deposition of perovskite QDs as a dense monolayer on an a-Si metasurface. Briefly, in the finalized procedure, 20 µL of a $CsPbBr_3$ solution with a concentration of $3.8\,g\,L^{-1}$ as determined from the absorbance (see Section 3.4 for details) was spread via spin-coating (Laurell, *Model WS-650MZ-23MPP*) at 1250 rpm on a $1 \times 1\,cm^2$ a-Si substrate with an encoded z-metasurface region. Prior to this deposition, the a-Si substrate had been cleaned by ultra-sonication in water, isopropanol, and finally toluene followed by spin-coating of 20 µL pure toluene at equal conditions as used in the subsequent deposition process.

5.3 Excitation Control of the Perovskite-Metasurface PL

The as-prepared hybrid perovskite-metasurface was intensively analyzed regarding its optical properties. LHP QDs are excellent emitters, possessing high PLQYs as discussed in Section 2.1. Thus, their luminescence is representative for any changes in both, excitation and emission processes. Taking additionally the non-transparent nature of the z-metasurface into account, I thus based my investigation of changes in the hybrid perovskite-metasurface performance on luminescent intensity measurements. These are subsequently presented and analyzed to determine the impact of a physical modification in the LHP QDs' surrounding.

5.3.1 The Metasurface Enhances the QD Luminescence

The hybrid perovskite-metasurface has been subject to below and above band gap excitation. An analysis of the LHP QD's luminescence for these two regimes shall enable a comprehensive understanding of the z-metasurface impact both, upon excitation within and outside the wavelength range of polarization dependent resonances (see Figure 5.4). The respective excitation processes and subsequent emission of a photon are exemplary sketched in Figure 5.9, with at least two photons absorbed for a below band gap excitation process. Comparative images of the luminescence detected for an excitation with left CP light on the z-metasurface and an unstructured reference area are depicted in Figure 5.9a.
Notably, the luminescence is strongly enhanced for the z-metasurface region. This enhancement is observed throughout the complete metasurface structure, as evident in the large-scale image kindly taken by S. Pritzl at an inverted microscope (Olympus IX81) upon excitation with light of 470–490 nm. Spatially resolved images that I recorded at the μ-PL setup confirm this observation for both, above and below band gap excitation at 480 nm and 760 nm, respectively. However, independent of the strong enhancement, the PL of the QDs still exhibits the same spectral shape (Figure 5.9b) with the luminescence maximum centered at 512 nm. This suggests that preparation related differences of QDs placed on the corrugated versus the flat substrate areas can be excluded. Omitting such preparation effects was the goal of constructing the substrate to include structured and non-structured areas, allowing a direct comparison between these areas subject to the same spin-coating process. Thus, the enhance-

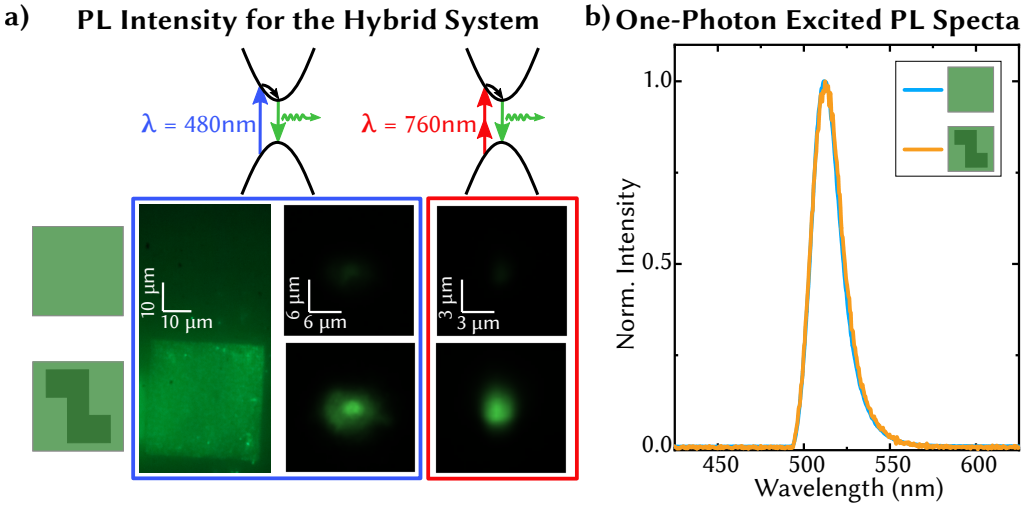

Figure 5.9: PL Characteristics of the Hybrid System. a Below and above band gap excitation are schematically sketched. For both, PL images have been acquired in two distinct regions, at the z-metasurface or an unstructured a-Si reference area located on the same substrate. The additional large scale image for the above band gap excitation reveals the homogeneity of the PL enhancement throughout the complete z-metasurface. **b** Normalized PL spectra upon excitation at 480 nm within the two distinct substrate regions with a maxmimum PL centered at 512 nm.

ment is evidently an effect of the optical surrounding provided by the structured surface area. Yet, a closer analysis is necessary to unravel its reason.

Metasurfaces are known for their ability to modulate both, the excitation and emission process of emitters brought in contact with them. While the probability of absorption changes with the local electric field, the non-isotropic environment may also impact the emission, as quantified in terms of the Purcell effect (see Subsection 2.3.2). To pinpoint the z-metasurface's impact, I analyzed the luminescence signal as a function of the wavelength and polarization of the excitation light. PL images have been spatially integrated both, for measurements taken at the z-metasurface and at the unstructured surface area. In order to allow for a wavelength dependent comparison, average values obtained for each wavelength at the unstructured surface area were set to one and all other values corrected accordingly. The as obtained PLE spectra of the perovskite QDs' enhancement at the z-metasurface are shown in Figure 5.10. A strong enhancement is evident both, upon above and below band gap excitation. When subject to a one-photon process, the luminescence gets enhanced by a factor of six to eight with a slight increase towards shorter excitation wavelengths. Importantly, this was observed independent of the excitation light's polarization. On the contrary, a strong modulation for a variation of both, the polarization and wavelength of the excitation light, is found for a below band gap excitation. For light between 690 nm to 800 nm, the luminescence enhancement at the z-metasurface varies dependent on the wavelength from six up to values as large as 32. At a fixed wavelength, an additionally polarization dependent modulation of a factor up to 20 occurs. Such a strong dependence on the excitation conditions, both wavelength and polarization, is a hint that the observed enhancement is at least partially

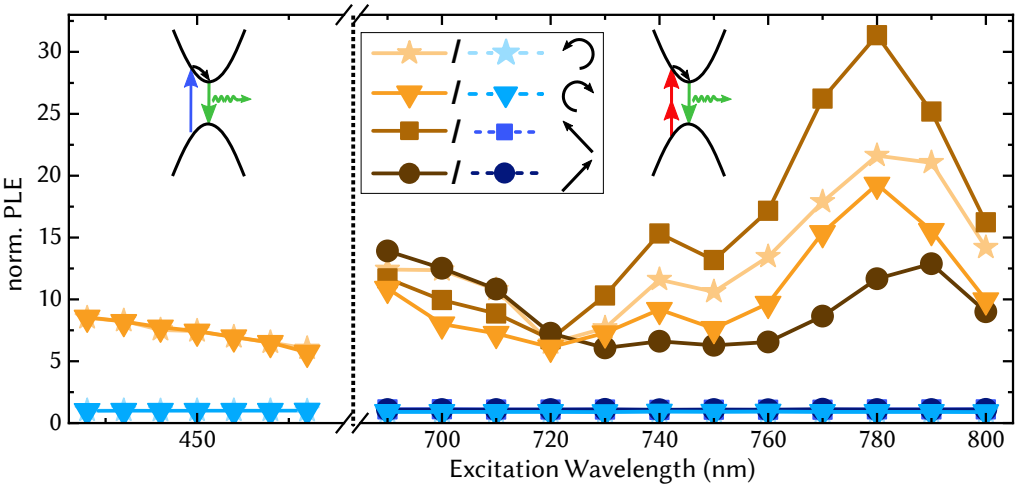

Figure 5.10: Excitation-dependent PL of the Hybrid System. PL intensites obtained via image integration for an excitation with light of variable wavelength and polarization for QDs deposited on the z-metasurface (orange symbols) were normalized to the polarization averaged intensity detected for QDs deposited on an unstructured reference area (blue symbols).

linked to a modification in the excitation process. However, as enhancement was present for all tested conditions, I systematically evaluated the light generation process regarding potential contributions to this enhancement.

5.3.2 The Unaltered Process of Light Generation

The substrate's impact on the emission process is best monitored by means of the QDs' excited state dynamics, which responds sensitively to any changes in the relaxation process. To simplify the analysis, the QDs were excited with light of 440 nm well outside the range of polarization dependent modulations. Time-resolved PL spectra recorded at the PL maximum (Figure 5.11) reveal a multi-exponential PL decay for the same $CsPbBr_3$ QDs dispersed in solution. This might be a hint for the presence of trap-related recombination,[7,26] in line with their lower PLQY of only ≈ 50 % compared to almost 70 % for the highly luminescent spheroidal QDs discussed in Chapter 4. However, a closer analysis of these trap states was omitted at this point, as the properties in solution merely served as a reference in identifying the substrate's impact.

When depositing the QDs, a clear change in the decay behavior is evident. Compared to QDs in solution, the lifetime is shortened. Apparently, additional decay channels, either non-radiative or radiative, are present that speed up the recombination. However, only slight differences in the decay of QDs deposited at the z-metasurface or a planar a-Si area were observed. Instead of a decrease in lifetime, a logarithmic representation even reveals a slightly prolonged decay for the z-metasurface. If a change in the photon density of states (i.e. modes the photon emits into) was to play a significant role in luminescence enhancement at the

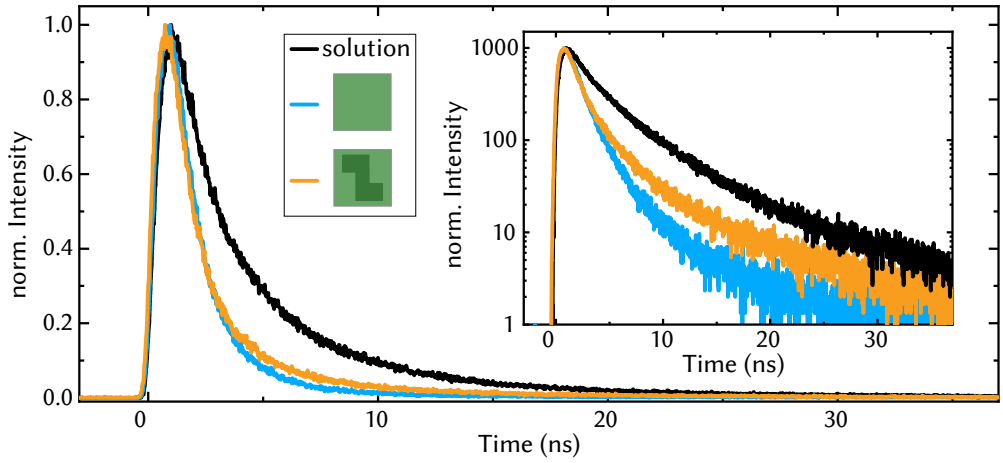

Figure 5.11: Time-resolved PL of the Hybrid System. PL recombination dynamics were recorded by TCSPC at the PL maximum (512 nm) upon excitation at 480 nm. Apart from QD monolayers formed at (orange) and next to (blue) the structured z-metasurface area, the luminescence of QDs dispersed in toluene (black) was probed. The inset shows the same dataset with a logarithmic scale.

z-metasurface, the lifetime of the excited state would, on the contrary, be reduced. Thus, the increase in luminescence for QDs on the z-metasurface cannot be explained by a coupling of emitted photon to a larger number of optical modes. In other words, the emission process is not significantly impacted by the z-metasurface. Changes in the luminescence are instead mostly related to the excitation process!

In this process, the z-metaatoms might act as nanoscale scatterers and thereby confine the excitation light to certain regions. LHP QDs placed close to such a confinement region are subject to an enhanced electric field energy density. As an aftereffect, these QDs absorb more light and consequently the average emission at such a surface area is enhanced. This interpretation is strongly supported by the fact that the enhanced emission goes hand-in-hand with a reduced reflection at the z-metasurface, as discussed in Section 5.1. Conversely, the enhancement suggests that the reduced reflectance is a consequence of scattering. Upon one-photon excitation, for example, the reflectance slightly decreases towards shorter wavelengths (Figure 5.4), while the luminescence is enhanced fo an identical spectral variation (Figure 5.10). A similar trend is observed within the wavelength range of below band gap excitation. However, multiple photons are involved in the generation of the excited state for a below band gap excitation. Thus, care needs to be taken when linking the strong polarization and wavelength dependent modulations in the PL intensity exclusively to the z-metasurface light confinement ability. Wavelength dependent luminescence modulations may also result from an alteration of the non-linear process involved. This has previously been reported for dense packed LHP QD films.[76] I have thus conducted power dependent measurements to clarify the order of the process for the various excitation conditions for the present hybrid perovskite-metasurface system.

The result of these power dependent measurements are shown in Figure 5.12. Pump fluences have been determined based on the excitation light's power, measured at the sample location, and the illuminated area. The spot size encompassing all pixels with more than 20 % of the maximum intensity has been taken as a measure for this area. The quadratic relation between emitted light intensity and excitation pump fluence in Figure 5.12a is characteristic for a two-photon process (see Subsection 2.1.3), in which two excitation light quanta are simultaneously absorbed to reach the excited state. For this spot located at the z-metasurface, such a two-photon process was found upon excitation with left and right CP light, though the luminescence enhancement for these two polarization states differs. An order of two is also maintained independent of the excitation wavelength or its polarization state within the tested wavelength range from 690 nm up to 800 nm (Figure 5.12b). Most importantly, within the accuracy of the measurement, the order of the process is also independent on whether or not the z-metasurface is present. The small deviation with slightly smaller values determined for the reference a-Si surface area might be explained by the different intensity range of detection allowing to achieve a higher signal-to-noise ratio at the z-metasurface area.

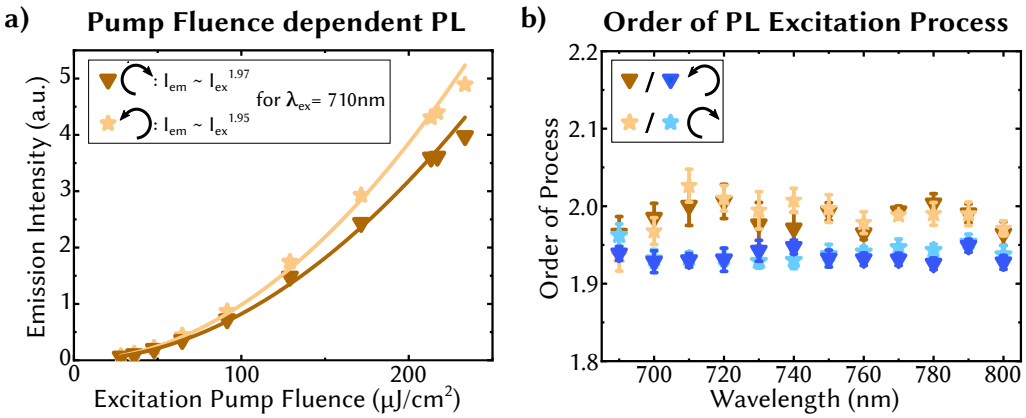

Figure 5.12: The Two-Photon Excitation Process. a Emission intensities measured when exciting QDs deposited on the z-metasurface with light of 710 nm for various excitation pump fluences. The solid lines represent power-law fits to the data. Their functional dependence is stated with the exponent being the order of the process. **b** Spectral dependence of the order of the process extracted from quadratic fits to the power dependent luminescence of QDs deposited on the z-metasurface (orange symbols) or on a planar a-Si substrate area (blue symbols) upon variation of the excitation light's handedness and wavelength.

In summary, the process of light generation apparently remains unaltered by the presence of the z-metasurface versus depositing the QD monolayer on an unstructured a-Si layer instead. The previous statement can thus be further refined: Changes in the luminescence are attributed to an alteration in the QD's absorption probability. This is true both, upon above and below band gap excitation. A two-photon excitation with its dependence on the electric field vector to the power of four reacts especially sensitive to such changes. In this regard, the z-metasurface allows to directly steer the absorption probability by its ability to confine excitation light of given properties via scattering.

5.3.3 Chirality is Imprinted on the Two-Photon Excitation

With this in mind, the impact exhibited by the surrounding on a QDs' luminescence, specifically its significance for a polarization dependent response of the QDs, shall finally be explicated. Strong modulations in luminescence as a function of polarization, evident e.g. in Figure 5.10, can now be analyzed in the realm of light confinement provided by the z-metasurface. At first, the discrepancy in luminescence for an excitation with linearly polarized light shall be shortly discussed. When its orientation has been aligned with the direction of the z-structure the enhancement peaked, while the weakest enhancements have been observed when the excitation light's electric field vector is rotated by 90° with respect to the z-metaatom orientation. A correlation with the inverse trend observed for the reflection is apparent, supporting the notion that light not reflected is scattered at the surface to light confinement regions thus contributing to an enhanced emission signal. As I pointed out previously, the increased scattering ability when the electric field vector is aligned with the

long axis of the structure is in line with similar observations for anisotropic but achiral gold nanoantenna structures.[245]

A significant change in luminescence is not only observed for different orientations of linearly polarized light, but most importantly also upon alteration of the light's handedness. This is a unique feature for the asymmetrically shaped z-metaatom. Knowing that changes in the luminescence in Figure 5.10 are directly related to a modulation of the QDs' absorption probability, the z-metasurface impact on the absorption of circularly polarized light can be extracted. For this, the two-photon excitation induced PL asymmetry δ_{PL} as a function of the excitation wavelength λ has been defined in an analogous manner as the reflection asymmetry by

$$\delta_{\mathrm{PL}}(\lambda) = \frac{I(\mathrm{LCP},\lambda) - I(\mathrm{RCP},\lambda)}{I(\mathrm{LCP},\lambda) + I(\mathrm{RCP},\lambda)}. \tag{5.2}$$

This is essentially a measure for the structure induced circular dichroism. Note that this definition differs however by a factor of 1/2 from the dissymmetry factor g commonly applied to compare chiral discrimination for molecular systems. Yet, the beauty of the herein defined PL asymmetry δ_{PL} is its link to the percentage scale. An asymmetry of +100 % (−100 %) directly relates to an absorption of purely left (right) CP light.

The as determined PL asymmetry δ_{PL} in Figure 5.13a clearly reveals wavelength dependent modulations with a chiral discrimination as large as 25 %. This modulation can be seen as a consequence of the asymmetric structure at the z-metasurface, with insignificant chiral effect for QDs deposited on a planar a-Si surface area. The positive sign of the two chiral resonances

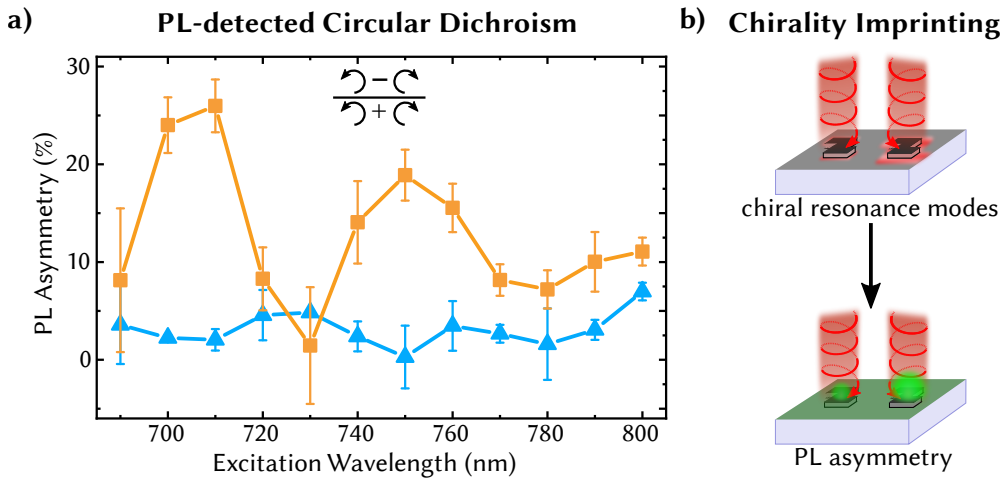

Figure 5.13: PL-detected Circular Dichroism of the Hybrid System. a Two-photon detected PL asymmetry as calculated based on intensity data exemplary presented in Figure 5.10 according to Equation 5.3.3 for QDs located on the z-metasurface (orange symbols) and on a planar a-Si reference area (blue symbols). Error bars account for averaging the response obtained at five different spots across the z-metasurface. **b** Sketch how polarization dependent light confinement at the z-metaatoms acting as nanoantennas sensitizes the two-photon absorption of QDs deposited on the structure.

at 710 nm and 750 nm implies that an excitation with left CP light is more efficient. Notably, their appearance coincides with negative chiral resonances in reflectance asymmetry, taking a redshift of 30 nm (for the PL resonances) into account. Such a shift in wavelength may be explained by a refractive index change induced by the deposition of LHP material in the near field. Compared to air, $CsPbBr_3$ possesses a larger refractive index of $n_{700\,nm} \approx 2.2$,[255] such that a redshifted resonance would be expected.[138]

Overall, the similar but inverse line shape in the excitation light's reflection and the QDs' emission intensity thus suggests that the z-metasurface directly imprints its chiral effect on the two-photon excitation of the LHP QDs, as sketched in Figure 5.13b. The structure induced asymmetric light-matter interactions allow to confine light of particular handedness – here left CP light – to a larger extent, which subsequently enhances the absorption of LHP QDs located in the near-field of the z-metasurface. In this regard, the QD luminescence is a valuable tool for probing such changes in its surrounding and thereby identifying the unique chiral near field of the chosen asymmetric z-metaatom. Likewise, this proof of concept demonstrates that such hybrid perovskite-metasurface systems formed in a facile solution based process offer the possibility to induce circular dichorism in LHP QDs. Notably, discrimination of the light's handedness to much larger extents than thus far possible via chiral surfactants[256,257] can be achieved, which is a step towards their utilization for advanced applications such as circular polarized light photodetectors.

6

Conclusions and Outlook

This thesis seeks to generate an insight on important interaction mechanisms QDs are exposed to through their environment. Specifically, changes in the optical transitions in $CsPbBr_3$ QDs upon chemical and physical modifications to their surrounding have been elucidated. Firstly, I analyzed the interaction between QDs and metal salts in solution. Among post-synthetic modification processes, such treatments take a prominent role. Yet, a microscopic picture that enables to address fundamental process parameters had been lacking. In a second approach, I demonstrated how near field interactions at substrates may be exploited to equip QDs with optical properties not inherent to their material class. Such an intimate contact with a substrate is present for many applications including photodetectors, LEDs, or alike. Thus, control of the substrate's impact is a viable method to achieve novel functionalities. In the following, I will summarize the main findings in more detail.

On the one hand, I was able to propose a model for the metal salt-QD interaction mechanism by combining highly monodisperse, excitonic spheroidal $CsPbBr_3$ QDs with $BiBr_3$. When adding $BiBr_3$ to the QDs, strong, instantaneous but reversible quenching occurred, pointing towards a surface-driven process. Closely analyzing selected QD samples with different $BiBr_3$ contents allowed to conclude on a fast, but inhomogeneous trap formation. This result might help to further pin down the role Bi adopts as a dopant, which had been subject to debate thus far.
Notably, stepwise $BiBr_3$ addition revealed an unusual exponential dependence between PL intensity and quencher concentration. I could explain this with a statistic adsorption process. The presented statistic model, the sphere of action model, in particular enabled me to identify

the severity of formed trap states, exposing a non-radiative decay time of less than 10 ps. Opposed to the common perception of LHP as defect tolerant, such deep traps formed by $BiBr_3$ result in a single adsorbed species and thus only one trap capable of completely quenching the PL of a QD. This suggests that impurities in LHP have to be carefully traced despite LHP's tolerance to intrinsic defects.
With a surface affinity factor, I furthermore introduced a novel interpretation of the exponential quenching parameter in the sphere of action model matching the situation of trap formation at the QDs. Tailored modifications of the QDs subsequently enabled me to extract key process parameters such as the adsorption site or barrier imposed by ligands, utilizing dependencies of the aforementioned affinity factor. Size dependent studies unraveled a clear preference of adsorption at facet junctions, while surface ligand variation revealed that a Langmuir-type monolayer coverage impedes adsorption. Now that a framework for the interaction is at hand, future studies such as halide alteration of the QD and closer analysis of interaction with different metal salts may provide further inisght on the impact of defects in LHP QDs.

As an example of utilizing physical modifications, strong chiral discrimination in the absorption of intrinsically achiral LHP QDs has been demonstrated with the help of a metasurface. While previous approaches mainly focused on manipulating luminescence and relied on bulk LHP films, I instead addressed the absorption process in a monolayer of QDs. The choice of QDs increased processing flexibility, while control of the absorption may allow for e.g. chiral LHP light sensors.
With a z-shaped metasurface composed of amorphous silicon, a rational design has been introduced compatible with semiconductor processing technologies. Complex polarization and wavelength dependent light-matter interactions were shown to occur at this metasurface. Specifically, I found a strong discrimination of left and right circularly polarized light within the red spectral range. Therefore, I subsequently utilized this surface in a hybrid perovskite-metasurface system for inducing changes in the nonlinear excitation process of $CsPbBr_3$ QDs. Such a hybrid system could be formed by depositing cubic $CsPbBr_3$ QDs with precise thickness control down to a monolayer coverage on the metasurface by an easy solution based method. This ensured a contact exclusively in the near-field.
Based on analyzing the PL characteristics for QDs in contact with the metasurface, I demonstrated how scattering induced light confinement within the structure exclusively translated to an enhanced absorption. A significant increase in PL intensity upon above and below band gap excitation has been achieved in the hybrid system. For the below band gap excitation, additionally a wavelength dependent polarization sensitivity up to 25 % was obtained. On the one hand, I confirmed that the light generation process remained identical, i.e. a two-photon absorption occurred regardless of the excitation condition and importantly the luminescence process was not impacted. On the other hand, I could demonstrate that the PL increase was

directly related to the light scattering ability of the surface. As such, the presented results are a demonstration of polarization dependent absorption control, i.e. evolution of circular dichroism, in $CsPbBr_3$ QDs caused by the surface's chiral near-field.

Overall, the results presented in this thesis add to the understanding of interactions between QDs and their environment. In particular, they contribute to seeking control of these interactions to enable designed QD properties. The proposed model for the metal salt-QD interaction created a perspective for future surface alterations and may additionally aid in disentangling why certain metal salts cause a loss in luminescence while others do not. In the future, this may allow to avoid defects and thus lead to more efficient light sources. The demonstrated combination of QDs with a chiral metasurface by a facile solution based process may on the other hand facilitate the realization of chiral sensors that utilize LHPs. As such, these results may help to further establish LHP QDs as an exciting and prospective material for future semiconductor applications.

References

[1] Thomas Kirchartz and Uwe Rau. "What Makes a Good Solar Cell?" In: *Adv. Energy Mater.* 8.28 (2018), p. 1703385. DOI: https://doi.org/10.1002/aenm.201703385 (cited on page 1).

[2] K. L. Chopra, P. D. Paulson, and V. Dutta. "Thin-film solar cells: an overview." In: *Prog. Photovoltaics Res. Appl.* 12.2-3 (2004), pp. 69–92. DOI: https://doi.org/10.1002/pip.541 (cited on page 1).

[3] Shuji Nakamura, Takashi Mukai, and Masayuki Senoh. "Candela-class high-brightness InGaN/AlGaN double-heterostructure blue-light-emitting diodes." In: *Appl. Phys. Lett.* 64.13 (1994), pp. 1687–1689. DOI: 10.1063/1.111832 (cited on page 1).

[4] Shuji Nakamura and Gerhard Fasol. "Introduction." In: *The Blue Laser Diode: GaN Based Light Emitters and Lasers*. Berlin, Heidelberg: Springer Berlin Heidelberg, 1997, pp. 1–5. DOI: 10.1007/978-3-662-03462-0_1 (cited on page 1).

[5] Marshall I. Nathan, William P. Dumke, Gerald Burns, Jr. Dill Frederick H., and Gordon Lasher. "Stimulated Emission of Radiation from GaAs p-n Junctions." In: *Appl. Phys. Lett.* 1.3 (2004), pp. 62–64. DOI: 10.1063/1.1777371 (cited on page 1).

[6] Michał Michalik, Jacek Szymańczyk, Michał Stajnke, Tomasz Ochrymiuk, and Adam Cenian. "Medical Applications of Diode Lasers: Pulsed versus Continuous Wave (cw) Regime." In: *Micromachines* 12.6 (2021). DOI: 10.3390/mi12060710 (cited on page 1).

[7] Laura M. Herz. "Charge-Carrier Dynamics in Organic-Inorganic Metal Halide Perovskites." In: *Annu. Rev. Phys. Chem.* 67.1 (2016), pp. 65–89. DOI: 10.1146/annurev-physchem-040215-112222 (cited on pages 1, 9, 10, 98).

[8] Oxford PV. *Oxford PV The Perovskite Company*. https://www.oxfordpv.com/news/oxford-pv-sets-new-solar-cell-world-record. Accessed: 10th October, 2023. 2023 (cited on page 1).

[9] Felix Deschler, Michael Price, Sandeep Pathak, Lina E. Klintberg, David-Dominik Jarausch, Ruben Higler, Sven Hüttner, Tomas Leijtens, Samuel D. Stranks, Henry J. Snaith, Mete Atatüre, Richard T. Phillips, and Richard H. Friend. "High Photoluminescence Efficiency and Optically Pumped Lasing in Solution-Processed Mixed Halide Perovskite Semiconductors." In: *J. Phys. Chem. Lett.* 5.8 (2014), pp. 1421–1426. DOI: 10.1021/jz5005285 (cited on page 1).

[10] Guichuan Xing, Nripan Mathews, Swee Sien Lim, Natalia Yantara, Xinfeng Liu, Dharani Sabba, Michael Grätzel, Subodh Mhaisalkar, and Tze Chien Sum. "Low-temperature solution-processed wavelength-tunable perovskites for lasing." In: *Nat. Mater.* 13.5 (2014), pp. 476–480. DOI: 10.1038/nmat3911 (cited on page 1).

[11] M. Era, S. Morimoto, T. Tsutsui, and S. Saito. "Organic-inorganic heterostructure electroluminescent device using a layered perovskite semiconductor $(C_6H_5C_2H_4NH_3)_2PbI_4$." In: *Appl. Phys. Lett.* 65.6 (1994), pp. 676–678. DOI: 10.1063/1.112265 (cited on page 1).

[12] Li Na Quan, Barry P. Rand, Richard H. Friend, Subodh Gautam Mhaisalkar, Tae-Woo Lee, and Edward H. Sargent. "Perovskites for Next-Generation Optical Sources." In: *Chem. Rev.* 119.12 (2019), pp. 7444–7477. DOI: 10.1021/acs.chemrev.9b00107 (cited on pages 1, 9, 14).

[13] Maksym V. Kovalenko, Loredana Protesescu, and Maryna I. Bodnarchuk. "Properties and potential optoelectronic applications of lead halide perovskite nanocrystals." In: *Science* 358.6364 (2017), pp. 745–750. DOI: 10.1126/science.aam7093 (cited on pages 1, 2, 9, 10, 14, 18).

[14] F. Pelayo García de Arquer, Dmitri V. Talapin, Victor I. Klimov, Yasuhiko Arakawa, Manfred Bayer, and Edward H. Sargent. "Semiconductor quantum dots: Technological progress and future challenges." In: *Science* 373.6555 (2021), eaaz8541. DOI: 10.1126/science.aaz8541 (cited on pages 1, 8, 14, 15).

[15] M G Bawendi, M L Steigerwald, and L E Brus. "The Quantum Mechanics of Larger Semiconductor Clusters (Quantum Dots)." In: *Annu. Rev. Phys. Chem.* 41.1 (1990), pp. 477–496. DOI: 10.1146/annurev.pc.41.100190.002401 (cited on page 1).

[16] C. B. Murray, D. J. Norris, and M. G. Bawendi. "Synthesis and characterization of nearly monodisperse CdE (E = sulfur, selenium, tellurium) semiconductor nanocrystallites." In: *J. Am. Chem. Soc.* 115.19 (1993), pp. 8706–8715. DOI: 10.1021/ja00072a025 (cited on pages 2, 41).

[17] A A H Abdellatif, M A Younis, M Alsharidah, O Al Rugaie, and Tawfeek H M. "Biomedical Applications of Quantum Dots: Overview, Challenges, and Clinical Potential." In: *Int J Nanomed.* 17 (2022), pp. 1951–1970. DOI: 10.2147/IJN.S357980 (cited on page 2).

[18] Yasuhiro Shirasaki, Geoffrey J. Supran, Moungi G. Bawendi, and Vladimir Bulović. "Emergence of colloidal quantum-dot light-emitting technologies." In: *Nat. Photonics* 7.1 (2013), pp. 13–23. DOI: 10.1038/nphoton.2012.328 (cited on page 2).

[19] Michael A. Boles, Daishun Ling, Taeghwan Hyeon, and Dmitri V. Talapin. "The surface science of nanocrystals." In: *Nat. Mater.* 15.2 (2016), pp. 141–153. DOI: 10.1038/nmat4526 (cited on pages 2, 8, 15).

[20] Philip D. Howes, Rona Chandrawati, and Molly M. Stevens. "Colloidal nanoparticles as advanced biological sensors." In: *Science* 346.6205 (2014), p. 1247390. DOI: 10.1126/science.1247390 (cited on page 2).

[21] Niko Hildebrandt, Christopher M. Spillmann, W. Russ Algar, Thomas Pons, Michael H. Stewart, Eunkeu Oh, Kimihiro Susumu, Sebastian A. Díaz, James B. Delehanty, and Igor L. Medintz. "Energy Transfer with Semiconductor Quantum Dot Bioconjugates: A Versatile Platform for Biosensing, Energy Harvesting, and Other Developing Applications." In: *Chem. Rev.* 117.2 (2017), pp. 536–711. DOI: 10.1021/acs.chemrev.6b00030 (cited on pages 2, 15).

[22] Christian M. Wolff, Peter D. Frischmann, Marcus Schulze, Bernhard J. Bohn, Robin Wein, Panajotis Livadas, Michael T. Carlson, Frank Jäckel, Jochen Feldmann, Frank Würthner, and Jacek K. Stolarczyk. "All-in-one visible-light-driven water splitting by combining nanoparticulate and molecular co-catalysts on CdS nanorods." In: *Nat. Energy* 3.10 (2018), pp. 862–869. DOI: 10.1038/s41560-018-0229-6 (cited on page 2).

[23] Tina X. Ding, Jacob H. Olshansky, Stephen R. Leone, and A. Paul Alivisatos. "Efficiency of Hole Transfer from Photoexcited Quantum Dots to Covalently Linked Molecular Species." In: *J. Am. Chem. Soc.* 137.5 (2015), pp. 2021–2029. DOI: 10.1021/ja512278a (cited on pages 2, 15).

[24] Kerim M. Gattás-Asfura and Roger M. Leblanc. "Peptide-coated CdS quantum dots for the optical detection of copper(ii) and silver(i)." In: *Chem. Commun.* (21 2003), pp. 2684–2685. DOI: 10.1039/B308991F (cited on page 2).

[25] Yongfen Chen and Zeev Rosenzweig. "Luminescent CdS Quantum Dots as Selective Ion Probes." In: *Anal. Chem.* 74.19 (2002), pp. 5132–5138. DOI: 10.1021/ac0258251 (cited on page 2).

[26] Bernhard J. Bohn, Yu Tong, Moritz Gramlich, May Ling Lai, Markus Döblinger, Kun Wang, Robert L. Z. Hoye, Peter Müller-Buschbaum, Samuel D. Stranks, Alexander S. Urban, Lakshminarayana Polavarapu, and Jochen Feldmann. "Boosting Tunable Blue Luminescence of Halide Perovskite Nanoplatelets through Postsynthetic Surface Trap Repair." In: *Nano Lett.* 18.8 (2018), pp. 5231–5238. DOI: 10.1021/acs.nanolett.8b02190 (cited on pages 2, 19, 20, 64, 80, 98).

[27] Javad Shamsi, Alexander S. Urban, Muhammad Imran, Luca De Trizio, and Liberato Manna. "Metal Halide Perovskite Nanocrystals: Synthesis, Post-Synthesis Modifications, and Their Optical Properties." In: *Chem. Rev.* 119.5 (2019), pp. 3296–3348. DOI: 10.1021/acs.chemrev.8b00644 (cited on pages 2, 9, 10, 15, 20, 38–41).

[28] Dennis H. Goldstein. *Polarized Light.* 3rd ed. Boca Raton: CRC Press, 2011 (cited on page 2).

[29] Aleksandr Vaskin, Radoslaw Kolkowski, A. Femius Koenderink, and Isabelle Staude. In: *Nanophotonics* 8.7 (2019), pp. 1151–1198. DOI: doi:10.1515/nanoph-2019-0110 (cited on pages 2, 30, 31).

[30] Giorgio Adamo, Harish Natarajan Swaha Krishnamoorthy, Daniele Cortecchia, Bhumika Chaudhary, Venkatram Nalla, Nikolay I. Zheludev, and Cesare Soci. "Metamaterial Enhancement of Metal-Halide Perovskite Luminescence." In: *Nano Lett.* 20.11 (2020), pp. 7906–7911. DOI: 10.1021/acs.nanolett.0c02571 (cited on pages 2, 31).

[31] Chun-Ho Lin, Chieh-Yu Kang, Ting-Zhu Wu, Chun-Lin Tsai, Chin-Wei Sher, Xinwei Guan, Po-Tsung Lee, Tom Wu, Chih-Hsiang Ho, Hao-Chung Kuo, and Jr-Hau He. "Giant Optical Anisotropy of Perovskite Nanowire Array Films." In: *Adv. Funct. Mater.* 30.14 (2020), p. 1909275. DOI: https://doi.org/10.1002/adfm.201909275 (cited on page 2).

[32] In Cheol Seo, Yeonsoo Lim, Soo-Chan An, Byung Hoon Woo, Seongheon Kim, Jung Geon Son, SeokJae Yoo, Q-Han Park, Jin Young Kim, and Young Chul Jun. "Circularly Polarized Emission from Organic–Inorganic Hybrid Perovskites via Chiral Fano Resonances." In: *ACS Nano* 15.8 (2021), pp. 13781–13793. DOI: 10.1021/acsnano.1c05421 (cited on pages 2, 35).

[33] Felix Bloch. "Über die Quantenmechanik der Elektronen in Kristallgittern." In: *Z. Phys.* 52.7 (1929), pp. 555–600. DOI: 10.1007/BF01339455 (cited on page 6).

[34] Mildred Dresselhaus, Gene Dresselhaus, Stephen B. Cronin, and Antonio Gomes Souza Filho. *Solid State Properties: From Bulk to Nano.* Berlin, Heidelberg: Springer Berlin Heidelberg, 2018, pp. 13–104, 411–441. DOI: 10.1007/978-3-662-55922-2 (cited on pages 6, 7, 16, 17).

[35] M. Born and R. Oppenheimer. "Zur Quantentheorie der Molekeln." In: *Ann. Phys.* 389.20 (1927), pp. 457–484. DOI: https://doi.org/10.1002/andp.19273892002 (cited on page 6).

[36] D. R. Hartree. "The Wave Mechanics of an Atom with a Non-Coulomb Central Field. Part II. Some Results and Discussion." In: *Math. Proc. Cambridge Philos. Soc.* 24.1 (1928), pp. 111–132. DOI: 10.1017/S0305004100011920 (cited on page 6).

[37] V. Fock. "Näherungsmethode zur Lösung des quantenmechanischen Mehrkörperproblems." In: *Z. Phys.* 61.1 (1930), pp. 126–148. DOI: 10.1007/BF01340294 (cited on page 6).

[38] Charles Kittel. *Semiconductor Optics.* 8th ed. Danvers: John Wiley & Sons Inc., 2005 (cited on pages 6, 15, 16).

[39] S. V. Gaponenko. *Optical Properties of Semiconductor Nanocrystals.* Cambridge Studies in Modern Optics. Cambridge University Press, 1998, pp. 1–54. DOI: 10.1017/CBO9780511524141 (cited on pages 7, 8, 11).

[40] *Semiconductor Optics.* Berlin, Heidelberg: Springer Berlin Heidelberg, 2007. DOI: 10.1007/978-3-540-38347-5 (cited on pages 7, 9, 15, 47).

[41] J. C. Slater. "Electrons in Perturbed Periodic Lattices." In: *Phys. Rev.* 76 (11 1949), pp. 1592–1601. DOI: 10.1103/PhysRev.76.1592 (cited on page 7).

[42] Gregory H. Wannier. "The Structure of Electronic Excitation Levels in Insulating Crystals." In: *Phys. Rev.* 52 (3 1937), pp. 191–197. DOI: 10.1103/PhysRev.52.191 (cited on page 7).

[43] Makoto Sakata, Takashi Nishiwaki, and Jimpei Harada. "Neutron Diffraction Study of the Structure of Cubic $CsPbBr_3$." In: *J. Phys. Soc. Jpn.* 47.1 (1979), pp. 232–233. DOI: 10.1143/JPSJ.47.232 (cited on page 9).

[44] Shuxia Tao, Ines Schmidt, Geert Brocks, Junke Jiang, Ionut Tranca, Klaus Meerholz, and Selina Olthof. "Absolute energy level positions in tin- and lead-based halide perovskites." In: *Nat. Commun.* 10.1 (2019), p. 2560. DOI: 10.1038/s41467-019-10468-7 (cited on pages 9, 10).

[45] Riley E. Brandt, Vladan Stevanović, David S. Ginley, and Tonio Buonassisi. "Identifying defect-tolerant semiconductors with high minority-carrier lifetimes: beyond hybrid lead halide perovskites." In: *MRS Commun.* 5.2 (2015), pp. 265–275. DOI: 10.1557/mrc.2015.26 (cited on pages 9, 10, 18).

[46] V M Goldschmidt. "Die Gesetze der Krystallochemie." In: *Naturwissenschaften* 14.21 (1926), pp. 477–485. DOI: 10.1007/BF01507527 (cited on page 9).

[47] Tom F. W. Barth. "Die Kristallstruktur von Perowskit und verwandten Verbindungen." In: *Norsk Geolog. Tidsskr. VIII* 08.03 (1925), pp. 201–216 (cited on page 9).

[48] M. A. Peña and J. L. G. Fierro. "Chemical Structures and Performance of Perovskite Oxides." In: *Chem. Rev.* 101.7 (2001), pp. 1981–2018. DOI: 10.1021/cr980129f (cited on page 9).

[49] Gustav Rose. "Beschreibung einiger neuen Mineralien des Urals." In: *Ann. Phys.* 124.12 (1839), pp. 551–573. DOI: https://doi.org/10.1002/andp.18391241205 (cited on page 9).

[50] T. Umebayashi, K. Asai, T. Kondo, and A. Nakao. "Electronic structures of lead iodide based low-dimensional crystals." In: *Phys. Rev. B* 67 (15 2003), p. 155405. DOI: 10.1103/PhysRevB.67.155405 (cited on page 10).

[51] Jingying Wang, Chuang Zhang, Haoliang Liu, Ryan McLaughlin, Yaxin Zhai, Shai R. Vardeny, Xiaojie Liu, Stephen McGill, Dmitry Semenov, Hangwen Guo, Ryuichi Tsuchikawa, Vikram V. Deshpande, Dali Sun, and Z. Valy Vardeny. "Spin-optoelectronic devices based on hybrid organic-inorganic trihalide perovskites." In: *Nat. Commun.* 10.1 (2019), p. 129. DOI: 10.1038/s41467-018-07952-x (cited on page 10).

[52] Simone Strohmair, Amrita Dey, Yu Tong, Lakshminarayana Polavarapu, Bernhard J. Bohn, and Jochen Feldmann. "Spin Polarization Dynamics of Free Charge Carriers in $CsPbI_3$ Nanocrystals." In: *Nano Lett.* 20.7 (2020), pp. 4724–4730. DOI: 10.1021/acs.nanolett.9b05325 (cited on pages 10, 33).

[53] E. Kirstein, N. E. Kopteva, D. R. Yakovlev, E. A. Zhukov, E. V. Kolobkova, M. S. Kuznetsova, V. V. Belykh, I. A. Yugova, M. M. Glazov, M. Bayer, and A. Greilich. "Mode locking of hole spin coherences in CsPb(Cl, Br)3 perovskite nanocrystals." In: *Nat. Commun.* 14.1 (2023), p. 699. DOI: 10.1038/s41467-023-36165-0 (cited on page 10).

[54] Samuel D. Stranks, Giles E. Eperon, Giulia Grancini, Christopher Menelaou, Marcelo J. P. Alcocer, Tomas Leijtens, Laura M. Herz, Annamaria Petrozza, and Henry J. Snaith. "Electron-Hole Diffusion Lengths Exceeding 1 Micrometer in an Organometal Trihalide Perovskite Absorber." In: *Science* 342.6156 (2013), pp. 341–344. DOI: 10.1126/science.1243982 (cited on page 10).

[55] Christian Wehrenfennig, Giles E. Eperon, Michael B. Johnston, Henry J. Snaith, and Laura M. Herz. "High Charge Carrier Mobilities and Lifetimes in Organolead Trihalide Perovskites." In: *Adv. Mater.* 26.10 (2014), pp. 1584–1589. DOI: https://doi.org/10.1002/adma.201305172 (cited on page 10).

[56] Vikash Kumar Ravi, Ganesh B. Markad, and Angshuman Nag. "Band Edge Energies and Excitonic Transition Probabilities of Colloidal $CsPbX_3$ (X = Cl, Br, I) Perovskite Nanocrystals." In: *ACS Energy Lett.* 1.4 (2016), pp. 665–671. DOI: 10.1021/acsenergylett.6b00337 (cited on page 10).

[57] Verena A. Hintermayr, Alexander F. Richter, Florian Ehrat, Markus Döblinger, Willem Vanderlinden, Jasmina A. Sichert, Yu Tong, Lakshminarayana Polavarapu, Jochen Feldmann, and Alexander S. Urban. "Tuning the Optical Properties of Perovskite Nanoplatelets through Composition and Thickness by Ligand-Assisted Exfoliation." In: *Adv. Mater.* 28.43 (2016), pp. 9478–9485. DOI: https://doi.org/10.1002/adma.201602897 (cited on pages 10, 14, 38, 41).

[58] Jasmina A. Sichert, Yu Tong, Niklas Mutz, Mathias Vollmer, Stefan Fischer, Karolina Z. Milowska, Ramon García Cortadella, Bert Nickel, Carlos Cardenas-Daw, Jacek K. Stolarczyk, Alexander S. Urban, and Jochen Feldmann. "Quantum Size Effect in Organometal Halide Perovskite Nanoplatelets." In: *Nano Lett.* 15.10 (2015), pp. 6521–6527. DOI: 10.1021/acs.nanolett.5b02985 (cited on pages 10, 14, 15).

[59] Yehonadav Bekenstein, Brent A. Koscher, Samuel W. Eaton, Peidong Yang, and A. Paul Alivisatos. "Highly Luminescent Colloidal Nanoplates of Perovskite Cesium Lead Halide and Their Oriented Assemblies." In: *J. Am. Chem. Soc.* 137.51 (2015), pp. 16008–16011. DOI: 10.1021/jacs.5b11199 (cited on page 10).

[60] Dandan Zhang, Samuel W. Eaton, Yi Yu, Letian Dou, and Peidong Yang. "Solution-Phase Synthesis of Cesium Lead Halide Perovskite Nanowires." In: *J. Am. Chem. Soc.* 137.29 (2015), pp. 9230–9233. DOI: 10.1021/jacs.5b05404 (cited on page 10).

[61] Loredana Protesescu, Sergii Yakunin, Maryna I. Bodnarchuk, Franziska Krieg, Riccarda Caputo, Christopher H. Hendon, Ruo Xi Yang, Aron Walsh, and Maksym V. Kovalenko. "Nanocrystals of Cesium Lead Halide Perovskites ($CsPbX_3$, X = Cl, Br, and I): Novel Optoelectronic Materials Showing Bright Emission with Wide Color Gamut." In: *Nano Lett.* 15.6 (2015), pp. 3692–3696. DOI: 10.1021/nl5048779 (cited on pages 10, 11, 14, 38, 41, 63).

[62] Quinten A. Akkerman, Tan P. T. Nguyen, Simon C. Boehme, Federico Montanarella, Dmitry N. Dirin, Philipp Wechsler, Finn Beiglböck, Gabriele Rainò, Rolf Erni, Claudine Katan, Jacky Even, and Maksym V. Kovalenko. "Controlling the nucleation and growth kinetics of lead halide perovskite quantum dots." In: *Science* 377.6613 (2022), pp. 1406–1412. DOI: 10.1126/science.abq3616 (cited on pages 10, 20, 38, 41, 42, 50, 51, 62, 65).

[63] Anja Barfüßer, Sebastian Rieger, Amrita Dey, Ahmet Tosun, Quinten A. Akkerman, Tushar Debnath, and Jochen Feldmann. "Confined Excitons in Spherical-Like Halide Perovskite Quantum Dots." In: *Nano Lett.* 22.22 (2022), pp. 8810–8817. DOI: 10.1021/acs.nanolett.2c02223 (cited on pages 11, 62, 63).

[64] H. MAHR. "4 - Two-Photon Absorption Spectroscopy." In: *Quantum Electronics: A Treatise*. Ed. by HERBERT RABIN and C.L. TANG. Academic Press, 1975, pp. 285–361. DOI: https://doi.org/10.1016/B978-0-12-574001-2.50010-1 (cited on pages 11, 12).

[65] Donald M. Friedrich. "Two-photon molecular spectroscopy." In: *J. Chem. Educ.* 59.6 (1982), p. 472. DOI: 10.1021/ed059p472 (cited on pages 11, 12).

[66] Maria Göppert-Mayer. "Über Elementarakte mit zwei Quantensprüngen." In: *Ann. Phys.* 401.3 (1931), pp. 273–294. DOI: https://doi.org/10.1002/andp.19314010303 (cited on page 11).

[67] Wolfgang Demtröder. "Linienbreiten und Profile von Spektrallinien." In: *Laserspektroskopie 1: Grundlagen*. Berlin, Heidelberg: Springer Berlin Heidelberg, 2011, pp. 43–68. DOI: 10.1007/978-3-642-21306-9_3 (cited on pages 12, 13, 50).

[68] Guang S. He, Loon-Seng Tan, Qingdong Zheng, and Paras N. Prasad. "Multiphoton Absorbing Materials: Molecular Designs, Characterizations, and Applications." In: *Chem. Rev.* 108.4 (2008), pp. 1245–1330. DOI: 10.1021/cr050054x (cited on page 12).

[69] G. C. Papavassiliou. "Synthetic Three-and Lower-Dimensional Semiconductors Based on Inorganic Units." In: *Molecular Crystals and Liquid Crystals Science and Technology. Section A. Molecular Crystals and Liquid Crystals* 286.1 (1996), pp. 231–238. DOI: 10.1080/10587259608042291 (cited on page 12).

[70] Yue Wang, Xiaoming Li, Jizhong Song, Lian Xiao, Haibo Zeng, and Handong Sun. "All-Inorganic Colloidal Perovskite Quantum Dots: A New Class of Lasing Materials with Favorable Characteristics." In: *Adv. Mater.* 27.44 (2015), pp. 7101–7108. DOI: https://doi.org/10.1002/adma.201503573 (cited on page 12).

[71] Akihiro Kojima, Kenjiro Teshima, Yasuo Shirai, and Tsutomu Miyasaka. "Organometal Halide Perovskites as Visible-Light Sensitizers for Photovoltaic Cells." In: *J. Am. Chem. Soc.* 131.17 (2009), pp. 6050–6051. DOI: 10.1021/ja809598r (cited on page 12).

[72] Hui-Seon Kim, Chang-Ryul Lee, Jeong-Hyeok Im, Ki-Beom Lee, Thomas Moehl, Arianna Marchioro, Soo-Jin Moon, Robin Humphry-Baker, Jun-Ho Yum, Jacques E. Moser, Michael Grätzel, and Nam-Gyu Park. "Lead Iodide Perovskite Sensitized All-Solid-State Submicron Thin Film Mesoscopic Solar Cell with Efficiency Exceeding 9%." In: *Sci. Rep.* 2.1 (2012), p. 591. DOI: 10.1038/srep00591 (cited on page 12).

[73] Yue Wang, Xiaoming Li, Xin Zhao, Lian Xiao, Haibo Zeng, and Handong Sun. "Nonlinear Absorption and Low-Threshold Multiphoton Pumped Stimulated Emission from All-Inorganic Perovskite Nanocrystals." In: *Nano Lett.* 16.1 (2016), pp. 448–453. DOI: 10.1021/acs.nanolett.5b04110 (cited on page 12).

[74] Jialiang Xu, Xinyue Li, Jianbo Xiong, Chunqing Yuan, Sergey Semin, Theo Rasing, and Xian-He Bu. "Halide Perovskites for Nonlinear Optics." In: *Adv. Mater.* 32.3 (2020), p. 1806736. DOI: https://doi.org/10.1002/adma.201806736 (cited on page 12).

[75] Yanqing Xu, Qi Chen, Chunfeng Zhang, Rui Wang, Hua Wu, Xiaoyu Zhang, Guichuan Xing, William W. Yu, Xiaoyong Wang, Yu Zhang, and Min Xiao. "Two-Photon-Pumped Perovskite Semiconductor Nanocrystal Lasers." In: *J. Am. Chem. Soc.* 138.11 (2016), pp. 3761–3768. DOI: 10.1021/jacs.5b12662 (cited on page 12).

[76] Aurora Manzi, Yu Tong, Julius Feucht, En-Ping Yao, Lakshminarayana Polavarapu, Alexander S. Urban, and Jochen Feldmann. "Resonantly enhanced multiple exciton generation through below-band-gap multi-photon absorption in perovskite nanocrystals." In: *Nat. Commun.* 9.1 (2018), p. 1518. DOI: 10.1038/s41467-018-03965-8 (cited on pages 12, 93, 99).

[77] Robert F. Pierret. *Advanced Semiconductor Fundamentals*. 2nd ed. Modular Series on Solid State Devices. Pearson Education, Inc., 2003 (cited on pages 13, 17).

[78] Joseph R. Lakowicz, ed. *Principles of Fluorescence Spectroscopy*. Boston, MA: Springer US, 2006. DOI: 10.1007/978-0-387-46312-4 (cited on pages 13, 20–25, 47, 48, 58).

[79] Richard C. Powell and Zoltán G. Soos. "Singlet exciton energy transfer in organic solids." In: *J. Lumin.* 11.1 (1975), pp. 1–45. DOI: https://doi.org/10.1016/0022-2313(75)90077-0 (cited on page 13).

[80] Feng Wang, Yang Wu, Mark S. Hybertsen, and Tony F. Heinz. "Auger recombination of excitons in one-dimensional systems." In: *Phys. Rev. B* 73 (24 2006), p. 245424. DOI: 10.1103/PhysRevB.73.245424 (cited on page 13).

[81] Libai Huang and Todd D. Krauss. "Quantized Bimolecular Auger Recombination of Excitons in Single-Walled Carbon Nanotubes." In: *Phys. Rev. Lett.* 96 (5 2006), p. 057407. DOI: 10.1103/PhysRevLett.96.057407 (cited on page 13).

[82] Feng Liu, Yaohong Zhang, Chao Ding, Syuusuke Kobayashi, Takuya Izuishi, Naoki Nakazawa, Taro Toyoda, Tsuyoshi Ohta, Shuzi Hayase, Takashi Minemoto, Kenji Yoshino, Songyuan Dai, and Qing Shen. "Highly Luminescent Phase-Stable $CsPbI_3$ Perovskite Quantum Dots Achieving Near 100% Absolute Photoluminescence Quantum Yield." In: *ACS Nano* 11.10 (2017), pp. 10373–10383. DOI: 10.1021/acsnano.7b05442 (cited on page 14).

[83] Quinten A Akkerman, Gabriele Rainò, Maksym V Kovalenko, and Liberato Manna. "Genesis, challenges and opportunities for colloidal lead halide perovskite nanocrystals." In: *Nat. Mater.* 17.5 (2018), pp. 394–405. DOI: 10.1038/s41563-018-0018-4 (cited on pages 14, 15, 18).

[84] Quinten A. Akkerman, Valerio D'Innocenzo, Sara Accornero, Alice Scarpellini, Annamaria Petrozza, Mirko Prato, and Liberato Manna. "Tuning the Optical Properties of Cesium Lead Halide Perovskite Nanocrystals by Anion Exchange Reactions." In: *J. Am. Chem. Soc.* 137.32 (2015), pp. 10276–10281. DOI: 10.1021/jacs.5b05602 (cited on pages 14, 19, 20, 66).

[85] Xing-Fei He. "Excitons in anisotropic solids: The model of fractional-dimensional space." In: *Phys. Rev. B* 43 (3 1991), pp. 2063–2069. DOI: 10.1103/PhysRevB.43.2063 (cited on page 14).

[86] Jonathan Owen. "The coordination chemistry of nanocrystal surfaces." In: *Science* 347.6222 (2015), pp. 615–616. DOI: 10.1126/science.1259924 (cited on pages 15, 19).

[87] Carlo Giansante and Ivan Infante. "Surface Traps in Colloidal Quantum Dots: A Combined Experimental and Theoretical Perspective." In: *J. Phys. Chem. Lett.* 8.20 (2017), pp. 5209–5215. DOI: 10.1021/acs.jpclett.7b02193 (cited on pages 15, 19).

[88] Cédric Mongin, Sofia Garakyaraghi, Natalia Razgoniaeva, Mikhail Zamkov, and Felix N. Castellano. "Direct observation of triplet energy transfer from semiconductor nanocrystals." In: *Science* 351.6271 (2016), pp. 369–372. DOI: 10.1126/science.aad6378 (cited on page 15).

[89] Yu-Ho Won, Oul Cho, Taehyung Kim, Dae-Young Chung, Taehee Kim, Heejae Chung, Hyosook Jang, Junho Lee, Dongho Kim, and Eunjoo Jang. "Highly efficient and stable InP/ZnSe/ZnS quantum dot light-emitting diodes." In: *Nature* 575.7784 (2019), pp. 634–638. DOI: 10.1038/s41586-019-1771-5 (cited on page 15).

[90] Peter Y. Yu and Manuel Cardona. "Electronic Properties of Defects." In: *Fundamentals of Semiconductors: Physics and Materials Properties*. Berlin, Heidelberg: Springer Berlin Heidelberg, 2010, pp. 159–202. DOI: 10.1007/978-3-642-00710-1_4 (cited on pages 15–17, 26, XXI).

[91] Hans J. Queisser and Eugene E. Haller. "Defects in Semiconductors: Some Fatal, Some Vital." In: *Science* 281.5379 (1998), pp. 945–950. DOI: 10.1126/science.281.5379.945 (cited on pages 16, 17).

[92] W. Shockley and W. T. Read. "Statistics of the Recombinations of Holes and Electrons." In: *Phys. Rev.* 87 (5 1952), pp. 835–842. DOI: 10.1103/PhysRev.87.835 (cited on page 17).

[93] R. N. Hall. "Electron-Hole Recombination in Germanium." In: *Phys. Rev.* 87 (2 1952), pp. 387–387. DOI: 10.1103/PhysRev.87.387 (cited on page 17).

[94] Michael J. Trimpl, Adam D. Wright, Kelly Schutt, Leonardo R. V. Buizza, Zhiping Wang, Michael B. Johnston, Henry J. Snaith, Peter Müller-Buschbaum, and Laura M. Herz. "Charge-Carrier Trapping and Radiative Recombination in Metal Halide Perovskite Semiconductors." In: *Adv. Funct. Mater.* 30.42 (2020), p. 2004312. DOI: https://doi.org/10.1002/adfm.202004312 (cited on pages 17, 18).

[95] Michael B. Johnston and Laura M. Herz. "Hybrid Perovskites for Photovoltaics: Charge-Carrier Recombination, Diffusion, and Radiative Efficiencies." In: *Acc. Chem. Res.* 49.1 (2016), pp. 146–154. DOI: 10.1021/acs.accounts.5b00411 (cited on page 18).

[96] Stephanie ten Brinck, Francesco Zaccaria, and Ivan Infante. "Defects in Lead Halide Perovskite Nanocrystals: Analogies and (Many) Differences with the Bulk." In: *ACS Energy Lett.* 4.11 (2019), pp. 2739–2747. DOI: 10.1021/acsenergylett.9b01945 (cited on pages 18, 19).

[97] Quinten A. Akkerman, Silvia Genaro Motti, Ajay Ram Srimath Kandada, Edoardo Mosconi, Valerio D'Innocenzo, Giovanni Bertoni, Sergio Marras, Brett A. Kamino, Laura Miranda, Filippo De Angelis, Annamaria Petrozza, Mirko Prato, and Liberato Manna. "Solution Synthesis Approach to Colloidal Cesium Lead Halide Perovskite Nanoplatelets with Monolayer-Level Thickness Control." In: *J. Am. Chem. Soc.* 138.3 (2016), pp. 1010–1016. DOI: 10.1021/jacs.5b12124 (cited on page 19).

[98] Yang Zhou, Jie Chen, Osman M. Bakr, and Hong-Tao Sun. "Metal-Doped Lead Halide Perovskites: Synthesis, Properties, and Optoelectronic Applications." In: *Chem. Mater.* 30.19 (2018), pp. 6589–6613. DOI: 10.1021/acs.chemmater.8b02989 (cited on pages 19, 20).

[99] Raihana Begum, Manas R. Parida, Ahmed L. Abdelhady, Banavoth Murali, Noktan M. Alyami, Ghada H. Ahmed, Mohamed Nejib Hedhili, Osman M. Bakr, and Omar F. Mohammed. "Engineering Interfacial Charge Transfer in CsPbBr3 Perovskite Nanocrystals by Heterovalent Doping." In: *J. Am. Chem. Soc.* 139.2 (2017), pp. 731–737. DOI: 10.1021/jacs.6b09575 (cited on pages 19, 66, 69, 75).

[100] Jun Yin, Ghada H. Ahmed, Osman M. Bakr, Jean-Luc Brédas, and Omar F. Mohammed. "Unlocking the Effect of Trivalent Metal Doping in All-Inorganic $CsPbBr_3$ Perovskite." In: *ACS Energy Lett.* 4.3 (2019), pp. 789–795. DOI: 10.1021/acsenergylett.9b00209 (cited on pages 19, 68, 69, 80).

[101] Shovon Chatterjee, Mainak Ghosal, Khushubo Tiwari, and Pratik Sen. "Potassium-Induced Passivation of Deep Traps in Bismuth-Doped Hybrid Lead Bromide Perovskite Nanocrystals: Massive Amplification of Photoluminescence Quantum Yield." In: *J. Phys. Chem. Lett.* 12.1 (2021), pp. 546–551. DOI: 10.1021/acs.jpclett.0c03092 (cited on pages 19, 69).

[102] Brent A. Koscher, Joseph K. Swabeck, Noah D. Bronstein, and A. Paul Alivisatos. "Essentially Trap-Free CsPbBr3 Colloidal Nanocrystals by Postsynthetic Thiocyanate Surface Treatment." In: *J. Am. Chem. Soc.* 139.19 (2017), pp. 6566–6569. DOI: 10.1021/jacs.7b02817 (cited on page 19).

[103] Young-Hoon Kim, Yaxin Zhai, E. Ashley Gaulding, Severin N. Habisreutinger, Taylor Moot, Bryan A. Rosales, Haipeng Lu, Abhijit Hazarika, Roman Brunecky, Lance M. Wheeler, Joseph J. Berry, Matthew C. Beard, and Joseph M. Luther. "Strategies to Achieve High Circularly Polarized Luminescence from Colloidal Organic–Inorganic Hybrid Perovskite Nanocrystals." In: *ACS Nano* 14.7 (2020), pp. 8816–8825. DOI: 10.1021/acsnano.0c03418 (cited on pages 19, 35).

[104] Donglin Jia, Jingxuan Chen, Mei Yu, Jianhua Liu, Erik M. J. Johansson, Anders Hagfeldt, and Xiaoliang Zhang. "Dual Passivation of CsPbI3 Perovskite Nanocrystals with Amino Acid Ligands for Efficient Quantum Dot Solar Cells." In: *Small* 16.24 (2020), p. 2001772. DOI: https://doi.org/10.1002/smll.202001772 (cited on page 19).

[105] Jahangeer Khan, Xuliang Zhang, Jianyu Yuan, Yao Wang, Guozheng Shi, Robert Patterson, Junwei Shi, Xufeng Ling, Long Hu, Tom Wu, Songyuan Dai, and Wanli Ma. "Tuning the Surface-Passivating Ligand Anchoring Position Enables Phase Robustness in CsPbI3 Perovskite Quantum Dot Solar Cells." In: *ACS Energy Lett.* 5.10 (2020), pp. 3322–3329. DOI: 10.1021/acsenergylett.0c01849 (cited on page 19).

[106] Navendu Mondal, Apurba De, and Anunay Samanta. "Achieving Near-Unity Photoluminescence Efficiency for Blue-Violet-Emitting Perovskite Nanocrystals." In: *ACS Energy Lett.* 4.1 (2019), pp. 32–39. DOI: 10.1021/acsenergylett.8b01909 (cited on page 19).

[107] Fei Li, Ying Liu, Hongliang Wang, Qian Zhan, Quanlin Liu, and Zhiguo Xia. "Postsynthetic Surface Trap Removal of $CsPbX_3$ (X = Cl, Br, or I) Quantum Dots via a ZnX2/Hexane Solution toward an Enhanced Luminescence Quantum Yield." In: *Chem. Mater.* 30.23 (2018), pp. 8546–8554. DOI: 10.1021/acs.chemmater.8b03442 (cited on page 19).

[108] Georgian Nedelcu, Loredana Protesescu, Sergii Yakunin, Maryna I. Bodnarchuk, Matthias J. Grotevent, and Maksym V. Kovalenko. "Fast Anion-Exchange in Highly Luminescent Nanocrystals of Cesium Lead Halide Perovskites ($CsPbX_3$, X = Cl, Br, I)." In: *Nano Lett.* 15.8 (2015), pp. 5635–5640. DOI: 10.1021/acs.nanolett.5b02404 (cited on pages 19, 20).

[109] Jonathan De Roo, Maria Ibáñez, Pieter Geiregat, Georgian Nedelcu, Willem Walravens, Jorick Maes, Jose C. Martins, Isabel Van Driessche, Maksym V. Kovalenko, and Zeger Hens. "Highly Dynamic Ligand Binding and Light Absorption Coefficient of Cesium Lead Bromide Perovskite Nanocrystals." In: *ACS Nano* 10.2 (2016), pp. 2071–2081. DOI: 10.1021/acsnano.5b06295 (cited on page 19).

[110] Jorick Maes, Lieve Balcaen, Emile Drijvers, Qiang Zhao, Jonathan De Roo, André Vantomme, Frank Vanhaecke, Pieter Geiregat, and Zeger Hens. "Light Absorption Coefficient of CsPbBr3 Perovskite Nanocrystals." In: *J. Phys. Chem. Lett.* 9.11 (2018), pp. 3093–3097. DOI: 10.1021/acs.jpclett.8b01065 (cited on pages 19, 49).

[111] Junichiro Mizusaki, Kimiyasu Arai, and Kazuo Fueki. "Ionic conduction of the perovskite-type halides." In: *Solid State Ionics* 11.3 (1983), pp. 203–211. DOI: https://doi.org/10.1016/0167-2738(83)90025-5 (cited on page 20).

[112] Loredana Protesescu, Sergii Yakunin, Sudhir Kumar, Janine Bär, Federica Bertolotti, Norberto Masciocchi, Antonietta Guagliardi, Matthias Grotevent, Ivan Shorubalko, Maryna I. Bodnarchuk, Chih-Jen Shih, and Maksym V. Kovalenko. "Dismantling the "Red Wall" of Colloidal Perovskites: Highly Luminescent Formamidinium and Formamidinium–Cesium Lead Iodide Nanocrystals." In: *ACS Nano* 11.3 (2017), pp. 3119–3134. DOI: 10.1021/acsnano.7b00116 (cited on page 20).

[113] Di Gao, Bo Qiao, Zheng Xu, Dandan Song, Pengjie Song, Zhiqin Liang, Zhaohui Shen, Jingyue Cao, Junjie Zhang, and Suling Zhao. "Postsynthetic, Reversible Cation Exchange between Pb^2+ and Mn^2+ in Cesium Lead Chloride Perovskite Nanocrystals." In: *J. Phys. Chem. C* 121.37 (2017), pp. 20387–20395. DOI: 10.1021/acs.jpcc.7b06929 (cited on page 20).

[114] Guangguang Huang, Chunlei Wang, Shuhong Xu, Shenfei Zong, Ju Lu, Zhuyuan Wang, Changgui Lu, and Yiping Cui. "Postsynthetic Doping of $MnCl_2$ Molecules into Preformed $CsPbBr_3$ Perovskite Nanocrystals via a Halide Exchange-Driven Cation Exchange." In: *Adv. Mater.* 29.29 (2017), p. 1700095. DOI: https://doi.org/10.1002/adma.201700095 (cited on page 20).

[115] Horst Schmidt-Böcking, Karin Reich, Alan Templeton, Wolfgang Trageser, and Volkmar Vill. "S10, Otto Stern und Max Volmer, Über die Abklingungszeit der Fluoreszenz. Physik. Z., 20, 183–188 (1919)." In: *Otto Sterns Veröffentlichungen – Band 2: Sterns Veröffentlichungen von 1916 bis 1926*. Ed. by Horst Schmidt-Böcking, Karin Reich, Alan Templeton, Wolfgang Trageser, and Volkmar Vill. Berlin, Heidelberg: Springer Berlin Heidelberg, 2016, pp. 79–85. DOI: 10.1007/978-3-662-46962-0_5 (cited on page 21).

[116] Z. Lakos, A. Szarka, and B. Somogyi. "Fluorescence Quenching in Membrane Phase." In: *Biochem. Biophys. Res. Commun.* 208.1 (1995), pp. 111–117. DOI: https://doi.org/10.1006/bbrc.1995.1312 (cited on page 21).

[117] Alexander Kyrychenko. "Using fluorescence for studies of biological membranes: a review." In: *Methods Appl. Fluoresc.* 3.4 (2015), p. 042003. DOI: 10.1088/2050-6120/3/4/042003 (cited on page 21).

[118] Marian Smoluchowski. "Drei Vorträge über Diffusion, Brownsche Molekularbewegung und Koagulation von Kolloidteilchen." ger. In: *Pisma Mariana Smoluchowskiego* 2.1 (1927), pp. 530–594 (cited on pages 22, 24).

[119] Perrin, Francis. "Théorie quantique des transferts d´activation entre molécules de même espèce. Cas des solutions fluorescentes." In: *Ann. Phys.* 10.17 (1932), pp. 283–314. DOI: 10.1051/anphys/193210170283 (cited on pages 23, 24).

[120] J. M. Frank and S. J. Wawilow. "Über die Wirkungssphäre der Auslöschungsvorgänge in den fluoreszierenden Flüssigkeiten." In: *Z. Phys.* 69.1 (1931), pp. 100–110. DOI: 10.1007/BF01391516 (cited on pages 23, 24).

[121] William Limm, Mitchell A. Winnik, Barton A. Smith, and Deirdre T. Stanton. "Solvent Concentration Profile of Poly(methyl methacrylate) Dissolving in Methyl Ethyl Ketone." In: vol. 412. ACS Symposium Series. 0. American Chemical Society, 1989, pp. 385–399. DOI: 10.1021/bk-1989-0412.ch023 (cited on page 24).

[122] Thomas L. Nemzek and William R. Ware. "Kinetics of diffusion-controlled reactions: Transient effects in fluorescence quenching." In: *J. Chem. Phys.* 62.2 (2008), pp. 477–489. DOI: 10.1063/1.430501 (cited on pages 24, 25).

[123] B. Sveshnikoff. "On the Theory of Photochemical Reactions and Chemiluminescence in Solutions." In: *Acta Physicochimica U.R.S.S., Academy of Sciences of the U.S.S.R.* 3 (1935), 257–268 (cited on page 24).

[124] William R. Ware and Joel S. Novros. "Kinetics of Diffusion-Controlled Reactions. An Experimental Test of the Theory as Applied to Fluorescence Quenching." In: *J. Phys. Chem.* 70.10 (1966), pp. 3246–3253. DOI: 10.1021/j100882a038 (cited on page 24).

[125] Mark Fox. *Quantum Optics: An Introduction*. New York: Oxford University Press, 2006 (cited on pages 26, 27).

[126] Jean-Michel Gérard and Bruno Gayral. "Semiconductor microcavities, quantum boxes and the Purcell effect." In: *Confined Photon Systems*. Ed. by Henri Benisty, Claude Weisbuch, École Polytechnique, Jean-Michel Gérard, Romuald Houdré, and John Rarity. Berlin, Heidelberg: Springer Berlin Heidelberg, 1999, pp. 331–351. DOI: 10.1007/BFb0104387 (cited on page 26).

[127] STUART D. BRORSON and PETER M. W. SKOVGAARD. "OPTICAL MODE DENSITY AND SPONTANEOUS EMISSION IN MICROCAVITIES." In: *Optical Processes in Microcavities*, pp. 77–99. DOI: 10.1142/9789812830760_0002 (cited on page 27).

[128] E. M. Purcell. "Spontaneous Emission Probabilities at Radio Frequencies." In: *Proceedings of the American Physical Society*. Vol. 69. American Physical Society, 1946, pp. 674–674. DOI: 10.1103/PhysRev.69.674.2 (cited on page 27).

[129] K.H. Drexhage. "Influence of a dielectric interface on fluorescence decay time." In: *J. Lumin.* 1-2 (1970), pp. 693–701. DOI: https://doi.org/10.1016/0022-2313(70)90082-7 (cited on page 27).

[130] C. C. Lee and H. Y. Fan. "Two-photon absorption with exciton effect for degenerate valence bands." In: *Phys. Rev. B* 9 (8 1974), pp. 3502–3516. DOI: 10.1103/PhysRevB.9.3502 (cited on page 27).

[131] Emiliano Cortés, Fedja J. Wendisch, Luca Sortino, Andrea Mancini, Simone Ezendam, Seryio Saris, Leonardo de S. Menezes, Andreas Tittl, Haoran Ren, and Stefan A. Maier. "Optical Metasurfaces for Energy Conversion." In: *Chem. Rev.* 122.19 (2022), pp. 15082–15176. DOI: 10.1021/acs.chemrev.2c00078 (cited on pages 27–31, 88).

[132] Subal Kar. "Metamaterials or left-handed materials—a counter-intuitive artificial material." In: *Metamaterials and Metasurfaces*. 2053-2563. IOP Publishing, 2023, 1–1 to 1–48. DOI: 10.1088/978-0-7503-5532-2ch1 (cited on page 27).

[133] Pete Vukusic and J. Roy Sambles. "Photonic structures in biology." In: *Nature* 424.6950 (2003), pp. 852–855. DOI: 10.1038/nature01941 (cited on page 28).

[134] Hou-Tong Chen, J. Antoinette Taylor, and Nanfang Yu. "A review of metasurfaces: physics and applications." In: *Rep. Prog. Phys.* 79.7 (2016), p. 076401. DOI: 10.1088/0034-4885/79/7/076401 (cited on pages 28–30).

[135] Nina Meinzer, William L. Barnes, and Ian R. Hooper. "Plasmonic meta-atoms and metasurfaces." In: *Nat. Photonics* 8.12 (2014), pp. 889–898. DOI: 10.1038/nphoton.2014.247 (cited on page 28).

[136] Arseniy I. Kuznetsov, Andrey E. Miroshnichenko, Mark L. Brongersma, Yuri S. Kivshar, and Boris Luk'yanchuk. "Optically resonant dielectric nanostructures." In: *Science* 354.6314 (2016), aag2472. DOI: 10.1126/science.aag2472 (cited on page 28).

[137] Cheng-Wei Qiu, Tan Zhang, Guangwei Hu, and Yuri Kivshar. "Quo Vadis, Metasurfaces?" In: *Nano Lett.* 21.13 (2021), pp. 5461–5474. DOI: 10.1021/acs.nanolett.1c00828 (cited on pages 28, 31).

[138] Stefan A. Maier. *Plasmonics: Fundamentals and Applications*. 1st ed. Springer New York, NY, 2007 (cited on pages 28–30, 102).

[139] Eugene Hecht. *Optik*. 7th ed. Berlin, Boston: De Gruyter, 2018. DOI: doi:10.1515/9783110526653 (cited on pages 29, 32, 33, 47, 55).

[140] Patrice Genevet, Federico Capasso, Francesco Aieta, Mohammadreza Khorasaninejad, and Robert Devlin. "Recent advances in planar optics: from plasmonic to dielectric metasurfaces." In: *Optica* 4.1 (2017), pp. 139–152. DOI: 10.1364/OPTICA.4.000139 (cited on page 30).

[141] Qiong He, Shulin Sun, Shiyi Xiao, and Lei Zhou. "High-Efficiency Metasurfaces: Principles, Realizations, and Applications." In: *Adv. Opt. Mater.* 6.19 (2018), p. 1800415. DOI: https://doi.org/10.1002/adom.201800415 (cited on page 30).

[142] Nanfang Yu, Patrice Genevet, Mikhail A. Kats, Francesco Aieta, Jean-Philippe Tetienne, Federico Capasso, and Zeno Gaburro. "Light Propagation with Phase Discontinuities: Generalized Laws of Reflection and Refraction." In: *Science* 334.6054 (2011), pp. 333–337. DOI: 10.1126/science.1210713 (cited on page 30).

[143] Dianmin Lin, Pengyu Fan, Erez Hasman, and Mark L. Brongersma. "Dielectric gradient metasurface optical elements." In: *Science* 345.6194 (2014), pp. 298–302. DOI: 10.1126/science.1253213 (cited on page 30).

[144] Nanfang Yu, Francesco Aieta, Patrice Genevet, Mikhail A. Kats, Zeno Gaburro, and Federico Capasso. "A Broadband, Background-Free Quarter-Wave Plate Based on Plasmonic Metasurfaces." In: *Nano Lett.* 12.12 (2012), pp. 6328–6333. DOI: 10.1021/nl303445u (cited on page 30).

[145] V. G. Kravets, A. V. Kabashin, W. L. Barnes, and A. N. Grigorenko. "Plasmonic Surface Lattice Resonances: A Review of Properties and Applications." In: *Chem. Rev.* 118.12 (2018), pp. 5912–5951. DOI: 10.1021/acs.chemrev.8b00243 (cited on page 31).

[146] Gyeongtae Kim, Yeseul Kim, Jooyeong Yun, Seong-Won Moon, Seokwoo Kim, Jaekyung Kim, Junkyeong Park, Trevon Badloe, Inki Kim, and Junsuk Rho. "Metasurface-driven full-space structured light for three-dimensional imaging." In: *Nat. Commun.* 13.1 (2022), p. 5920. DOI: 10.1038/s41467-022-32117-2 (cited on page 31).

[147] Andreas Tittl, Aleksandrs Leitis, Mingkai Liu, Filiz Yesilkoy, Duk-Yong Choi, Dragomir N. Neshev, Yuri S. Kivshar, and Hatice Altug. "Imaging-based molecular barcoding with pixelated dielectric metasurfaces." In: *Science* 360.6393 (2018), pp. 1105–1109. DOI: 10.1126/science.aas9768 (cited on page 31).

[148] Luca M. Berger, Martin Barkey, Stefan A. Maier, and Andreas Tittl. "Metallic and All-Dielectric Metasurfaces Sustaining Displacement-Mediated Bound States in the Continuum." In: *Adv. Opt. Mater.* n/a.n/a (), p. 2301269. DOI: https://doi.org/10.1002/adom.202301269 (cited on page 31).

[149] P. Spinelli, M. A. Verschuuren, and A. Polman. "Broadband omnidirectional antireflection coating based on subwavelength surface Mie resonators." In: *Nat. Commun.* 3.1 (2012), p. 692. DOI: 10.1038/ncomms1691 (cited on page 31).

[150] Kseniia Baryshnikova, Dmitry Gets, Tatiana Liashenko, Anatoly Pushkarev, Ivan Mukhin, Yuri Kivshar, and Sergey Makarov. "Broadband Antireflection with Halide Perovskite Metasurfaces." In: *Laser Photonics Rev.* 14.12 (2020), p. 2000338. DOI: https://doi.org/10.1002/lpor.202000338 (cited on page 31).

[151] Christiane Becker, Sven Burger, Carlo Barth, Phillip Manley, Klaus Jäger, David Eisenhauer, Grit Köppel, Pavel Chabera, Junsheng Chen, Kaibo Zheng, and Tõnu Pullerits. "Nanophotonic-Enhanced Two-Photon-Excited Photoluminescence of Perovskite Quantum Dots." In: *ACS Photonics* 5.11 (2018), pp. 4668–4676. DOI: 10.1021/acsphotonics.8b01199 (cited on page 31).

[152] Pericles S. Theocaris and Emmanuel E. Gdoutos. "Description of Polarized Light." In: *Matrix Theory of Photoelasticity*. Berlin, Heidelberg: Springer Berlin Heidelberg, 1979, pp. 20–44. DOI: 10.1007/978-3-540-35789-6_3 (cited on page 33).

[153] Guankui Long, Randy Sabatini, Makhsud I. Saidaminov, Girish Lakhwani, Abdullah Rasmita, Xiaogang Liu, Edward H. Sargent, and Weibo Gao. "Chiral-perovskite optoelectronics." In: *Nat. Rev. Mater.* 5.6 (2020), pp. 423–439. DOI: 10.1038/s41578-020-0181-5 (cited on page 33).

[154] Bengt Nordén, Alison Rodger, and Timothy Daffon. *Linear Dichroism and Circular Dichroism: A Textbook on Polarized-Light Spectroscopy*. Cambridge: RSC Publishing, 2010 (cited on page 33).

[155] Martin Schäferling. "Chiral Properties of Light." In: *Chiral Nanophotonics: Chiral Optical Properties of Plasmonic Systems*. Cham: Springer International Publishing, 2017, pp. 61–75. DOI: 10.1007/978-3-319-42264-0_4 (cited on pages 33, 34).

[156] L. Rosenfeld. "Quantenmechanische Theorie der natürlichen optischen Aktivität von Flüssigkeiten und Gasen." In: *Z. Phys.* 52.3 (1929), pp. 161–174. DOI: 10.1007/BF01342393 (cited on page 33).

[157] E Plum, V A Fedotov, and N I Zheludev. "Extrinsic electromagnetic chirality in metamaterials." In: *J. Opt. A: Pure Appl. Opt.* 11.7 (2009), p. 074009. DOI: 10.1088/1464-4258/11/7/074009 (cited on page 34).

[158] Meng Qiu, Lei Zhang, Zhixiang Tang, Wei Jin, Cheng-Wei Qiu, and Dang Yuan Lei. "3D Metaphotonic Nanostructures with Intrinsic Chirality." In: *Adv. Funct. Mater.* 28.45 (2018), p. 1803147. DOI: https://doi.org/10.1002/adfm.201803147 (cited on page 34).

[159] Zheni N. Georgieva, Brian P. Bloom, Supriya Ghosh, and David H. Waldeck. "Imprinting Chirality onto the Electronic States of Colloidal Perovskite Nanoplatelets." In: *Adv. Mater.* 30.23 (2018), p. 1800097. DOI: https://doi.org/10.1002/adma.201800097 (cited on page 35).

[160] Kanchan Mishra, Dylana Guyon, Jovan San Martin, and Yong Yan. "Chiral Perovskite Nanocrystals for Asymmetric Reactions: A Highly Enantioselective Strategy for Photocatalytic Synthesis of N–C Axially Chiral Heterocycles." In: *J. Am. Chem. Soc.* 145.31 (2023), pp. 17242–17252. DOI: 10.1021/jacs.3c04593 (cited on page 35).

[161] Hafiz Saad Khaliq, Asad Nauman, Jae-Won Lee, and Hak-Rin Kim. "Recent Progress on Plasmonic and Dielectric Chiral Metasurfaces: Fundamentals, Design Strategies, and Implementation." In: *Adv. Opt. Mater.* 11.16 (2023), p. 2300644. DOI: https://doi.org/10.1002/adom.202300644 (cited on page 35).

[162] Guankui Long, Giorgio Adamo, Jingyi Tian, Maciej Klein, Harish N. S. Krishnamoorthy, Elena Feltri, Hebin Wang, and Cesare Soci. "Perovskite metasurfaces with large superstructural chirality." In: *Nat. Commun.* 13.1 (2022), p. 1551. DOI: 10.1038/s41467-022-29253-0 (cited on page 35).

[163] Babak Ziaie, Antonio Baldi, and Massood Z. Atashbar. "Introduction to Micro-/Nanofabrication." In: *Springer Handbook of Nanotechnology*. Ed. by Bharat Bhushan. Berlin, Heidelberg: Springer Berlin Heidelberg, 2010, pp. 231–269. DOI: 10.1007/978-3-642-02525-9_8 (cited on pages 37, 43).

[164] Loredana Protesescu, Sergii Yakunin, Olga Nazarenko, Dmitry N. Dirin, and Maksym V. Kovalenko. "Low-Cost Synthesis of Highly Luminescent Colloidal Lead Halide Perovskite Nanocrystals by Wet Ball Milling." In: *ACS Appl. Nano Mater.* 1.3 (2018), pp. 1300–1308. DOI: 10.1021/acsanm.8b00038 (cited on page 38).

[165] Nguyen T. K. Thanh, N. Maclean, and S. Mahiddine. "Mechanisms of Nucleation and Growth of Nanoparticles in Solution." In: *Chem. Rev.* 114.15 (2014), pp. 7610–7630. DOI: 10.1021/cr400544s (cited on pages 38, 39).

[166] Yadong Yin and A. Paul Alivisatos. "Colloidal nanocrystal synthesis and the organic–inorganic interface." In: *Nature* 437.7059 (2005), pp. 664–670. DOI: 10.1038/nature04165 (cited on pages 38–43).

[167] Abhishek Kumar Soni, Rashmi Joshi, and Raghumani Singh Ningthoujam. "Hot Injection Method for Nanoparticle Synthesis: Basic Concepts, Examples and Applications." In: *Handbook on Synthesis Strategies for Advanced Materials : Volume-I: Techniques and Fundamentals*. Ed. by A. K. Tyagi and Raghumani S. Ningthoujam. Singapore: Springer Singapore, 2021, pp. 383–434. DOI: 10.1007/978-981-16-1807-9_13 (cited on pages 38–41).

[168] Amelie Heuer-Jungemann, Neus Feliu, Ioanna Bakaimi, Majd Hamaly, Alaaldin Alkilany, Indranath Chakraborty, Atif Masood, Maria F. Casula, Athanasia Kostopoulou, Eunkeu Oh, Kimihiro Susumu, Michael H. Stewart, Igor L. Medintz, Emmanuel Stratakis, Wolfgang J. Parak, and Antonios G. Kanaras. "The Role of Ligands in the Chemical Synthesis and Applications of Inorganic Nanoparticles." In: *Chem. Rev.* 119.8 (2019), pp. 4819–4880. DOI: 10.1021/acs.chemrev.8b00733 (cited on pages 39, 43).

[169] Tadao Sugimoto. "Chapter 6 - General Principles for the Formation of Monodispersed Particles." In: *Monodispersed Particles (Second Edition)*. Ed. by Tadao Sugimoto. Second Edition. Amsterdam: Elsevier, 2019, pp. 209–223. DOI: https://doi.org/10.1016/B978-0-444-62749-0.00006-5 (cited on page 39).

[170] Soon Gu Kwon and Taeghwan Hyeon. "Formation Mechanisms of Uniform Nanocrystals via Hot-Injection and Heat-Up Methods." In: *Small* 7.19 (2011), pp. 2685–2702. DOI: https://doi.org/10.1002/smll.201002022 (cited on page 39).

[171] Peter Reiss, Myriam Protière, and Liang Li. "Core/Shell Semiconductor Nanocrystals." In: *Small* 5.2 (2009), pp. 154–168. DOI: https://doi.org/10.1002/smll.200800841 (cited on page 39).

[172] Luigi Carbone and P. Davide Cozzoli. "Colloidal heterostructured nanocrystals: Synthesis and growth mechanisms." In: *Nano Today* 5.5 (2010), pp. 449–493. DOI: https://doi.org/10.1016/j.nantod.2010.08.006 (cited on page 39).

[173] Victor K. LaMer and Robert H. Dinegar. "Theory, Production and Mechanism of Formation of Monodispersed Hydrosols." In: *J. Am. Chem. Soc.* 72.11 (1950), pp. 4847–4854. DOI: 10.1021/ja01167a001 (cited on page 39).

[174] Tadao Sugimoto. "Chapter 1 - Nucleation." In: *Monodispersed Particles (Second Edition)*. Ed. by Tadao Sugimoto. Second Edition. Amsterdam: Elsevier, 2019, pp. 3–94. DOI: https://doi.org/10.1016/B978-0-444-62749-0.00001-6 (cited on page 39).

[175] Tadao Sugimoto. "Chapter 2 - Growth." In: *Monodispersed Particles (Second Edition)*. Ed. by Tadao Sugimoto. Second Edition. Amsterdam: Elsevier, 2019, pp. 95–124. DOI: https://doi.org/10.1016/B978-0-444-62749-0.00002-8 (cited on page 39).

[176] Guilherme Almeida, Olivia J. Ashton, Luca Goldoni, Daniela Maggioni, Urko Petralanda, Nimai Mishra, Quinten A. Akkerman, Ivan Infante, Henry J. Snaith, and Liberato Manna. "The Phosphine Oxide Route toward Lead Halide Perovskite Nanocrystals." In: *J. Am. Chem. Soc.* 140.44 (2018), pp. 14878–14886. DOI: 10.1021/jacs.8b08978 (cited on pages 41, 42, 64).

[177] Ilka Vinçon, Fedja J. Wendisch, Daniele De Gregorio, Stefanie D. Pritzl, Quinten A. Akkerman, Haoran Ren, Leonardo de S. Menezes, Stefan A. Maier, and Jochen Feldmann. "Strong Polarization Dependent Nonlinear Excitation of a Perovskite Nanocrystal Monolayer on a Chiral Dielectric Nanoantenna Array." In: *ACS Photonics* 9.11 (2022), pp. 3506–3514. DOI: 10.1021/acsphotonics.2c00159 (cited on pages 41, 85).

[178] D. H. Everett. In: *Pure Appl. Chem.* 31.4 (1972), pp. 577–638. DOI: doi:10.1351/pac197231040577 (cited on page 41).

[179] Miriam Koolyk, Daniel Amgar, Sigalit Aharon, and Lioz Etgar. "Kinetics of cesium lead halide perovskite nanoparticle growth; focusing and de-focusing of size distribution." In: *Nanoscale* 8 (12 2016), pp. 6403–6409. DOI: 10.1039/C5NR09127F (cited on page 41).

[180] Franziska Krieg, Stefan T. Ochsenbein, Sergii Yakunin, Stephanie ten Brinck, Philipp Aellen, Adrian Süess, Baptiste Clerc, Dominic Guggisberg, Olga Nazarenko, Yevhen Shynkarenko, Sudhir Kumar, Chih-Jen Shih, Ivan Infante, and Maksym V. Kovalenko. "Colloidal $CsPbX_3$ (X = Cl, Br, I) Nanocrystals 2.0: Zwitterionic Capping Ligands for Improved Durability and Stability." In: *ACS Energy Lett.* 3.3 (2018), pp. 641–646. DOI: 10.1021/acsenergylett.8b00035 (cited on pages 42, 64).

[181] Franziska Krieg, Quy K. Ong, Max Burian, Gabriele Rainò, Denys Naumenko, Heinz Amenitsch, Adrian Süess, Matthias J. Grotevent, Frank Krumeich, Maryna I. Bodnarchuk, Ivan Shorubalko, Francesco Stellacci, and Maksym V. Kovalenko. "Stable Ultraconcentrated and Ultradilute Colloids of $CsPbX_3$ (X = Cl, Br) Nanocrystals Using Natural Lecithin as a Capping Ligand." In: *J. Am. Chem. Soc.* 141.50 (2019), pp. 19839–19849. DOI: 10.1021/jacs.9b09969 (cited on pages 42, 64).

[182] Catherine J. Murphy, Tapan K. Sau, Anand M. Gole, Christopher J. Orendorff, Jinxin Gao, Linfeng Gou, Simona E. Hunyadi, and Tan Li. "Anisotropic Metal Nanoparticles: Synthesis, Assembly, and Optical Applications." In: *J. Phys. Chem. B* 109.29 (2005), pp. 13857–13870. DOI: 10.1021/jp0516846 (cited on page 42).

[183] Xiaogang Peng, Liberato Manna, Weidong Yang, Juanita Wickham, Erik Scher, Andreas Kadavanich, and A. P. Alivisatos. "Shape control of CdSe nanocrystals." In: *Nature* 404.6773 (2000), pp. 59–61. DOI: https://doi.org/10.1038/35003535 (cited on page 43).

[184] Liberato Manna, Erik C. Scher, and A. Paul Alivisatos. "Synthesis of Soluble and Processable Rod-, Arrow-, Teardrop-, and Tetrapod-Shaped CdSe Nanocrystals." In: *J. Am. Chem. Soc.* 122.51 (2000), pp. 12700–12706. DOI: 10.1021/ja003055+ (cited on page 43).

[185] Guilherme Almeida, Luca Goldoni, Quinten Akkerman, Zhiya Dang, Ali Hossain Khan, Sergio Marras, Iwan Moreels, and Liberato Manna. "Role of Acid–Base Equilibria in the Size, Shape, and Phase Control of Cesium Lead Bromide Nanocrystals." In: *ACS Nano* 12.2 (2018), pp. 1704–1711. DOI: 10.1021/acsnano.7b08357 (cited on pages 43, 64).

[186] Shibin Sun, Dan Yuan, Yuan Xu, Aifei Wang, and Zhengtao Deng. "Ligand-Mediated Synthesis of Shape-Controlled Cesium Lead Halide Perovskite Nanocrystals via Reprecipitation Process at Room Temperature." In: *ACS Nano* 10.3 (2016), pp. 3648–3657. DOI: 10.1021/acsnano.5b08193 (cited on page 43).

[187] Aizhao Pan, Bo He, Xiaoyun Fan, Zeke Liu, Jeffrey J. Urban, A. Paul Alivisatos, Ling He, and Yi Liu. "Insight into the Ligand-Mediated Synthesis of Colloidal CsPbBr3 Perovskite Nanocrystals: The Role of Organic Acid, Base, and Cesium Precursors." In: *ACS Nano* 10.8 (2016), pp. 7943–7954. DOI: 10.1021/acsnano.6b03863 (cited on page 43).

[188] Narayan Pradhan. "Why Do Perovskite Nanocrystals Form Nanocubes and How Can Their Facets Be Tuned? A Perspective from Synthetic Prospects." In: *ACS Energy Lett.* 6.1 (2021), pp. 92–99. DOI: 10.1021/acsenergylett.0c02099 (cited on pages 43, 78).

[189] Alexandra Boltasseva and Vladimir M. Shalaev. "Fabrication of optical negative-index metamaterials: Recent advances and outlook." In: *Metamaterials* 2.1 (2008), pp. 1–17. DOI: https://doi.org/10.1016/j.metmat.2008.03.004 (cited on page 43).

[190] E. Abbe. "Beiträge zur Theorie des Mikroskops und der mikroskopischen Wahrnehmung." In: *Arch. Mikrosk. Anat.* 9.1 (1873), pp. 413–468. DOI: https://doi.org/10.1007/BF02956173 (cited on page 44).

[191] De Broglie, Louis. "Recherches sur la théorie des Quanta." In: *Ann. Phys.* 10.3 (1925), pp. 22–128. DOI: 10.1051/anphys/192510030022 (cited on page 44).

[192] Tobias Klein, Egbert Buhr, and Carl Georg Frase. "Chapter 6 - TSEM: A Review of Scanning Electron Microscopy in Transmission Mode and Its Applications." In: *Advances in Imaging and Electron Physics*. Ed. by Peter W. Hawkes. Vol. 171. Advances in Imaging and Electron Physics. Elsevier, 2012, pp. 297–356. DOI: https://doi.org/10.1016/B978-0-12-394297-5.00006-4 (cited on pages 44, 47).

[193] David B. Williams and C. Barry Carter. *Transmission Electron Microscopy: A Textbook for Materials Science*. Boston, MA: Springer US, 2009, pp. 3–38. DOI: 10.1007/978-0-387-76501-3 (cited on pages 44–46).

[194] Joseph I. Goldstein, Dale E. Newbury, Joseph R. Michael, Nicholas W. M. Ritchie, John Henry J. Scott, and David C. Joy. *Scanning Electron Microscopy and X-Ray Microanalysis*. New York, NY: Springer New York, 2018. DOI: 10.1007/978-1-4939-6676-9 (cited on pages 45, 46).

[195] Mark Fox. *Optical Properties of Solids*. Oxford University Press, 2001 (cited on pages 47–49).

[196] Zeger Hens and Iwan Moreels. "Light absorption by colloidal semiconductor quantum dots." In: *J. Mater. Chem.* 22 (21 2012), pp. 10406–10415. DOI: 10.1039/C2JM30760J (cited on page 49).

[197] Wei-Yu Wu, J. N. Schulman, T. Y. Hsu, and Uzi Efron. "Effect of size nonuniformity on the absorption spectrum of a semiconductor quantum dot system." In: *Appl. Phys. Lett.* 51.10 (1987), pp. 710–712. DOI: 10.1063/1.98896 (cited on page 50).

[198] *Fluorolog-3® with FluorEssence™Operation Manual*. HORIBA Instruments Incorporated. Edison, USA, 2014 (cited on page 50).

[199] Knut Rurack. "Fluorescence Quantum Yields: Methods of Determination and Standards." In: *Standardization and Quality Assurance in Fluorescence Measurements I: Techniques*. Ed. by Ute Resch-Genger. Berlin, Heidelberg: Springer Berlin Heidelberg, 2008, pp. 101–145. DOI: 10.1007/4243_2008_019 (cited on page 50).

[200] C. A. Parker and W. T. Rees. "Correction of fluorescence spectra and measurement of fluorescence quantum efficiency." In: *Analyst* 85 (1013 1960), pp. 587–600. DOI: 10.1039/AN9608500587 (cited on page 50).

[201] *Quanta-ϕF-3029 Integrating Sphere*. HORIBA Scientific. Operation Manual, 2010 (cited on page 50).

[202] Kengo Suzuki, Atsushi Kobayashi, Shigeo Kaneko, Kazuyuki Takehira, Toshitada Yoshihara, Hitoshi Ishida, Yoshimi Shiina, Shigero Oishi, and Seiji Tobita. "Reevaluation of absolute luminescence quantum yields of standard solutions using a spectrometer with an integrating sphere and a back-thinned CCD detector." In: *Phys. Chem. Chem. Phys.* 11 (42 2009), pp. 9850–9860. DOI: 10.1039/B912178A (cited on page 50).

[203] Christian Würth, Markus Grabolle, Jutta Pauli, Monika Spieles, and Ute Resch-Genger. "Comparison of Methods and Achievable Uncertainties for the Relative and Absolute Measurement of Photoluminescence Quantum Yields." In: *Anal. Chem.* 83.9 (2011), pp. 3431–3439. DOI: 10.1021/ac2000303 (cited on page 51).

[204] Alexander F. Richter. "Charge Carrier Dynamics in Nontoxic Semiconductor Quantum Dots." PhD thesis. Munich: Ludwig-Maximilians-Universität, 2020 (cited on page 52).

[205] *PInano® High Precision & Stability XYZ Piezo Stage*. Physik Instrumente PI GmbH & Co. KG. Edison, USA, 2009 (cited on page 53).

[206] *SuperK SELECT*. NKT Photonics. Birkerod, Denmark, 2019 (cited on page 54).

[207] *SuperK Extend-UV Instruction Manual*. NKT Photonics. Birkerod, Denmark, 2014 (cited on page 54).

[208] Wolfgang Demtröder. "Elektromagnetische Wellen in Materie." In: *Experimentalphysik 2: Elektrizität und Optik*. Berlin, Heidelberg: Springer Berlin Heidelberg, 2013, pp. 219–259. DOI: 10.1007/978-3-642-29944-5_8 (cited on pages 54, 55).

[209] S. Pancharatnam. "Achromatic combinations of birefringent plates." In: *Proc. Indian Acad. Sci. - A* 41.4 (1955), pp. 130–136. DOI: 10.1007/BF03047097 (cited on page 55).

[210] Wolfgang Becker. "Introduction to Multi-dimensional TCSPC." In: *Advanced Time-Correlated Single Photon Counting Applications*. Ed. by Wolfgang Becker. Cham: Springer International Publishing, 2015, pp. 1–63. DOI: 10.1007/978-3-319-14929-5_1 (cited on page 58).

[211] Michael Wahl. *Technical Note: Time-Correlated Single Photon Counting*. PicoQuant GmbH. Berlin, Germany, 2014 (cited on page 58).

[212] Bernhard J. Bohn. "Exciton Dynamics in Lead Halide Perovskite Nanocrystals: Recombination, Dephasing and Diffusion." PhD thesis. Munich: Ludwig-Maximilians-Universität, 2019 (cited on page 59).

[213] Ilka Vinçon, Anja Barfüßer, Jochen Feldmann, and Quinten A. Akkerman. "Quantum Dot Metal Salt Interactions Unraveled by the Sphere of Action Model." In: *J. Am. Chem. Soc.* 145.26 (2023), pp. 14395–14403. DOI: 10.1021/jacs.3c03582 (cited on page 61).

[214] Michael A. Becker, Roman Vaxenburg, Georgian Nedelcu, Peter C. Sercel, Andrew Shabaev, Michael J. Mehl, John G. Michopoulos, Samuel G. Lambrakos, Noam Bernstein, John L. Lyons, Thilo Stöferle, Rainer F. Mahrt, Maksym V. Kovalenko, David J. Norris, Gabriele Rainò, and Alexander L. Efros. "Bright triplet excitons in caesium lead halide perovskites." In: *Nature* 553.7687 (2018), pp. 189–193. DOI: 10.1038/nature25147 (cited on page 63).

[215] Georgian Nedelcu, Loredana Protesescu, Sergii Yakunin, Maryna I. Bodnarchuk, Matthias J. Grotevent, and Maksym V. Kovalenko. "Fast Anion-Exchange in Highly Luminescent Nanocrystals of Cesium Lead Halide Perovskites ($CsPbX_3$, X = Cl, Br, I)." In: *Nano Lett.* 15.8 (2015), pp. 5635–5640. DOI: 10.1021/acs.nanolett.5b02404 (cited on page 66).

[216] Ward van der Stam, Jaco J. Geuchies, Thomas Altantzis, Karel H. W. van den Bos, Johannes D. Meeldijk, Sandra Van Aert, Sara Bals, Daniel Vanmaekelbergh, and Celso de Mello Donega. "Highly Emissive Divalent-Ion-Doped Colloidal CsPb1−xMxBr3 Perovskite Nanocrystals through Cation Exchange." In: *J. Am. Chem. Soc.* 139.11 (2017), pp. 4087–4097. DOI: 10.1021/jacs.6b13079 (cited on page 66).

[217] Hui Cheng, Jing Leng, Fengke Sun, Shengli Zhao, Jianbo Tang, Kaifeng Wu, Jiming Bian, and Shengye Jin. "Dopant-Induced Slow Spin Relaxation in CsPbBr3 Perovskite Nanocrystals." In: *ACS Energy Lett.* 7.12 (2022), pp. 4325–4332. DOI: 10.1021/acsenergylett.2c01901 (cited on page 69).

[218] Aleksander M. Ulatowski, Adam D. Wright, Bernard Wenger, Leonardo R. V. Buizza, Silvia G. Motti, Hannah J. Eggimann, Kimberley J. Savill, Juliane Borchert, Henry J. Snaith, Michael B. Johnston, and Laura M. Herz. "Charge-Carrier Trapping Dynamics in Bismuth-Doped Thin Films of $MAPbBr_3$ Perovskite." In: *J. Phys. Chem. Lett.* 11.9 (2020), pp. 3681–3688. DOI: 10.1021/acs.jpclett.0c01048 (cited on page 69).

[219] Yasuhiro Yamada, Mizuki Hoyano, Ryo Akashi, Kenichi Oto, and Yoshihiko Kanemitsu. "Impact of Chemical Doping on Optical Responses in Bismuth-Doped $CH_3NH_3PbBr_3$ Single Crystals: Carrier Lifetime and Photon Recycling." In: *J. Phys. Chem. Lett.* 8.23 (2017), pp. 5798–5803. DOI: 10.1021/acs.jpclett.7b02508 (cited on page 69).

[220] Rui Meng, Guangbao Wu, Jiyu Zhou, Huiqiong Zhou, Honghua Fang, Maria A. Loi, and Yuan Zhang. "Understanding the Impact of Bismuth Heterovalent Doping on the Structural and Photophysical Properties of $CH_3NH_3PbBr_3$ Halide Perovskite Crystals with Near-IR Photoluminescence." In: *Chem. Eur. J.* 25.21 (2019), pp. 5480–5488. DOI: https://doi.org/10.1002/chem.201805370 (cited on page 69).

[221] Erin Jedlicka, Jian Wang, Joshua Mutch, Young-Kwang Jung, Preston Went, Joseph Mohammed, Mark Ziffer, Rajiv Giridharagopal, Aron Walsh, Jiun-Haw Chu, and David S. Ginger. "Bismuth Doping Alters Structural Phase Transitions in Methylammonium Lead Tribromide Single Crystals." In: *J. Phys. Chem. Lett.* 12.11 (2021), pp. 2749–2755. DOI: 10.1021/acs.jpclett.1c00334 (cited on page 69).

[222] Eric A.J. Reits and Jacques J. Neefjes. "From fixed to FRAP: measuring protein mobility and activity in living cells." In: *Nat. Cell Biol.* 3.6 (2001), E145–E147. DOI: 10.1038/35078615 (cited on page 72).

[223] Tasnim Ahmed, Apurba De, Sumanta Paul, and Anunay Samanta. "Individual Particle-Level Picture of Charge Carrier Recombination in Bi-Doped $CsPbBr_3$ Nanocrystals." In: *J. Phys. Chem. C* 125.3 (2021), pp. 2156–2162. DOI: 10.1021/acs.jpcc.0c10037 (cited on page 75).

[224] Yuanwei Li, Haixin Lin, Wenjie Zhou, Lin Sun, Devleena Samanta, and Chad A. Mirkin. "Corner-, edge-, and facet-controlled growth of nanocrystals." In: *Sci. Adv.* 7.3 (2021), eabf1410. DOI: 10.1126/sciadv.abf1410 (cited on page 78).

[225] Seoin Back, Min Sun Yeom, and Yousung Jung. "Active Sites of Au and Ag Nanoparticle Catalysts for CO_2 Electroreduction to CO." In: *ACS Catal.* 5.9 (2015), pp. 5089–5096. DOI: 10.1021/acscatal.5b00462 (cited on page 78).

[226] Blanka E. Janicek, Joshua G. Hinman, Jordan J. Hinman, Sang hyun Bae, Meng Wu, Jacob Turner, Huei-Huei Chang, Eugene Park, Rachel Lawless, Kenneth S. Suslick, Catherine J. Murphy, and Pinshane Y. Huang. "Quantitative Imaging of Organic Ligand Density on Anisotropic Inorganic Nanocrystals." In: *Nano Lett.* 19.9 (2019), pp. 6308–6314. DOI: 10.1021/acs.nanolett.9b02434 (cited on page 78).

[227] Irving Langmuir. "THE ADSORPTION OF GASES ON PLANE SURFACES OF GLASS, MICA AND PLATINUM." In: *J. Am. Chem. Soc.* 40.9 (1918), pp. 1361–1403. DOI: 10.1021/ja02242a004 (cited on page 79).

[228] Xiaohui Ji, Danis Copenhaver, Christopher Sichmeller, and Xiaogang Peng. "Ligand Bonding and Dynamics on Colloidal Nanocrystals at Room Temperature: The Case of Alkylamines on CdSe Nanocrystals." In: *J. Am. Chem. Soc.* 130.17 (2008), pp. 5726–5735. DOI: 10.1021/ja710909f (cited on page 79).

[229] Iwan Moreels, Jose C. Martins, and Zeger Hens. "Ligand Adsorption/Desorption on Sterically Stabilized InP Colloidal Nanocrystals: Observation and Thermodynamic Analysis." In: *ChemPhysChem* 7.5 (2006), pp. 1028–1031. DOI: https://doi.org/10.1002/cphc.200500659 (cited on pages 79, 80).

[230] C. Bullen and P. Mulvaney. "The Effects of Chemisorption on the Luminescence of CdSe Quantum Dots." In: *Langmuir* 22.7 (2006), pp. 3007–3013. DOI: 10.1021/la051898e (cited on pages 79, 80).

[231] Helmut HAUSER, Michael C. PHILLIPS, Barry A. LEVINE, and Robert J. P. WILLIAMS. "Ion-Binding to Phospholipids." In: *Eur. J. Biochem.* 58.1 (1975), pp. 133–144. DOI: https://doi.org/10.1111/j.1432-1033.1975.tb02357.x (cited on page 80).

[232] H. Le Chatelier. "Sur Un Énoncé Général des Lois des Équilibres Chimiques." In: *C. R. Acad. Sci. Paris ou CRAS* 99 (1884), pp. 786–789 (cited on page 81).

[233] Feng Li, Chun Ma, Hong Wang, Weijin Hu, Weili Yu, Arif D. Sheikh, and Tom Wu. "Ambipolar solution-processed hybrid perovskite phototransistors." In: *Nat. Commun.* 6.1 (2015), p. 8238. DOI: 10.1038/ncomms9238 (cited on page 82).

[234] Jizhong Song, Leimeng Xu, Jianhai Li, Jie Xue, Yuhui Dong, Xiaoming Li, and Haibo Zeng. "Monolayer and Few-Layer All-Inorganic Perovskites as a New Family of Two-Dimensional Semiconductors for Printable Optoelectronic Devices." In: *Adv. Mater.* 28.24 (2016), pp. 4861–4869. DOI: https://doi.org/10.1002/adma.201600225 (cited on page 82).

[235] Somnath Das, Apurba De, and Anunay Samanta. "Ambient Condition Mg^{2+} Doping Producing Highly Luminescent Green- and Violet-Emitting Perovskite Nanocrystals with Reduced Toxicity and Enhanced Stability." In: *J. Phys. Chem. Lett.* 11.3 (2020), pp. 1178–1188. DOI: 10.1021/acs.jpclett.9b03831 (cited on page 82).

[236] Zi-Jun Yong, Shao-Qiang Guo, Ju-Ping Ma, Jun-Ying Zhang, Zhi-Yong Li, Ya-Meng Chen, Bin-Bin Zhang, Yang Zhou, Jie Shu, Jia-Li Gu, Li-Rong Zheng, Osman M. Bakr, and Hong-Tao Sun. "Doping-Enhanced Short-Range Order of Perovskite Nanocrystals for Near-Unity Violet Luminescence Quantum Yield." In: *J. Am. Chem. Soc.* 140.31 (2018), pp. 9942–9951. DOI: 10.1021/jacs.8b04763 (cited on page 82).

[237] Ju-Ping Ma, Jia-Kai Chen, Jun Yin, Bin-Bin Zhang, Qing Zhao, Yoshihiro Kuroiwa, Chikako Moriyoshi, Lili Hu, Osman M. Bakr, Omar F. Mohammed, and Hong-Tao Sun. "Doping Induces Structural Phase Transitions in All-Inorganic Lead Halide Perovskite Nanocrystals." In: *ACS Mater. Lett.* 2.4 (2020), pp. 367–375. DOI: 10.1021/acsmaterialslett.0c00059 (cited on page 82).

[238] Arthur Shapiro, Markus W. Heindl, Faris Horani, Meir-Haim Dahan, Jiang Tang, Yaron Amouyal, and Efrat Lifshitz. "Significance of Ni Doping in $CsPbX_3$ Nanocrystals via Postsynthesis Cation–Anion Coexchange." In: *J. Phys. Chem. C* 123.40 (2019), pp. 24979–24987. DOI: 10.1021/acs.jpcc.9b08317 (cited on page 82).

[239] He Huang, Maryna I. Bodnarchuk, Stephen V. Kershaw, Maksym V. Kovalenko, and Andrey L. Rogach. "Lead Halide Perovskite Nanocrystals in the Research Spotlight: Stability and Defect Tolerance." In: *ACS Energy Lett.* 2.9 (2017), pp. 2071–2083. DOI: 10.1021/acsenergylett.7b00547 (cited on page 86).

[240] Yu Tong, Eva Bladt, Meltem F. Aygüler, Aurora Manzi, Karolina Z. Milowska, Verena A. Hintermayr, Pablo Docampo, Sara Bals, Alexander S. Urban, Lakshminarayana Polavarapu, and Jochen Feldmann. "Highly Luminescent Cesium Lead Halide Perovskite Nanocrystals with Tunable Composition and Thickness by Ultrasonication." In: *Angew. Chem. Int. Ed.* 55.44 (2016), pp. 13887–13892. DOI: https://doi.org/10.1002/anie.201605909 (cited on page 86).

[241] Junsheng Chen, Karel Žídek, Pavel Chábera, Dongzhou Liu, Pengfei Cheng, Lauri Nuuttila, Mohammed J. Al-Marri, Heli Lehtivuori, Maria E. Messing, Keli Han, Kaibo Zheng, and Tõnu Pullerits. "Size- and Wavelength-Dependent Two-Photon Absorption Cross-Section of $CsPbBr_3$ Perovskite Quantum Dots." In: *J. Phys. Chem. Lett.* 8.10 (2017), pp. 2316–2321. DOI: 10.1021/acs.jpclett.7b00613 (cited on page 86).

[242] Saman Jahani and Zubin Jacob. "All-dielectric metamaterials." In: *Nat. Nanotechnol.* 11.1 (2016), pp. 23–36. DOI: 10.1038/nnano.2015.304 (cited on page 86).

[243] Bianca M. I. van der Zande, Laurent Pagès, Rifat A. M. Hikmet, and Alfons van Blaaderen. "Optical Properties of Aligned Rod-Shaped Gold Particles Dispersed in Poly(vinyl alcohol) Films." In: *J. Phys. Chem. B* 103.28 (1999), pp. 5761–5767. DOI: 10.1021/jp9847383 (cited on page 91).

[244] "A Potpourri of Particles." In: *Absorption and Scattering of Light by Small Particles*. John Wiley & Sons, Ltd, 1998. Chap. 8, pp. 181–223. DOI: https://doi.org/10.1002/9783527618156.ch8 (cited on page 91).

[245] Otto L. Muskens, Guillaume Bachelier, Natalia Del Fatti, Fabrice Vallée, Arnaud Brioude, Xuchuan Jiang, and Marie-Paule Pileni. "Quantitative Absorption Spectroscopy of a Single Gold Nanorod." In: *J. Phys. Chem. C* 112.24 (2008), pp. 8917–8921. DOI: 10.1021/jp8012865 (cited on pages 91, 101).

[246] Inki Kim, Jaehyuck Jang, Gyeongtae Kim, Jihae Lee, Trevon Badloe, Jungho Mun, and Junsuk Rho. "Pixelated bifunctional metasurface-driven dynamic vectorial holographic color prints for photonic security platform." In: *Nat. Commun.* 12.1 (2021), p. 3614. DOI: 10.1038/s41467-021-23814-5 (cited on page 92).

[247] Yu Tong, En-Ping Yao, Aurora Manzi, Eva Bladt, Kun Wang, Markus Döblinger, Sara Bals, Peter Müller-Buschbaum, Alexander S. Urban, Lakshminarayana Polavarapu, and Jochen Feldmann. "Spontaneous Self-Assembly of Perovskite Nanocrystals into Electronically Coupled Supercrystals: Toward Filling the Green Gap." In: *Adv. Mater.* 30.29 (2018), p. 1801117. DOI: https://doi.org/10.1002/adma.201801117 (cited on page 93).

[248] Zhuang Liu, Xian Qin, Qihao Chen, Tianci Jiang, Qiushui Chen, and Xiaogang Liu. "Metal–Halide Perovskite Nanocrystal Superlattice: Self-Assembly and Optical Fingerprints." In: *Adv. Mater.* 35.16 (2023), p. 2209279. DOI: https://doi.org/10.1002/adma.202209279 (cited on page 93).

[249] David Grosso, Cédric Boissière, and Marco Faustini. "Thin Film Deposition Techniques." In: *The Sol-Gel Handbook*. John Wiley & Sons, Ltd, 2015. Chap. 9, pp. 277–316. DOI: https://doi.org/10.1002/9783527670819.ch09 (cited on page 94).

[250] Frederik C. Krebs. "Fabrication and processing of polymer solar cells: A review of printing and coating techniques." In: *Sol. Energy Mater. Sol. Cells* 93.4 (2009). Processing and Preparation of Polymer and Organic Solar Cells, pp. 394–412. DOI: https://doi.org/10.1016/j.solmat.2008.10.004 (cited on page 94).

[251] Biplab K. Patra, Harshal Agrawal, Jian-Yao Zheng, Xun Zha, Alex Travesset, and Erik C. Garnett. "Close-Packed Ultrasmooth Self-assembled Monolayer of $CsPbBr_3$ Perovskite Nanocubes." In: *ACS Appl. Mater. Interfaces* 12.28 (2020), pp. 31764–31769. DOI: 10.1021/acsami.0c05945 (cited on page 94).

[252] Erika Penzo, Anna Loiudice, Edward S. Barnard, Nicholas J. Borys, Matthew J. Jurow, Monica Lorenzon, Igor Rajzbaum, Edward K. Wong, Yi Liu, Adam M. Schwartzberg, Stefano Cabrini, Stephen Whitelam, Raffaella Buonsanti, and Alexander Weber-Bargioni. "Long-Range Exciton Diffusion in Two-Dimensional Assemblies of Cesium Lead Bromide Perovskite Nanocrystals." In: *ACS Nano* 14.6 (2020), pp. 6999–7007. DOI: 10.1021/acsnano.0c01536 (cited on page 94).

[253] Horst Kuchling. *Taschenbuch der Physik*. 19., aktualisierte Auflage. München; Wien: Hanser Fachbuchverlag, 2007, p. 623 (cited on page 95).

[254] Zhongpeng Zhu, Ye Tian, Yupeng Chen, Zhen Gu, Shutao Wang, and Lei Jiang. "Superamphiphilic Silicon Wafer Surfaces and Applications for Uniform Polymer Film Fabrication." In: *Angew. Chem. Int. Ed.* 56.21 (2017), pp. 5720–5724. DOI: https://doi.org/10.1002/anie.201700039 (cited on page 95).

[255] Georgy Ermolaev, Anatoly P. Pushkarev, Alexey Zhizhchenko, Aleksandr A. Kuchmizhak, Ivan Iorsh, Ivan Kruglov, Arslan Mazitov, Arthur Ishteev, Kamilla Konstantinova, Danila Saranin, Aleksandr Slavich, Dusan Stosic, Elena S. Zhukova, Gleb Tselikov, Aldo Di Carlo, Aleksey Arsenin, Kostya S. Novoselov, Sergey V. Makarov, and Valentyn S. Volkov. "Giant and Tunable Excitonic Optical Anisotropy in Single-Crystal Halide Perovskites." In: *Nano Lett.* 23.7 (2023), pp. 2570–2577. DOI: 10.1021/acs.nanolett.2c04792 (cited on page 102).

[256] Nazifa Tabassum, Zheni N. Georgieva, Gouranga H. Debnath, and David H. Waldeck. "Size-dependent chiro-optical properties of $CsPbBr_3$ nanoparticles." In: *Nanoscale* 15 (5 2023), pp. 2143–2151. DOI: 10.1039/D2NR06751J (cited on page 102).

[257] Nadesh Fiuza-Maneiro, Kun Sun, Iago López-Fernández, Sergio Gómez-Graña, Peter Müller-Buschbaum, and Lakshminarayana Polavarapu. "Ligand Chemistry of Inorganic Lead Halide Perovskite Nanocrystals." In: *ACS Energy Lett.* 8.2 (2023), pp. 1152–1191. DOI: 10.1021/acsenergylett.2c02363 (cited on page 102).

[258] Quinten A. Akkerman, Laura Martínez-Sarti, Luca Goldoni, Muhammad Imran, Dmitry Baranov, Henk J. Bolink, Francisco Palazon, and Liberato Manna. "Molecular Iodine for a General Synthesis of Binary and Ternary Inorganic and Hybrid Organic–Inorganic Iodide Nanocrystals." In: *Chem. Mater.* 30.19 (2018), pp. 6915–6921. DOI: 10.1021/acs.chemmater.8b03295 (cited on page XIX).

[259] Edward D. Palik. *Handbook of Optical Constants of Solids*. Burlington: Academic Press, 1997. DOI: https://doi.org/10.1016/B978-012544415-6.50143-6 (cited on page XX).

[260] Robert J. Moerland and Jacob P. Hoogenboom. "Subnanometer-accuracy optical distance ruler based on fluorescence quenching by transparent conductors." In: *Optica* 3.2 (2016), pp. 112–117. DOI: 10.1364/OPTICA.3.000112 (cited on page XX).

Appendix

Chemicals

All chemicals were used as received unless otherwise stated. The following chemicals were purchased from Sigma Aldrich: bismuth tribromide ($BiBr_3$, >98%), cesium carbonate (Cs_2CO_3, 99.995%), indium bromide (InBr3, 99%, dried for 3h at vacuum before usage), lead bromide ($PbBr_2$, 99.999%), magnesium bromide ($MgBr_2$, 98%), nickel bromide ($NiBr_2$, 98%), zinc bromide ($ZnBr_2$, anhydrous), acetone (for HPLC, >99.8%), chromium etchant (standard), didodecyldimethylammoniumbromid (DDAB, 98%), diisooctylphosphinic acid (DOPA, technical grade, 90%), ethanol (for HPLC, >99.8%), hexane (Reagent Plus, > 99%), 1-octadecene (ODE, technical grade, 90%), n-octane (98%), oleic acid (OA, >99%, for spheroidal QDs), 2-propanol (IPA, ACS reagent, >99.8%), toluene (ACS reagent, >99.8%), and tricoctylphosphine oxide (TOPO, 99%). Oleic acid (OA, technical grade, 90%, decassed 1h, 120℃, vacuum) and oleylamine (OAm, 80–90%, decassed 1h, 120℃, vacuum) for the synthesis of cubic quantum dots were purchased from Alfa Aesar and Acos, respectively. Lecithin (from soy beans, 97%) was obtained from Carl Roth. For the e-beam lithography, the following chemicals were used: 495 PMMA A4/950 PMMA A4 (from Kayaku), E-Spacer 300Z (from Showa Denko Europe GmbH), Microposit Remover 1165 (from Dupont), Methylisobutylketone (from Technic), glass substrates with a 18 nm indium tin oxide (ITO) layer (from Nanoscribe), and anhydrous acetone (from VWR).

Synthesis of $CsPbBr_3$ QDs

For cubic $CsPbBr_3$ QD, a 65 mM $PbBr_2$ monomer was prepared from 367 mg (1 mmol) $PbBr_2$, 2.5 mL OAm, and 0.25 mL OA in 12.5 mL ODE heated to 100 °C for 1 h for complete dissolution. A 70 mM Cs-oleate was obtained by mixing 400 mg (1.2 mmol) Cs_2CO_3, 1.75 mL OA and 15 mL ODE at 150 °C. A minor oxidation evident by the slight brownish discoloration is accepted as a side effect. The $PbBr_2$ monomer was placed on a hot plate set to 200 °C. Thus, its heating mode was maintained during the subsequent injection of 2.5 mL Cs-oleate upon vigorous stirring, once the temperature reached 170 °C (for approx. 8 nm $CsPbBr_3$ QDs). After 30 s the reaction was quenched with an icebath, followed by 10 min centrifugation at 17 200 g. The supernatant was discarded and remains of ODE, which as a long-chain solvent has an affinity to plastic, were removed by carefully rinsing the centrifugation tube walls with hexane[258] prior to dispersing the finished product in 0.5 mL toluene. An additional centrifugation step at 4300 g for 3 min has been applied to remove large clusters.

For spheroidal $CsPbBr_3$ QDs, a 40 mM $PbBr_2$ monomer was prepared from 1 mmol $PbBr_2$, 5 mmol TOPO and 5 mL octane heated to 120 °C until dissolving $PbBr_2$ and subsequent dilution with 20 mL hexane prior to filtration with a syringe filter (PVDF, 0.45 µm, Carl Roth). 100 mg Cs_2CO_3 were dissolved in 2 mL octane and 1 mL DOPA at 120 °C before adding 27 mL hexane to yield the 20 mM Cs-DOPA monomer. 250 µL of Cs-DOPA was quickly injected in the reaction solution composed of 10 mL hexane with 500 µL $PbBr_2$-monomer and 0-1000 µL of a TOPO

solution (200 mM in hexane). Typical additional TOPO amounts to yield different particle sizes are shown in Table A.1. After 4 min, 500 µL of lecithin solution (50 mg/L in hexane) were added followed by a threefold excess of acetone 1 min later. The precipitate was collected by centrifugation (17 200 g for 4 min) and washed with a 1:1 mixture of toluene:ethanol and centrifugation at 4300 g for 3 min. Finally, the QDs were dispersed in 500 µL of hexane.

Table A.1: Synthetic Parameters for $CsPbBr_3$ Quantum Dots of variable Size.

QD diameter (nm)	4.4	4.9	6.2	6.6	7.7	8.8	11.8
TOPO (μL)	0	50	250	300	500	650	875

Post-Synthetic Modification of Spheroidal $CsPbBr_3$ QDs

Briefly, 40 mM monomer solutions of metal salts MBr_2/MBr_3 with M=Bi, Au, Ni, In, Mg, Zn have been prepared analogously to the $PbBr_2$ monomer. These stock solutions were either directly used, or further diluted 1:100 with hexane. Studies with different metal salts were conducted by adding 30 µL of the respective stock solution to 4 mL of a QD solution of volumetric fraction $4 \cdot 10^{-6}$. For detailed spectroscopic studies, 40 µL concentrated QD solution (volume fraction of $6 \cdot 10^{-4}$) and 10-200 µL diluted $BiBr_3$-solution were mixed by shaking and reacted for 5 min. These samples were subsequently washed with a threefold excess of acetone followed by centrifugation (4300 g). The precipitate was dissolved in 500 µL hexane for subsequent optical analysis. For the *in-situ* measurements of the adsorption kinetics (see Subsection 3.4.1), aliquots of diluted $BiBr_3$ monomer were added to a QD solution of $7.25 \cdot 10^{-6}$ volumetric fraction in hexane, providing up to 100 $BiBr_3$ per QD.

Electromagnetic Simulations

Based on finite-difference time-domain (FDTD) simulations with the commercially available software from Lumerical Inc, the z-metasurface light-matter interactions have been simulated. The simulation has been performed for one unit cell of the z-metasurface lattice as sketched below. Lattice interactions have been taken into account by applying periodic boundary conditions in the x-y-plane. In z-direction, a total slab of 2 µm, both above and below the z-metasurface, has been taken into account using perfectly matched layers. The materials' optical properties have been modeled using dielectric constants obtained from the Lumerical materials library[259] (for silicon and SiO_2) or data from Moerland and Hoogenbooms[260] (for ITO).

A perpendicular illumination with a circularly polarized plane wave propagating in z-direction has been realized with the help of two linearly polarized plane waves sources located 2 µm above the substrate. This is well outside the near-field regime. The plane wave's electric field vector have been oriented at 90° towards each other with a relative phase shift of 90° (−90°) to yield right (left) CP light. The simulated reflection response of the z-metasurface has been determined at a 2D power monitor which has been located at a distance of 3 µm above the substrate.

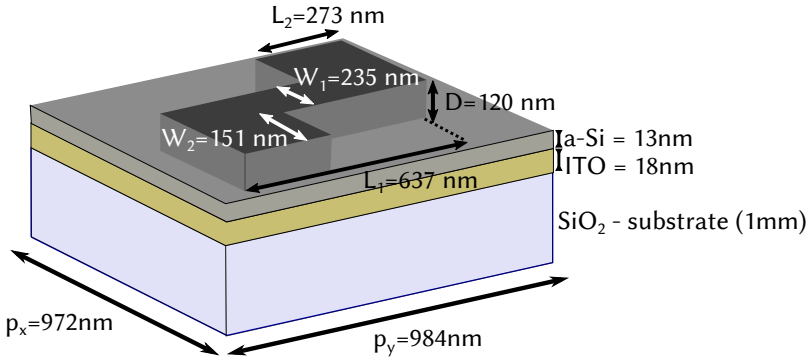

Sketch of the unit cell applied in electromagnetic simulations.

Fermi's Golden Rule: The Dipole Approximation for Excitons

The transition to an exciton state $|X_\mathrm{i}\rangle$ from a ground state $|0\rangle$, neglecting confinement for a moment, can be described in terms of a matrix element:[90]

$$\langle X_\mathrm{i}|H'|0\rangle = N|\phi_\mathrm{nlm}(0)|^2|\langle\psi_\mathrm{c}|H_\mathrm{eR}|\psi_\mathrm{v}\rangle|^2. \tag{A.1}$$

N is the number of primitive unit cells within the system, while $\phi_\mathrm{nlm}(0)$ is the wavefunction of the exciton's relative motion. As such, a transition and thus exciton creation only occurs if there is a non-zero probability for electron and hole to be present within the same unit cell. The last term, $\langle\psi_\mathrm{c}|H_\mathrm{eR}|\psi_\mathrm{v}\rangle$, denotes the matrix element for the Bloch electron involved in the transition, with its respective wavefunction in conduction (ψ_c) and valence band (ψ_v).[90] In a semi-classical approach, the light is described classically as an electromagnetic wave by its vector potential $\boldsymbol{A}$, which interacts with the electron defined in a quantum mechanical frame by its momentum operator $\boldsymbol{p}$. In the simplest case, in the limit of the electric dipole approximation, the Hamiltonian reduces to:

$$H_\mathrm{eR} = \frac{e}{m^*}\boldsymbol{A}\boldsymbol{p} = -e|\boldsymbol{E}|\hat{\boldsymbol{e}}\boldsymbol{r}. \tag{A.2}$$

It depends on the amplitude of the light's electric field vector $\boldsymbol{E}$ and the orientation of its unit vector $\hat{\boldsymbol{e}}$ towards the electron's position operator $\boldsymbol{r}$.[90] Together, charge and position form an operator for the electric dipole moment $\boldsymbol{\mu} = e\boldsymbol{r}$, lending the approximation its name. With Equation A.1 and Equation A.2 in Equation 2.23, the transition probability to an excitonic state $|X_\mathrm{i}\rangle$ as stated in Equation 2.24 is obtained.

List of Figures

List of Tables

List of Abbreviations

a-Si amorphous silicon
APD avalanche photodiode
CCD charge coupled device
CVD chemical vapor deposition
CP circularly polarized
DDQ distant dependent quenching
DM dichroic mirror
DOPA diisooctylphosphonic acid
F fluorophore
FWHM full width at half maximum
HI hot-injection
IRF instrumental response function
LCG ligand controlled growth
LED light emitting diode
LHP lead halide perovskite
LP long pass
NC nanocrystal
OA oleic acid
OAm oleyl amine
ODE octadecene
PL photoluminescence
PLE photoluminescence excitation
PLQY photoluminescence quantum yield
Q quencher
QD quantum dot
SEM scanning electron microscope
SE secondary electron
SP short pass
TAS transient absorption spectroscopy
TCSPC time correlated single photon counting
TEM transmission electron microscope
TOPO trioctylphosphineoxide

Acknowledgments

This is the end of a long journey – needless to say, it would have never been possible without support from everyone who shared this path with me and whom I want to thank at this point.

I am very grateful to Prof. Dr. Jochen Feldmann – you gave me this opportunity to switch gears and step into physics, believing that I am capable of doing this. From the beginning, I had the chance to take responsibilities and learn to step up to it. Thank you for showing me the beauty of fundamental clear explanations, how to not get lost in details and being efficient in pushing scientific questions.

Many thanks to my collaborators from the Chair of Hybrid Nanosystems – Daniele de Gregorio, Fedja Wendisch, Leonardo de S. Menezes and Haoran Ren and Prof. Stefan Maier. Together you introduced me to the world of metasurfaces and provided the foundation for my first project. Especially the long and fruitful discussions with you, Fedja and Leo, allowed to have a system that worked in the end.

I want to thank Quinten Akkerman for coming up with a beautiful project when I most needed it. Thank you Quinten, for providing a bridge to my chemistry background, for sharing all your knowledge on quantum dots and their synthesis and above all, to make me remember that I still like chemistry.

A warm thanks to Alexander Richter and Stefanie Pritzl, Anja Barfüßer, Philipp Bootz, and Jinhua Zhang – sharing an office with you was great! Thank you Alex for guiding me in the laser labs in my first year and answering all questions on time-resolved spectroscopy. I was very lucky to have you, Steffi and Anja – apologies for the countless times I distracted you from your own work to listen to and discuss my ideas and problems.

I am also very thankful to accompany you, Jakob Riedel, among other students during your master thesis. I learned a lot through and from you.

Thanks a lot to Gerlinde Adam – you have been a tremendous help around the office, always grounding me with your calmness and friendliness. Thank you also Stefan Niedermaier and Talee Barghouti, only due to you lab work was made possible in such a smooth way.

Thanks to all my current and former colleagues at the chair for equipping me with all the memorable stories that I can take away, not only about work. A special thanks to Anja Barfüßer, Quinten Akkerman, Mariam Kurashvili, Dominik Kammerer, Philipp Bootz, Fedja Wendisch, Stefanie Pritzl, Andreas Aigner, Alexander Richter, Matthias Kestler and Julian Mann for helping proofread this thesis.

I especially want to thank my friends and my family, for all the support not only during my PhD, but also along the way that got me up to this point. From the bottom of my heart I last but not least want to thank you, Leon. Whenever I was stuck and disappointed, you managed to cheer me up – thank you for always believing in me!